Radiation effects and damage formation in semiconductors due to high-energy ion irradiation

DISSERTATION

zur Erlangung des akademischen Grades
doctor rerum naturalium (Dr. rer. nat.)

vorgelegt dem Rat der Physikalisch-Astronomischen Fakultät
der Friedrich-Schiller-Universität Jena

von Diplom-Physiker Andrey Kamarou
geboren am 01.03.1975 in Minsk, Belarus

Gutachter:

1. Prof. Dr. Werner Wesch
   Institut für Festkörperphysik
   Friedrich-Schiller-Universität Jena

2. Prof. Dr. Wolfgang Bolse
   Institut für Strahlenphysik
   Universität Stuttgart

3. Prof. Dr. Hans Hofsäss
   Zweites Physikalisches Institut
   Universität Göttingen

Tag der letzten Rigorosumsprüfung: 29. September 2006
Tag der öffentlichen Verteidigung: 7. November 2006

scipta manent

Zusamenfassung

Gegenstand dieser Arbeit war die Untersuchung ionenstrahlinduzierter Schädenbildung und -ausheilung in kristallinem und konventionell vorgeschädigtem Ge, GaAs und InP. Der zentrale Punkt der Untersuchung bestand in der Aufklärung des Einflusses verschiedener experimenteller Bedingungen auf die oben genannten Effekte.

Die kristallinen und vorgeschädigten Proben wurden entweder bei Flüssigstickstoff-Temperatur (LNT, ≈ 80 K) oder bei Raumtemperatur (RT) mit Kr, Xe oder Au Ionen mit spezifischer Energie von etwa 0.3 MeV/u bis 3 MeV/u bestrahlt. Wesentlich dabei ist die Tatsache, dass in allen diesen Fällen der elektronische Energieverlust pro Ionenweglänge, ε_e, viel größer ist als der nuklerare Energieverlust ε_n. Anschließend wurden die Proben mittels Rutherford Rückstreuspektrometrie (RBS) und/oder Transmissionselektronenmikroskopie (TEM) untersucht.

Die Bestrahlung von einkristallinem Ge und GaAs mit 140 MeV Kr, 390 MeV Xe, und 593 MeV Au Ionen bei RT führt zur schwachen Schädenbildung in den Proben. Die relative Konzentration von Defekten, n_{da}, steigt sehr langsam mit der Ionenfluenz N_I an, wobei der maximale Wert von n_{da} bei der maximal erreichten Fluenz etwa 3% beträgt. Die Hochenergie-Ionenbestrahlung von vorgeschädigten Ge und GaAs Proben bei RT hat eine effektive (bis zu 90%) Ausheilung von vorhandenen Defekten zur Folge, es sei denn, dass die Vorschädigung selbst eine dicke amorphe Schicht erzeugt.

Oberhalb eines *Schwellwertes*, ε_e^{thr}, von etwa 13 keV/nm bei RT, wird eine deutlich stärkere Schädenbildung in InP durch den hohen elektronischen Energieverlust hervorgerufen. Schon relativ kleine Fluenzen der 593 MeV Au oder 390 MeV Xe Bestrahlung führen zu einer Amorphisierung des Materials. Im Gegensatz zu (*überschwelligen*) Bestrahlungen von InP mit 593 MeV Au oder 390 MeV Xe Ionen hat die Bestrahlung von InP mit (*unterschwelligem*) 140 MeV Kr Ionen bei RT keine Amorphisierung zur Folge, und für die maximal erreichte Fluenz beträgt $n_{da} \approx 5\%$. Außerdem führt die Bestrahlung von konventionell vorgeschädigtem InP bei RT zu einer sehr effektiven Ausheilung der vorhandenen Defekte, welche jener von vorgeschädigten Ge und GaAs sehr ähnelt. Im Gegensatz zur 140 MeV Kr Bestrahlung heilen die Schäden in vorgeschädigtem InP weder unter Xe- noch unter Au-Bestrahlung kaum aus.

Die Fluenzabhängigkeit der relativen Defektkonzentration, $n_{da}(N_I)$, wurde in InP im Rahmen des Überlappungs-Modells von Gibbons für verschiedene Ionensorten analysiert. Mit Ausnahme der 140 MeV Kr Bestrahlung, lassen sich die experimentellen Daten für RT- und LNT-Bestrahlungen gut beschreiben, wenn angenommen wird, dass entweder die nullte- oder die erste Ordnung von Überlappungen für eine lokale Amorphisierung notwendig ist.

Untersuchungen mittels Transmissionselektronenmikroskopie (TEM) zeigen, dass die Anzahl der Ionenspuren in InP unter Bestrahlung bei RT mit oberschwelligen Xe- oder Au-Projektilen der Ionenfluenz entspricht. Mit steigender Ionenfluenz fangen die Ionenspuren an sich zu überlappen und werden auf diese Weise breiter. Die Bestrahlung von InP mit 390 MeV Xe Ionen bei LNT erzeugt stark diskontinuierliche Spuren, was die Feststellung erklärt, dass bei LNT einkristallines InP viel strahlungsresistenter ist als bei RT.

Die experimentellen Ergebnisse wurden im Rahmen eines erweiterten Thermal-Spike-Modells (TS) beschrieben. Das Modell schlägt vor, dass die Ionenenergie durch *Elektronen-Phononen-Kopplung* ins Gitter übertragen wird, wobei die Gittertemperatur ansteigt. Wenn die resultierende Gittertemperatur den Schmelzpunkt überschreitet, dann kann das Material lokal geschmolzen werden. Auf diese Weise kann die anschließende Abkühlung und Erstarrung der geschmolzenen Zone die bestehende (partielle) Unordnung einfrieren und so eine Ionenspur hinterlassen.

Die theoretischen Ergebnisse dieser Arbeit ermöglichen es, den Einfluss verschiedener Bestrahlungbedingungen (Ionenmasse und -energie, Bestrahlungstemperatur, usw.) auf die Spurbildung in InP zu erklären und quantitativ zu beschreiben. Weiterhin stehen die Ergebnisse der Rechnungen im Widerspruch zu der in der Literatur weitverbreiteten Verwendung *eines einzelnen Schwellwertes der Spurbildung*, ε_e^{thr}, für *verschiedene Ionensorten*. Die Rechnungen zeigen, dass es keinen allgemeinen Schwellwert ε_e^{thr} in InP gibt, sondern dass dieser für leichtere Ionen größer ist (12.0 keV/nm bzw. 14.8 keV/nm für Au bzw. Xe).

Im Gegensatz zu InP, kann der Schwellwert für die Spurbildung in Ge und in GaAs mit einzelnen Ionen wahrscheinlich noch nicht erreicht werden, selbst nicht unter 593 MeV Au Bestrahlung. Dies ist in Übereinstimmung mit den Ergebnissen, die von anderen Arbeitsgruppen veröffentlicht wurden.

Contents

List of figures

List of tables

List of abbreviations

ASL	Amorphous surface layer
BSU	Belarusian State University, Minsk, Belarus
CSL	Crystalline surface layer
FSU	Friedrich-Schiller-Universität (Friedrich-Schiller-University, Jena, Germany)
HMI	Hahn-Meitner-Institut (Hahn-Meitner Institute, Berlin, Germany)
IFK	Institut für Festkörperphysik (Institute of Solid State Physics, Jena, Germany)
ISL	Ionenstrahllabor (Ion Beam Laboratory, see “HMI”)
LET	Linear energy transfer
LNT	Liquid nitrogen temperature (≈ 77-80 K)
RBS	Rutherford backscattering spectrometry
RT	Room temperature (≈ 300 K)
SHI	Swift heavy ion
SIMS	Secondary ion mass spectrometry
TEM	Transmission electron microscopy
TS	Thermal spike
XRD	X-ray diffraction

List of frequently used symbols

A_I	Damage cross-section (within Gibbons model)
$\Delta\chi_{min}$	Difference in minimum yield (from RBS)
ε_e	Electronic energy loss per ion and unit path length
ε_n	Nuclear energy loss per ion and unit path length
ε_e^{thr}	Threshold (necessary minimum) value of ε_e for track formation
E	Projectile energy
E_d	Displacement energy
E_g	Energy gap
g	Electron-phonon coupling efficiency
m	Number of overlaps (within Gibbons model)
m_e	Electron mass
M_1	Projectile mass
N_a	Target atomic density
N_I	Ion fluence
n_{da}	Measured relative concentration of displaced lattice atoms (from RBS)
n_{dpa}	Calculated relative number of displacements (from the SRIM-2003 code)
T_I	Irradiation temperature
T_m	Melting point
q	Ion charge (ionisation degree)
q_{init}	Initial ion charge
q_{mean}	Mean ion charge
z	Variable of depth
Z_1	Projectile atomic number (nuclear charge)

Chapter 1

Introduction

Germanium (Ge), gallium arsenide (GaAs) and indium phosphide (InP) are well-known semiconductor materials used for various electronic applications. Very often particular important properties of the materials mentioned above (e.g., carrier mobility, break-down voltage, resistance to oxidation, etc.) remarkably surpass the corresponding ones for silicon (Si) which strongly dominates the industry. In this way these alternative materials are far better suited to many future demands. However, their broader application is restricted due to various reasons. First, unlike Si, their constituents are very rare elements in the earth's crust; therefore, a production of the compound materials is inevitably connected with higher costs. Second, there are difficulties connected with fabrication of large high-quality wafers (compare maximum diameters of wafers used in the industry: 6 inches for GaAs and 12 inches for Si). And, last but not least, it is due to a more complex technology necessary to produce single microelectronic elements or chips.

Especially indium phosphide rates a special mention as a very promising material suitable for various electronic and optoelectronic applications [1]. It is considered to be the fourth-wave in semiconductor materials [1], after germanium, silicon and gallium arsenide, due to its outstanding physical properties as, for example, the *highest peak velocity of both electrons and holes* among all known semiconductors; high thermal conductivity and electric field breakdown; tens of percent lower turn-on voltage for different devices if compared to that of competing GaAs and SiGe; low power consumption per transistor, and so on. Its successful applications cover the InP-based high electron mobility transistors which are known to be the fastest among all the transistors (their reported cut-off and maximum oscillation frequencies are about 400 and 600 GHz, respectively); high-efficient and high-speed quantum well lasers, photodetectors and other active and passive optical elements of photonic integrated circuits (amplifiers, switches, (de)multiplexers, couplers and splitters), which are able to work at 1.3 and 1.55 μm light wavelength, and which can be fabricated on a *single chip*; InP-based solar cells for satellite applications on relatively cheap silicon substrates, which have reached the efficiency of 19% and proved to be highly radiation-resistant in real space tests. Also ternary and quaternary alloys (e.g. InGaAs and InGaAsP) can be epitaxially grown lattice-matched on GaAs or InP substrates. By changing the composition of the quaternary alloys, the bandgap wavelength can be tuned anywhere between 0.92 μm and 1.65 μm and, hence, such material can be used for production of both active (absorption or gain) and passive (transparent) electronic elements working in the telecommunication window of 1.25-1.65 μm.

However, InP is a much less investigated material than, for example, GaAs whose commercially viable technology emerged already in the late 1980s. Like GaAs, InP has no native oxide; it means that one has to introduce either additional defects or impurities to create both device/device and active-layer/substrate isolation. Because of the low thermal stability of InP the most prominent way to dope or electrically isolate the material in vertically limited layers or to modify quantum well layers is the ion implantation with MeV ion beams (protons, helium, oxygen, arsenic, etc.).

One cannot help mentioning the recent demands in the modern electronics, as to increase the working frequency of the basic elements, to lower the power consumption and heat dissipation, and to produce more compact chips. Obviously, this leads to a necessity to use deeper layers (probably, combined with 3D integration) and, therefore, one has to apply faster ion beams (tens of MeV and more) in order to modify materials to larger depths. Furthermore, MeV ion beams are known to produce much less surface damage than the conventional keV ions. Thus, MeV ion irradiation can be performed virtually at each temporal stage of the whole technological process (e.g., to form buried isolating and gettering layers, or for a final tuning of the working parameters of completed devices).

During the last decades a growing interest is observed in high energy ion implantation in order to form thick or buried layers with modified properties [2]. In this case the drastically increasing electronic energy deposition[1] can influence the implantation-induced damage formation in a many-sided way. On the one hand, the high electronic energy deposition can lead to creation of new defects, but on the other hand, it is able to transform or anneal already existing radiation damage. In order to predict the damage distribution resulting from MeV ion implantation under various irradiation conditions, it is desirable to study the influence of the electronic energy deposition, ε_e, separately from the other concomitant mechanism, that is, the nuclear energy deposition, ε_n. This can be done, e.g., by using swift heavy ions (SHI's) with energies in the range of several hundreds MeV, where the maximums of the depth distributions for $\varepsilon_e(z)$ and $\varepsilon_n(z)$ are well separated from each other.

It is worth mentioning that irradiation of various semiconductors with energetic ion or electron beams results in many-sided physical effects. Previously, Wie *et al.* [3] have suggested that perpendicular lattice strain produced with 15 MeV Cl irradiation in GaAs at 300 K is controlled by antisite defects and their complexes (antisite-vacancy, antisite-antisite, or antisite-interstitial pairs). It was observed that the strain saturates at $\approx 0.4\%$. The complete

---

[1] Though “electronic energy deposition” has a broader meaning, in the following this term will be used exclusively as a synonym of the linear energy transfer (LET, in units of energy/length) and denoted as ε_e.

recovery of the lattice strain occurs at about 700 K, which agrees with the recovery stage of isolated antisite defects in GaAs. In p-Ge a type conversion to n-Ge was found by Levalois *et al.* [4], and it was stated that the observed modification is a consequence of the formation of point defects during SHI irradiation (vacancy-oxygen or vacancy-doping impurity complex and divacancy). Later, Wesch *et al.* found that irradiation of GaAs with 10 MeV Se at 300 K caused only weak damaging in the depth region where ε_e dominates ε_n [5]. Primarily produced damage appeared to be much more stable in InP than in GaAs; it was found that the degree of damage annealing and transformation due to (relatively) high value of ε_e in GaAs is much higher than in InP [5]. Moreover, it was stated for GaAs that the higher the ε_e, the smaller the number of defects produced per vacancy. Then, Jencic *et al.* observed stimulated crystallisation of spatially isolated amorphous regions in Si, Ge and GaAs at 30 K and 300 K due to energetic electron beam irradiation [6, 7]. The crystallisation took place even when the energy of the electron beam was less than that required to create point defects in the crystalline material. However, in contrast to the ion beam-induced recrystallisation, electrons below the threshold displacement energy do not cause crystallisation of thick continuous amorphous layers but do cause crystallisation of spatially isolated amorphous zones [8].

Further, Herre *et al.* [9], Wesch *et al.* [10], Gaiduk *et al.* [11, 12], and Szenes *et al.* [13] reported on formation of amorphous continuous and discontinuous ion tracks (see Fig. 1.1),

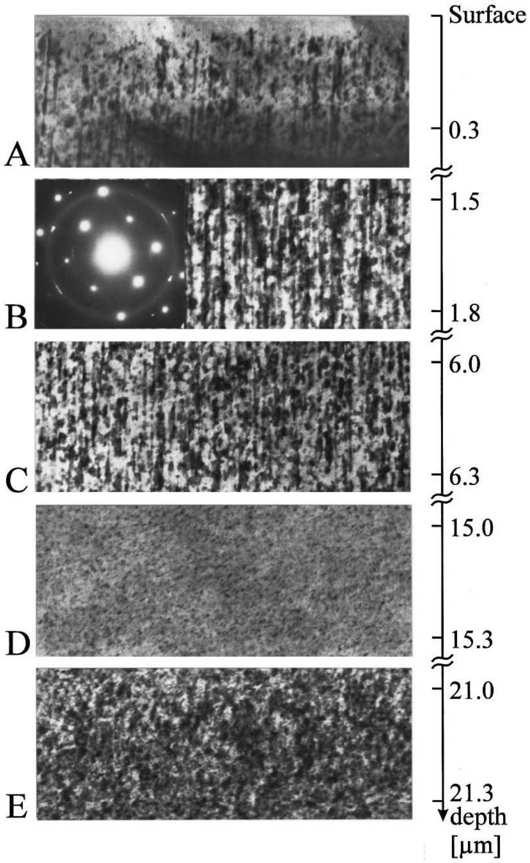

Fig. 1.1: Ion tracks in InP. Panorama-view XTEM images of InP irradiated at room temperature with 250 MeV Xe up to the fluence of 7x10^{12} ions/cm^2. Taken from [9].

high pressure (wurtzite) phase and amorphous layers in a depth region of dominating electronic energy loss for single-crystalline InP irradiated with swift Xe ions. The ion tracks were formed at room temperature (RT) and only *above some threshold electronic energy deposition* $\varepsilon_e^{thr} \approx 13$ keV/nm determined for fast Xe ions (lower values of ε_e were found to form point defects and defect clusters but not amorphous tracks). With ongoing SHI irradiation, the ion tracks begin to overlap, and extended amorphous layers are formed at sufficiently high ion fluences [9–11, 14]. And the last, the recent results of Wesch *et al.* [15–17] and Kamarou *et al.* [18–20] on effects of SHI irradiation in virgin and predamaged GaAs, InP, and Ge show that depending on the ion mass, ion energy and the irradiation temperature, the bombardment with various SHI's causes damage formation in the virgin materials (much more noticeable in InP than in GaAs or Ge) and more or less pronounced damage annealing in the predamaged ones. Furthermore, it was shown that both the *damage formation* and *damage annealing* occur *simultaneously* during SHI irradiations [18].

There are four main competing mechanisms of the ion track formation in solids due to high electronic energy deposition that are discussed in literature: Coulomb explosion [21–24], shock waves [25–27], lattice-relaxation (also called "athermal melting") [28–30], and inelastic thermal spikes[2] (i-TS) [13, 31–34] dating back to Desauer [35] and Seitz and Koehler [36]. The TS model of track formation is a well established approach that has been successfully applied to some metals, intermetallic compounds and dielectrics [37–41]. Because of the complexity of all energy relaxation processes involved, this model is also subjected to criticism [42–44] like all models mentioned above. However, the TS model seems to be the most elaborated one; furthermore, to our knowledge, currently it is the only model being able to provide at least approximate predictions on track formation in numerous conducting and nonconducting targets.

The TS model suggests that the energy is transferred to the lattice via electron-phonon coupling (see Sect. 5.1 and 5.2), which leads to an increase in the lattice temperature. If this increase surpasses the melting point, the material can melt. In this way the following fast cooling (also called "fast quenching") of the molten zone can freeze the resulting damage in and thus leave an ion track behind.

To our knowledge, no experimental results available in literature directly prove that a SHI passing through matter causes a local melting of the target material at the ion path and close to it. As a rule, the resulting effects (e.g., various phase transformations in simple or layered structures, or modifications of the existing surfaces and interfaces, etc.) are registered and measured on a time scale that is incommensurable with the characteristic time intervals of the basic processes being the first cause of the changes observed.[3]

---

[2] In the following it is referred to as "thermal spike model" or "TS model" for short.

[3] The "microscopical" (more precisely, "nano-scale") processes triggered by a SHI penetrating the matter usually last not longer than 10^{-13}–10^{-10} s, whereas the conventional methods (RBS, TEM, SIMS, optical ones, etc.) demand many orders of magnitude larger time spans for collecting a spectrum or acquiring an image even if applied *in situ*.

Nevertheless, some observed effects support the idea of the local melting indirectly. One of such effects is the well-known intermixing in layered structures by swift heavy ions [45–51]. It was shown that the mixing takes place only in above-threshold regimes (regarding the value of ε_e), and the respective threshold is determined by the more radiation-resistant material of the corresponding structure [45]. The last conclusion gives a clear indication that an efficient intermixing occurs only if both sides of the interface are locally molten by SHI's. Furthermore, for all experimental conditions favouring the intermixing[4] the effect is governed by very efficient interdiffusion of the constituent atoms [49, 50]. This diffusion is too fast to be ascribed to solid-state processes, because the respective diffusion coefficients (from about 10^{-4} to 10^{-2} $\mathrm{cm}^2\mathrm{s}^{-1}$) are several orders of magnitude larger than the solid-state ones. In fact, such diffusion coefficients are characteristic to *liquid-state diffusion*, which supports again the idea that the interface mixing results from the transient interdiffusion in the molten tracks of the SHI's.

Generally, SHI irradiation of virgin InP in the electronic stopping regime causes the formation of small-size defects, i.e., simple point defects and point defect clusters. Additionally to the simple defects mentioned above, more complex elongated defects such as ion tracks are formed due to high electronic energy loss ε_e in the above-threshold electronic regime (i.e., for SHI's with $\varepsilon_e \geq \varepsilon_e^{thr}$) and within a limited range of irradiation temperatures [9–11, 13]. The main points being discussed in literature are the correlation between the number of ion tracks and the ion fluence in virgin and predamaged InP [9, 10, 52], the origin of the discontinuous tracks [9, 10, 52], the wide distribution of track diameters [9], the influence of the irradiation temperature [10, 11], and the internal structure of ion tracks in InP [9–11, 52]. However, it is worth mentioning that explanations, proposed by different authors on some of the points listed above, are sometimes mutually contradictory. Further, as it was shown by us previously, the efficiency of the damage formation and accumulation in InP cannot be explained solely by the ion energy loss, but the radial distribution of the energy deposition has to be taken into account [18, 20]. This conclusion prejudices the amenity of a *single value* of the ε_e^{thr} as a *fundamental quantity* that is commonly used for the description of the track formation in solids irradiated with *different ion species* and at *different temperatures* [20].

The current work is devoted to many-sided effects of damage formation and annealing in virgin and conventionally predamaged Ge, GaAs and InP irradiated with SHI's at different experimental conditions. The main purpose is to analyse the obtained experimental data and try to offer a self-consistent way to explain the influence of various irradiation conditions on the formation and annealing of defects.

---

[4] Its efficiency is primarily dependent on the ion energy loss and on the irradiation temperature.

Chapter 2

Basics

2.1 Projectile-target interaction

Let us consider a non-relativistic atomic or ionic projectile with energy E moving in a solid target. Such a movement results in a mutual interaction between the projectile and the target atoms. Basically, there are three main interaction mechanisms: *nuclear* and *electronic scattering* (called also *elastic* and *inelastic scattering*, respectively), and *nuclear reactions*. The first mechanism is realised if both of the colliding partners (the projectile and a target atom) preserve their internal states, but can change their velocities and directions of movement according to the conservation laws for the total momentum and energy. Contrary, the second mechanism implies that the electronic states are changed as a result of the collision, which violates the conservation of the total momentum. The third mechanism becomes efficient only for fast light ions penetrating targets composed of light atoms, nevertheless, even in such cases the corresponding cross-sections are very small as compared to those for the electronic and nuclear scattering. Thus, in the following we will not give attention to the nuclear reactions as one of the interaction mechanisms. The other two interaction mechanisms are significant in the cases studied here, and with respect to the participating particles, the projectile-target interaction can be divided into three main types:

1. Internuclear repulsion (*elastic ion scattering*),
2. Attraction or capture of target electrons by the projectile nucleus,
3. Attraction or capture of projectile electrons by target nuclei.

The second and the third types (*inelastic ion scattering*) cause an excitation or ionisation of target atoms and projectiles, respectively. Further, they jointly determine the dynamics of the momentary ion charge (ionisation degree) q. The ion slowing down is determined by a combined action of all basic interaction types mentioned above. Using a fairly good approximation of no correlation between the electronic and nuclear processes (i.e., elastic and inelastic scattering occurs independently [53]), we obtain

$$S_{total}(E) = S_n(E) + S_e(E), \tag{2.1}$$

where S_n, S_e, and S_{total} are the nuclear, the electronic, and the total stopping cross-sections, respectively. These cross-sections determine the respective contributions to the ion energy loss:

$$\varepsilon_n(E) = -\left(\frac{dE}{dz}\right)_n = N_a S_n(E); \quad \varepsilon_e(E) = -\left(\frac{dE}{dz}\right)_e = N_a S_e(E), \tag{2.2}$$

where N_a is the atomic density of the target.

2.2 Nuclear energy loss

In the case of Coulomb interaction (i.e., for bare ions) the differential cross-section $d\sigma_n(T)$ for transferring some amount of energy T from an ion with energy E, atomic number Z_1 and mass M_1 to an atomic nucleus of the target with atomic number Z_2 and mass M_2 during a nuclear collision is given by [53]

$$d\sigma_n(T) = \begin{cases} B_n T^{-2} dT, & \text{for } T \leq T_{max} \\ 0, & \text{for } T > T_{max} \end{cases}, \tag{2.3}$$

where T_{max} is the maximum energy that can be transferred in a single collision (the so-called *kinematic limit*)

$$T_{max} = \frac{4M_1M_2}{(M_1+M_2)^2}E \tag{2.4}$$

and

$$B_n = \pi\left(\frac{b_n}{2}\right)^2 T_{max}\,, \tag{2.5}$$

where b_n is the collision diameter (the minimum distance of approach for a head-on collision).

If the interaction is described by the Coulomb potential

$$V(r) = \frac{Z_1Z_2e_0^2}{4\pi\varepsilon_0}\frac{1}{r}, \tag{2.6}$$

then

$$b_n = \frac{Z_1Z_2e_0^2}{4\pi\varepsilon_0 E_{cm}}, \tag{2.7}$$

where e_0 is the electron charge, ε_0 is the vacuum permittivity, and E_{cm} is the energy of the two colliding particles in the centre-of-mass system:

$$E_{cm} = \frac{M_2}{M_1+M_2}E\,. \tag{2.8}$$

Substituting Eqs. (2.7) and (2.8) into Eq. (2.5) gives

$$B_n = \pi \frac{M_1}{M_2} \left(\frac{Z_1 Z_2 e_0^2}{4\pi\varepsilon_0} \right)^2 \frac{1}{E} . \tag{2.9}$$

For ion-atomic collision events with a non-zero impact parameter s the transferred energy T is given by [53]

$$T(s) = \frac{(b_n/2)^2}{(b_n/2)^2 + s^2} T_{max}. \tag{2.10}$$

Obviously, the transferred energy rapidly decreases with increasing the impact parameter.

2.3 Electronic energy loss

The collision of a bare projectile with a free electron at rest can be described similarly to the nuclear interactions by using the formulae given in Sect. 2.2:

$$d\sigma_e = \begin{cases} B_e T^{-2} dT, & \text{for } T \leq T_{e,max} \\ 0, & \text{for } T > T_{e,max} \end{cases} . \tag{2.11}$$

Because the electron mass $m_e << M_1$,

$$T_{e,max} \cong 4 \frac{m_e}{M_1} E , \tag{2.12}$$

and

$$B_e \cong \pi \frac{M_1}{m_e} \left(\frac{Z_1 e_0^2}{4\pi\varepsilon_0} \right)^2 \frac{1}{E} . \tag{2.13}$$

For indirect collisions with a non-zero impact parameter s the energy T_e transferred from the projectile to the target electron is given by

$$T_e(s) = \frac{(b_e/2)^2}{(b_e/2)^2 + s^2} T_{e,max} , \tag{2.14}$$

where

$$b_e = \frac{Z_1 e_0^2}{4\pi\varepsilon_0} \frac{M_1}{m_e} \frac{1}{E} . \tag{2.15}$$

2.4 Nuclear versus electronic stopping

The comparison of the respective equations in Sects. 2.2 and 2.3 yields the following expressions:

$$\frac{T_{e,max}}{T_{max}} = \frac{m_e}{M_2}\left(\frac{M_1+M_2}{M_1}\right)^2 << 1,$$

$$\frac{b_e}{b_n} = \frac{1}{Z_2}\frac{M_1M_2}{m_e(M_1+M_2)} >> 1,$$

$$\frac{B_e}{B_n} = \frac{1}{Z_2^2}\frac{M_2}{m_e} >> 1.$$

Therefore, the maximum energy that can be transferred in a single head-on nuclear collision is much higher than that for a single electronic collision. For example, in the extreme case where $M_1 = M_2$, the whole amount of the ion energy E can be transferred to an atomic nucleus of the target. Contrary, only a very small amount of the ion energy can be acquired by an individual electron due to the large difference in their masses ($m_e << M_1$). However, the nuclear energy transfer decreases more rapidly with increasing impact parameter s than the electronic energy loss does [53]. Furthermore, because $B_e >> B_n$, the cross-section for the electronic energy loss is much larger than that for the nuclear energy loss. To sum up, with increasing ion energy, the probability of nuclear collisions with large scattering angles (where T is close to T_{max}) diminishes drastically and the ion slowing down is mainly due to the electronic stopping processes.

Chapter 3

Experiments

We have used nominally undoped <100>±0.5° single-crystalline Ge, GaAs, and InP wafers that were cut into pieces (typically, from 5x5 mm^2 to 8x8 mm^2 large samples). The samples were irradiated either at room temperature (RT, about 300 K) or at liquid nitrogen temperature (LNT, about 80 K) with various swift heavy ion (SHI) beams at the Ionenstrahllabor[1] (ISL) of the Hahn-Meitner-Institut[2] Berlin (HMI). Further, in order to study the effect of the high electronic energy deposition on already existing defects introduced by conventional ion implantation, we first predamaged the Ge, GaAs, and InP samples (see Sect. 3.1 for details) and afterwards irradiated them with various SHI's as described within Sect. 3.2.

Some selected structural and thermal properties of the investigated materials are presented in Table 3.1.

Property / Material	Ge	GaAs	InP
Structure	Diamond	Zinc Blende	Zinc Blende
Space group	Fd3m	F$\bar{4}$3m	F$\bar{4}$3m
Lattice Parameter a_0	0.566 nm	0.565 nm	0.586 nm
Mass density (solid) ρ_s	5.32 g/cm^3	5.32 g/cm^3	4.79 g/cm^3
Mass density (liquid) ρ_l	5.51 g/cm^3	5.71 g/cm^3	5.10 g/cm^3
Atomic concentration N_a	4.42x10^{22} cm^{-3}	4.42x10^{22} cm^{-3}	3.96x10^{22} cm^{-3}
Nature of energy gap	indirect	direct	direct
Energy gap E_g	0.66 eV	1.42 eV	1.34 eV
Thermal conductivity	59 W/(m·K)	58 W/(m·K)	72 W/(m·K)
Specific heat	0.31 J/(g·K)	0.33 J/(g·K)	0.31 J/(g·K)
Melting point T_m	1210 K	1513 K	1335 K
Latent heat of fusion H_m	36.9 kJ/mol	96.7 kJ/mol	62.7 kJ/mol

Tab. 3.1: Selected properties of materials investigated. Basic and thermal properties of Ge, GaAs, and InP at 300 K. The data are from Refs. [54–57].

---

[1] `http://www.hmi.de/isl`

[2] `http://www.hmi.de`

3.1 Predamaging of samples

The Ge, GaAs, and InP samples were predamaged at the 400 kV implanter[3] “ROMEO” of the Institut für Festkörperphysik[4] (IFK) of the Friedrich-Schiller-Universität[5] (FSU) with 300 keV N, 600 keV Ge or 600 keV Se ions at LNT. During the implantation, the samples were tilted by 7 degrees from normal incidence to minimise channelling. To achieve different damage levels between crystalline virgin and amorphised material, different ion fluences were used (see Table 3.2).

Material	Ion	E	N_I (cm^{-2})	T_I	R_D (nm)	R_p (nm)
Ge	N	300 keV	8x10^{13}	LNT	390	460
	Ge	600 keV	1x10^{13}	LNT	140	278
GaAs	Se	600 keV	1x10^{13}-1x10^{14}	LNT	135	230
	Ge	600 keV	1x10^{13}-2.5x10^{13}	LNT	150	250
InP	Ge	600 keV	4x10^{12}-2.5x10^{13}	LNT	160	275

Tab. 3.2: Predamaging of Ge, GaAs, and InP samples. Ion energy E, range of ion fluences N_I, irradiation temperature T_I, depth of the maximum nuclear energy deposition R_D, and projected ion range R_p. The values of R_D and R_p were calculated with the SRIM-2003 code [58].

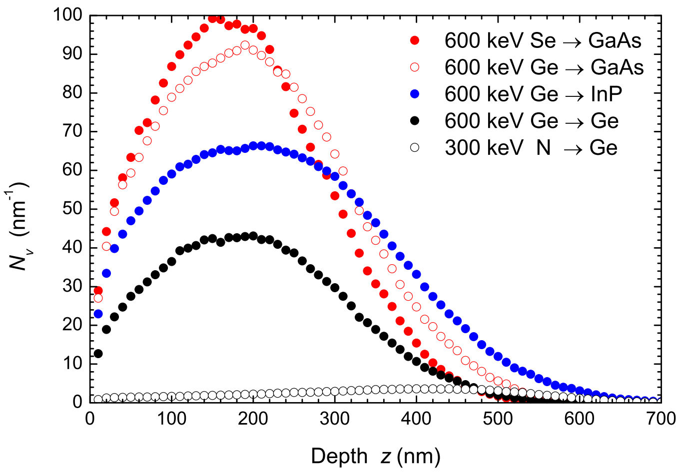

Fig. 3.1: Predamaging of samples. Number of vacancies N_v per ion and unit path length versus depth z, as calculated with SRIM-2003 [58]) for Ge, GaAs, and InP predamaged by means of conventional ion implantation (see Table 3.2).

Figure 3.1 shows calculated depth distributions of the radiation damage (obtained by using the SRIM-2003 code [58]) formed in Ge, GaAs or InP for different ion species and energies used. One can see that for all experimental conditions listed in Table 3.2 the predamaged layers in the Ge, GaAs, and InP samples are located within the depth region of $0 \leq z \leq 0.7$ μm.

---

[3] http://www.physik.uni-jena.de/~exphys/ionen/equipment/isl/equipment_isl_e.html

[4] http://www.physik.uni-jena.de/exp_phys

[5] http://www.uni-jena.de

3.2 SHI irradiation

The virgin and predamaged Ge and GaAs samples were irradiated at RT or LNT with 140 MeV $^{86}Kr^{10+}$, 390 MeV $^{129}Xe^{21+}$ or 593 MeV $^{197}Au^{30+}$ ions (see Table 3.3).

Material	Ion	E (MeV)	N_I (cm^{-2})	T_I	ε_e (keV/nm)	ε_n (keV/nm)	N_v (nm^{-1})
Ge	Kr	140	$1x10^{14}$-$2x10^{14}$	RT	14.2	0.036	0.69
	Xe	390	$3x10^{12}$-$4x10^{15}$	RT	24.3	0.047	0.79
	Au	593	$5x10^{11}$-$3x10^{14}$	RT	32.8	0.105	1.49
GaAs	Kr	140	$4x10^{13}$-$2x10^{14}$	RT	14.0	0.038	1.52
	Xe	390	$3x10^{12}$-$3x10^{14}$	RT, LNT	24.6	0.042	1.74
	Au	593	$1x10^{13}$-$3x10^{14}$	RT	33.3	0.091	3.37

Tab. 3.3: SHI irradiations of Ge and GaAs. Ion energy E, range of ion fluences N_I, irradiation temperature T_I, electronic (ε_e) and nuclear (ε_n) energy loss, and number of vacancies N_v per ion and unit path length. The values of ε_e, ε_n, and N_v were calculated with the SRIM-2003 code [58] using a displacement energy E_d of 20 eV for Ge [59] and 9.6 eV for GaAs [60].

The virgin and predamaged InP samples were irradiated with 140 MeV $^{86}Kr^{10+}$, 250 MeV $^{129}Xe^{17+}$, 390 MeV $^{129}Xe^{21+}$ or 593 MeV $^{197}Au^{30+}$ ions at RT or LNT. Besides, thin aluminium (Al) foils with different thickness (from 0.8 μm to several tens of μm) were placed in front of some samples to obtain lower ion energies and, at the same time, to bring the projectiles into the mean equilibrium charge state (see Table 3.4).

Ion	E (MeV)	E/M_1 (MeV/u)	q_{init}	q_{mean}	N_I (cm^{-2})	T_I	ε_e (keV/nm)	ε_n (keV/nm)	N_v (nm^{-1})
					Without Al foils				
Kr	140	1.63	10	22.3	$4x10^{12}$-$2x10^{15}$	RT	12.1	0.039	1.2
Xe	250	1.94	17	31.3	$1x10^{12}$-$1x10^{14}$	RT	20.0	0.060	2.0
Xe	390	3.02	21	34.7	$3x10^{11}$-$3x10^{14}$	LNT, RT	21.5	0.042	1.4
Au	593	3.01	30	46.3	$7x10^{10}$-$1x10^{13}$	LNT, RT	29.1	0.078	2.5
					With Al foils				
Xe	82	0.64	*	22.9	$2x10^{12}$-$1x10^{14}$	RT	13.5	0.165	4.9
Xe	193	1.50	*	29.4	$2x10^{12}$-$3x10^{13}$	RT	18.6	0.080	2.4
Xe	375	2.91	*	34.4	$8x10^{11}$-$9x10^{12}$	RT	21.5	0.044	1.5
Au	64	0.32	*	23.0	$5x10^{11}$-$9x10^{13}$	RT	10.7	0.568	15.2
Au	79	0.40	*	25.0	$5x10^{11}$-$9x10^{13}$	RT	12.6	0.500	13.0
Au	150	0.76	*	31.3	$2x10^{11}$-$2x10^{13}$	RT	18.8	0.259	7.5
Au	573	2.91	*	45.9	$1x10^{11}$-$5x10^{12}$	RT	28.9	0.091	2.9

Tab. 3.4: SHI irradiations of InP. Ion energy E, specific ion energy E/M_1 (M_1 is the ion mass), initial ion charge q_{init}, equilibrium ion charge in the target bulk q_{mean}, range of ion fluences N_I, irradiation temperature T_I, electronic (ε_e) and nuclear (ε_n) ion energy loss at the surface, number of vacancies per ion and unit path length N_v. '*' symbols: q_{init} is expected to be close to q_{mean}. The values of ε_e, ε_n, and N_v were calculated with the SRIM-2003 code [58] using a displacement energy E_d of 8.0 eV [61].

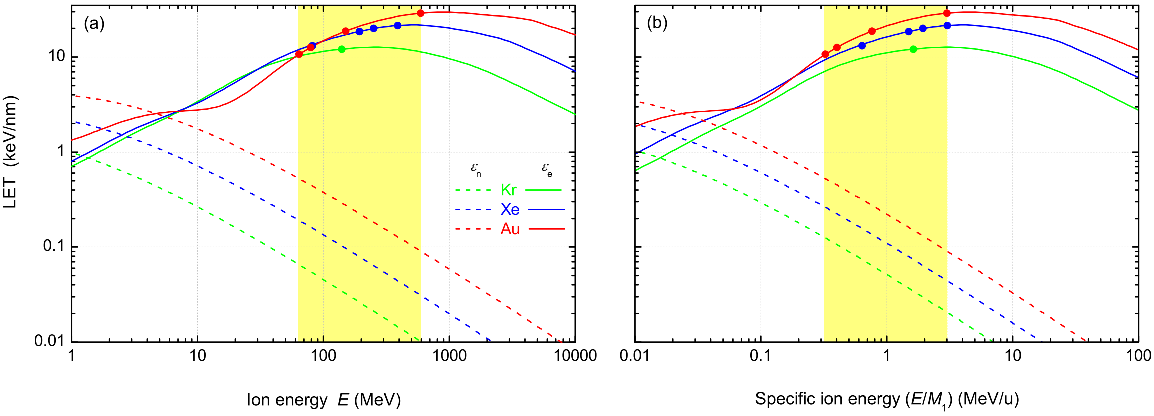

Fig. 3.2: Energy dependence of ε_n and ε_e. Nuclear (ε_n) and electronic (ε_e) energy loss of Kr, Xe, and Au in InP versus (a) ion energy E or (b) specific ion energy E/M_1 (SRIM-2003 [58] calculations). The performed irradiations are illustrated by the data points on the respective $\varepsilon_e(E)$ curves, and the yellow area covers the whole interval of the ion energies used (see Table 3.4).

Ion beam scanning was used in order to perform a uniform irradiation of all materials investigated. Further, to prevent heating of the samples during the SHI irradiations, the ion flux was kept low (typically, not higher than 5x10^{10} cm^{-2}s^{-1}), and the samples were mounted to the sample holder with silver paste giving a good thermal contact between them.

It should be mentioned that for all SHI irradiation performed the electronic energy loss ε_e increases and the nuclear one ε_n decreases with increasing energy E (or, equivalently, specific energy E/M_1 or velocity v) of the ions. This is illustrated in Fig. 3.2, where the energy dependences of ε_n and ε_e in InP are shown for all ion species used (Kr, Xe, and Au). Consequently, no Bragg peaks are expected in the respective depth distributions of ε_e, i.e., the value of ε_e continuously decreases starting from the very surface (provided that the initial ion charge equals the equilibrium one in the target bulk). This is well demonstrated in Fig. 3.3 showing the depth dependences of the electronic (ε_e) and nuclear (ε_n) energy deposition in InP for selected SHI species. One can see in Fig. 3.3 that for all ion species represented

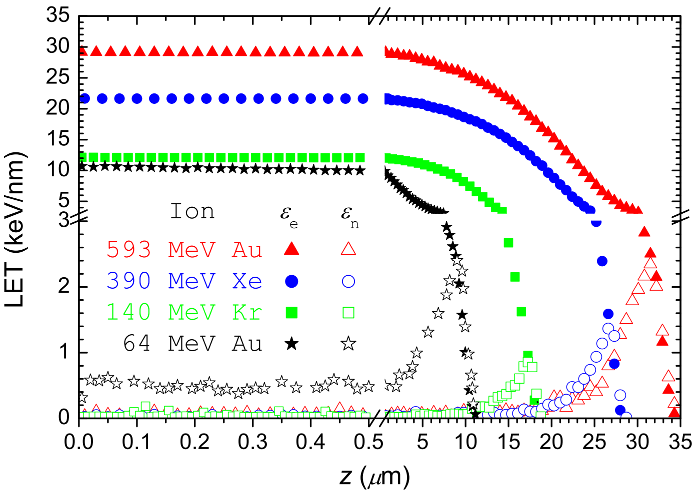

Fig. 3.3: SHI's energy loss. Depth dependence of the electronic and nuclear energy deposition [20] for selected ion species (SRIM-2003 [58] calculations). Please, note the breaks in both axes.

the depth distributions of both ε_e and ε_n are almost uniform, and $\varepsilon_e >> \varepsilon_n$ within the first 0.5 μm depth. This holds also for other ion species listed in Table 3.4. Further, Figs. 3.2 and 3.3, as well as Table 3.4 prove that irradiations with SHI beams decelerated by thin Al foils (excluding 193 MeV Xe, 375 MeV Xe, and 573 MeV Au) are characterised by noticeably higher nuclear stopping, than those in the first part of Table 3.4 (140 MeV Kr, 250 MeV Xe, 390 MeV Xe, and 593 MeV Au). Consequently, in the former case one can expect a larger influence of the nuclear energy deposition on the radiation damage formation.

3.3 Investigation methods

3.3.1 Rutherford backscattering spectrometry (RBS)

The irradiated samples were analysed by means of Rutherford backscattering spectrometry (RBS) in combination with the channelling technique using 1.4 MeV He ions at a laboratory scattering angle of 168°. This was done using the 3 MV Tandetron accelerator[6] “JULIA” of the Institut für Festkörperphysik of the Friedrich-Schiller-Universität (Jena, Germany). Under these conditions the depth which can be analysed in a quantitative manner in InP is approximately 0.6 μm. As a measure for the damage concentration within the irradiated layers the difference in minimum yield $\Delta\chi_{min}$ was taken. It is determined from the channelling spectra as a function of the depth z by

$$\Delta\chi_{\mathrm{min}}(z) = \frac{Y_{aligned}^{irradiated}(z) - Y_{aligned}^{virgin}(z)}{Y_{random}(z) - Y_{aligned}^{virgin}(z)},$$

where $Y_{aligned}^{virgin}(z)$ and $Y_{aligned}^{irradiated}(z)$ are the RBS yields of the aligned spectra (nonirradiated virgin and irradiated samples, respectively); $Y_{random}(z)$ is the yield measured in random direction. Assuming a random distribution of displaced lattice atoms within the lattice cell, the depth distributions of the relative concentration of displaced lattice atoms, $n_{da}(z)$, were calculated from the measured $\Delta\chi_{min}(z)$ values. These calculations were performed using the DICADA code [62] that is based on the discontinuous model of dechannelling. In the following the relative concentration of displaced lattice atoms, n_{da}, is referred to as “damage concentration” for short. $n_{da} = 0$ and $n_{da} = 1$ correspond to undamaged virgin and to very heavily damaged (amorphised) material, respectively.

---

[6] `http://www.physik.uni-jena.de/~exphys/ionen/equipment/isl/equipment_isl_e.html`

3.3.2 Transmission electron microscopy (TEM)

Some samples selected on the basis of the RBS results were additionally studied using transmission electron microscopy (TEM) in cross-section (X) and plan-view (PV) geometry. The thinned (transparent for electrons) samples for PV-TEM were prepared by means of chemical etching performed either before SHI irradiations or after them. All the X-TEM samples were thinned down after SHI irradiations, using a mechanical polishing followed by a final ion beam milling. The TEM investigations were performed using either a Hitachi H-800 instrument[7] or a JEOL JEM-3010 instrument[8] operating at 200 kV or 300 kV, respectively.

3.3.3 Secondary ion mass spectrometry (SIMS)

As it was discussed in Chapter 1 (see p. 5), experiments on intermixing of layered structures are potentially capable to provide an important information on the local melting of the target matter inside SHI tracks. Therefore, we prepared several sets of bulk GaAs and InP samples and covered them with a relatively thin (tens of nm) surface metallic layer of Bi by means of a thermal (vapour) deposition. Because the respective threshold is determined by the less sensitive material [45], it is reasonable to select a material with a low radiation-resistance.[9]

Afterwards, these samples were irradiated with 593 MeV Au ions at RT. Finally, the reference and the irradiated samples were investigated by means of SIMS. This was performed by using a Cameca IMS-4f facility.[10] The analysis has been carried out by a 12.3 keV O_2^+ primary beam. The duration of the analysis amounted to 7 minutes in all cases.

---

[7] Research & Design Company "Belmicrosystems" (`http://www.bms.by/research/bma_e.htm`)

[8] Institut für Materialwissenschaft und Werkstofftechnologie of the Friedrich-Schiller-Universität Jena (`http://www2.uni-jena.de/matwi/wiss_forsch/start.html.en`)

[9] According to Dufour *et al.* [37] and Wang *et al.* [39, 63], such metals as Ti, Fe, Co, Ni, Zr, and Bi are the most sensible ones with regard to SHI irradiation. Therefore, they are the best candidates. Taking further into account the respective melting points (Ti: 1933 K, Fe: 1808 K, Co: 1768 K, Ni: 1726 K, Zr: 2125 K, and Bi: 545 K), Bi seems to be the best choice.

[10] See footnote 7.

Chapter 4

Experimental results on swift heavy ion irradiations

As it will be shown below, different semiconductors demonstrate different radiation resistance to high electronic energy deposition during SHI irradiation. It turns out, for instance, that virgin Ge and GaAs are much more radiation-resistant to SHI irradiation than virgin InP. Therefore, it is expedient to consider Ge and GaAs separately from InP.

4.1 Damage formation in virgin Ge and GaAs

As an example, Fig. 4.1 shows the evolution of the radiation damage in Ge bombarded with 390 MeV Xe at RT. Part (a) of the figure represents RBS spectra, and part (b) illustrates the corresponding depth distributions of the damage concentrations calculated using the DICADA code (see Sect. 3.3.1).

Fig. 4.1(b) shows that for the highest fluence of 390 MeV Xe applied (4x10^{15} cm^{-2}) the damage concentration is lower than 0.03, i.e., less than 3% of the target atoms are

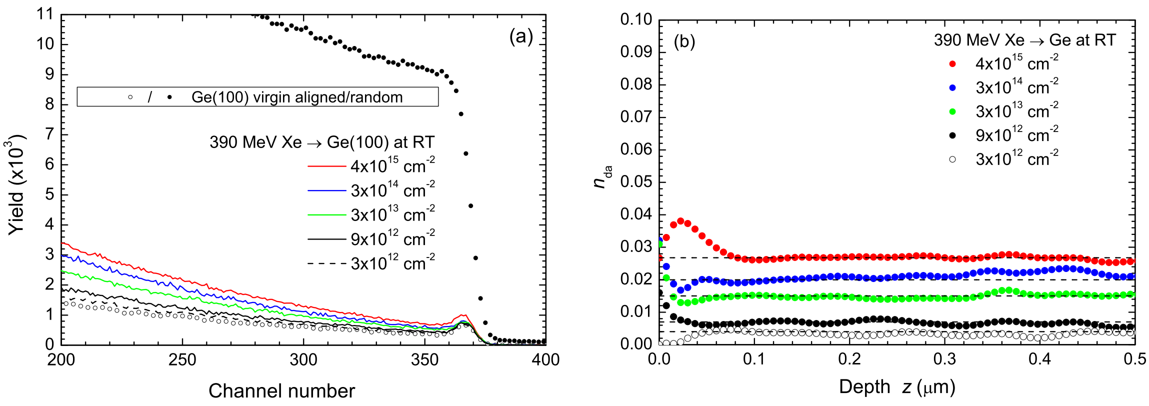

Fig. 4.1: Irradiation of virgin Ge with 390 MeV Xe at RT. (a) RBS spectra of virgin Ge(100) irradiated with different fluences of 390 MeV Xe at RT, and (b) the corresponding depth distribution of the radiation damage concentration n_{da}.

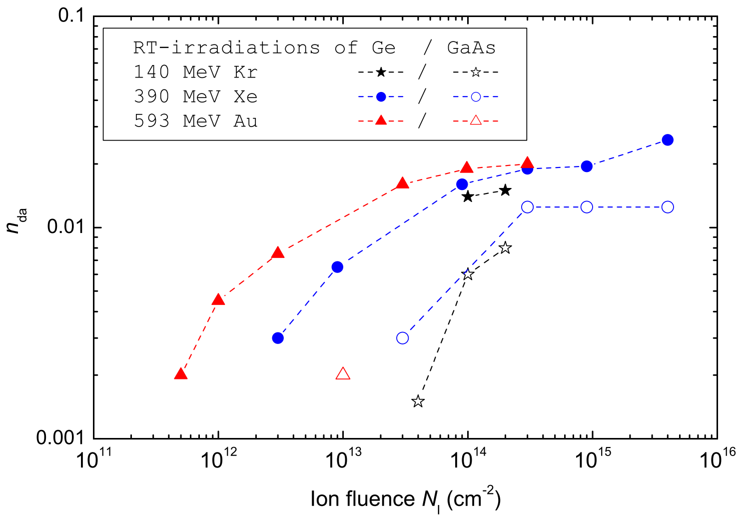

Fig. 4.2: RT-irradiation of Ge and GaAs. Fluence dependence of the damage concentration (n_{da}) formed at RT in Ge and GaAs by various ion beams. The dashed lines connecting the data points are drawn merely to guide the eye.

displaced from their regular lattice positions. Let us now try to determine to which extent the observed low efficiency of the damage formation and accumulation in Ge can be ascribed to the (relatively high) electronic or to the (relatively low) nuclear energy loss (see Table 3.3). Usually the number of displacements per lattice atom n_{dpa} is taken to quantify the nuclear energy deposition with $n_{dpa} = N_v N_I / N_a$, where N_v and N_I are the calculated number of vacancies per ion and unit path length and the ion fluence, respectively (see Table 3.3), and N_a = 4.42x10^{22} cm^{-3} is the atomic density of Ge (see Table 3.1). Therefore, for N_I = 4x10^{15} cm^{-2}, $n_{dpa} = 0.71$ dpa. The large difference between the calculated value of 71% and the measured one of ≈ 3% indicates that the radiation damage formed in single atomic cascades is not stable. This instability can be explained, e.g., by *efficient diffusion* and *annihilation* of point defects in Ge (provided that they are mobile at RT), or by the *damage annealing* due to the high electronic energy deposition ε_e.

Fig. 4.2 summarises the measured damage concentration n_{da} (taken at depth of 200 nm) as a function of the ion fluence. For the sake of comparison, the corresponding data for GaAs are presented along with that for Ge. The figure allows one to conclude that GaAs is slightly more radiation-resistant to SHI irradiation at RT than Ge. Further, it gives an indication that the damage concentration in GaAs saturates at a relatively low level (≈ 1.3%).[1] The obtained results thus demonstrate that both damage formation and damage annealing processes occur *simulaneously* in Ge and GaAs irradiated by swift heavy ions.

---

[1] The observed saturation correlates qualitatively with that observed by Huber *et al.* [64] in crystalline Ge irradiated with various swift ions.

4.2 Damage annealing in predamaged Ge and GaAs

This section deals with effects of SHI irradiation on Ge and GaAs predamaged by conventional implantation of ions having energies of several hundreds keV (see Sect. 3.1).

Figure 4.3 demonstrates the effect of SHI irradiation on the predamaged Ge. One can see that RT-irradiation of the predamaged Ge with 140 MeV Kr causes very noticeable damage annealing. So, the initial damage concentration in the maximum of the depth distribution ($n_{da}^{init.max}$) amounts to ca. 0.77 in the as-implanted material [see Fig. 4.3(b)]. This value is reduced to about 0.22 for the highest fluence of 140 MeV Kr used. This significant annealing of the predamaged Ge by different SHI is very similar to that previously observed in predamaged GaAs due to 390 MeV Xe irradiation [15]. It is worth mentioning that molecular-dynamics computer simulations of atomic cascades in similar material (Si) showed no effect of annealing in the Si atomic cascades; instead the preexisting damage, if it has any effect at all, enhances damage production [65]. Thus, the efficient annealing has to be attributed to the *high electronic energy deposition*.

A similar effect of the damage annealing in predamaged GaAs due to SHI irradiation at RT is illustrated by Fig. 4.4. Parts (a), (b), and (c) of the figure comprise the experimental data for 140 MeV Kr, 390 MeV Xe, and 593 MeV Au, respectively. Fig. 4.4 shows that for the largest ion fluences used, the damage concentration is decreased from 83-92% to 11-16%. The corresponding results for different predamage levels show that the efficiency of the observed annealing in GaAs depends on the initial concentration of damage $n_{da}^{init.max}$. The smaller the initial damage concentration $n_{da}^{init.max}$ is, the higher is the relative annealed fraction (RAF) of the damage. The last value is determined as $(n_{da}^{init.max} - n_{da}^{max})/n_{da}^{init.max}$, where $n_{da}^{init.max}$ and n_{da}^{max} are the concentrations of the displaced lattice atoms in the maximum of the distributions for the pre-damaged and SHI post-irradiated samples, respectively.

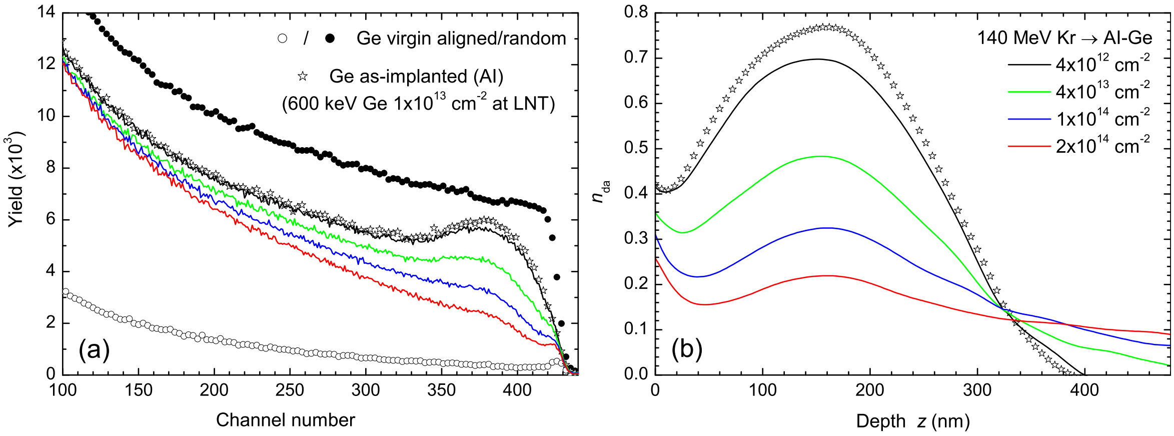

Fig. 4.3: Irradiation of predamaged Ge with 140 MeV Kr at RT. (a) RBS spectra and (b) the corresponding damage concentration *vs.* depth for Ge predamaged with 600 keV Ge (1x10^{13} cm^{-2} at LNT) and afterwards irradiated with different fluences of 140 MeV Kr at RT. The description of lines is valid for both parts of the figure.

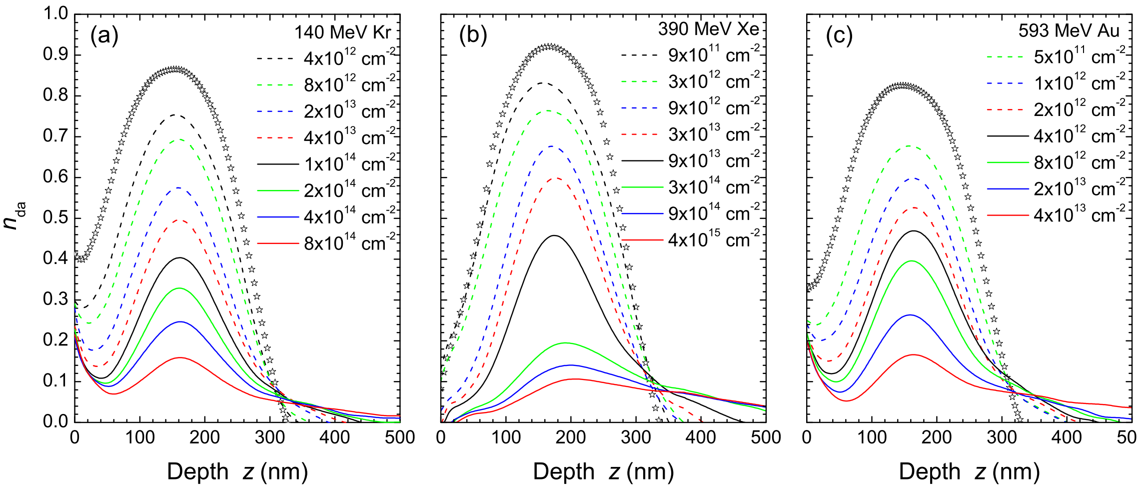

Fig. 4.4: SHI irradiation of predamaged GaAs. Damage concentration vs. depth for GaAs predamaged at LNT with 600 keV Ge (a) 2x10^{13} cm^{-2}, (b) 2.5x10^{13} cm^{-2}, (c) 2x10^{13} cm^{-2}, and afterwards irradiated with different fluences of 140 MeV Kr, 390 MeV Xe, or 593 MeV Au at RT. The open symbols in all parts of the figure stand for the depth distributions of the relative concentration of the predamage.

As an example, Fig. 4.5 shows the relative annealed fraction as a function of $n_{da}^{init.max}$ in predamaged GaAs samples post-irradiated with 390 MeV Xe at RT. For $n_{da}^{init.max} \leq 0.75$, the annealed fraction is between 80% and 90% at the highest Xe fluence.[2] This corresponds to a remaining damage of $n_{da} \approx 0.05$. However, if $n_{da}^{init.max} > 0.75$, then a considerable decrease of the RAF with increasing $n_{da}^{init.max}$ is observed, and in the case of thick heavily damaged layers only between 6% and 18% of the initial damage are annealed. Finally, for very high predamage levels ($n_{da} = 1$ for a broad interval of depths) and, consequently, for very thick amorphous layers (most probably, with no crystalline inclusions inside) there is hardly any annealing or no annealing at all. This is further illustrated in Fig. 4.6, where three obviously different cases are shown. Despite $n_{da}^{init.max} = 1$ is valid for all three initial distributions, only the last one [Fig. 4.6(c)] is for completely amorphous layers ($z \leq 240$ nm). The transition region (240 nm $< z <$ 380 nm) contains damaged but not amorphised material; therefore, the SHI post-irradiation results in the annealing and, consequently, causes a slight shift of the amorphous-crystalline interface [Fig. 4.6(c)]. The two other cases [Figs. 4.6(a) and (b)] represent the effect of annealing in heavily damaged (and partially amorphised) material. One can see that the highest Xe ion fluence used leads to a noticeable annealing of predamaged GaAs from the initial value of $n_{da} = 1$ in the maximum of the depth distribution down to approx. 0.45 or 0.82 [see parts (a) and (b), respectively]. The initial fraction of the amorphous material is thus obviously lower in the case illustrated in Fig. 4.6(a) than in the case of Fig. 4.6(b).

The observed dependence of the RAF on $n_{da}^{init.max}$ (see Fig. 4.5) indicates that the anneal-

---

[2] The results of our additional investigations, performed with the same experimental conditions but predamaging with 600 keV Se ions instead of 600 keV Ge are shown in Fig. 4.5 as open symbols. As one can see, they agree well with the results obtained for the predamaging with 600 keV Ge. This means that the annealing depends on the defect concentration but not on the ion species used for predamaging.

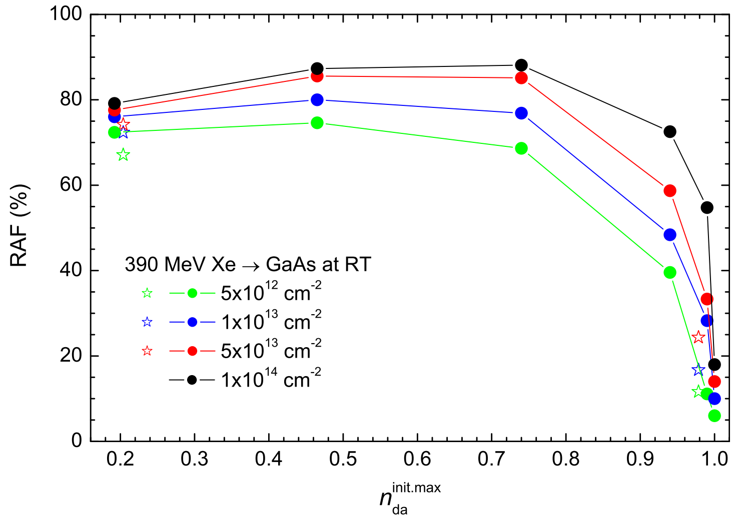

Fig. 4.5: Damage annealing in GaAs. Relative annealed fraction (RAF) of defect concentration in predamaged GaAs as a function of $n_{da}^{init.max}$ for various fluences of 390 MeV Xe [15]. The predamaging was performed either with 600 keV Se or 600 keV Ge ions (open and closed symbols, respectively). The lines connecting the data points are to guide the eye.

ing efficiency is much higher for low pre-damage levels than for those which are close to complete amorphisation. Further, the rate of defect formation due to the Xe ions themselves can increase at high pre-damage levels, which leads to a reduction in the RAF. Consequently, the defect concentrations measured after the Xe irradiation are the result of a complex interplay between generation and annealing of defects. With increasing Xe ion fluence the RAF increases for all pre-damage levels. This suggests that *defect annealing in GaAs dominates defect generation*.

TEM investigations provide additional important data on the defect structure within as-implanted and post-irradiated layers. Fig. 4.7 shows XTEM images of a Se-implanted GaAs sample with a pre-damage concentration of $n_{da}^{init.max} = 0.97$ before and after 390 MeV Xe irradiation [parts (a) and (b) of the figure, respectively]. The figure illustrates that in the

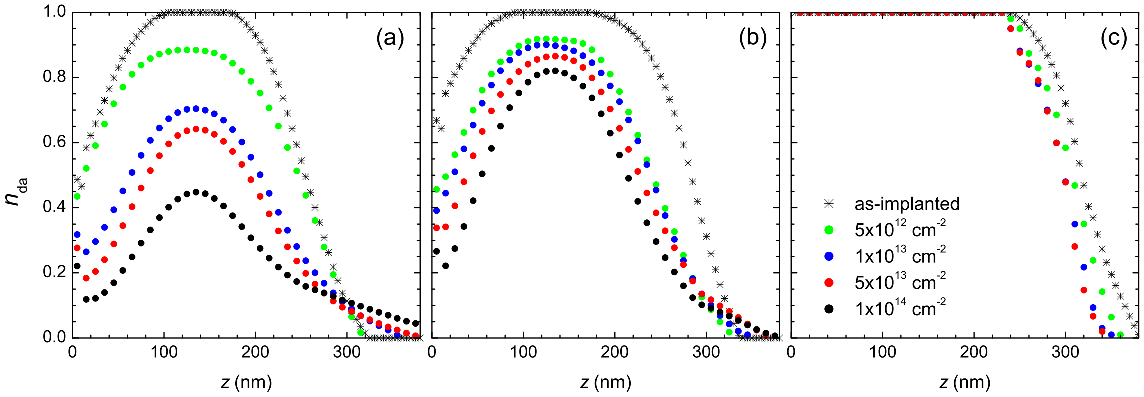

Fig. 4.6: Irradiation of differently predamaged GaAs. Damage annealing efficiency in GaAs for different predamage conditions. GaAs was predamaged with (a) 600 keV Ge (2x10^{13} cm^{-2}), (b) 600 keV Ge (2.5x10^{13} cm^{-2}), or (c) 600 keV Se (1x10^{14} cm^{-2}), and afterwards irradiated with 390 MeV Xe at RT. The description of the curves given in part (c) is valid for other parts as well.

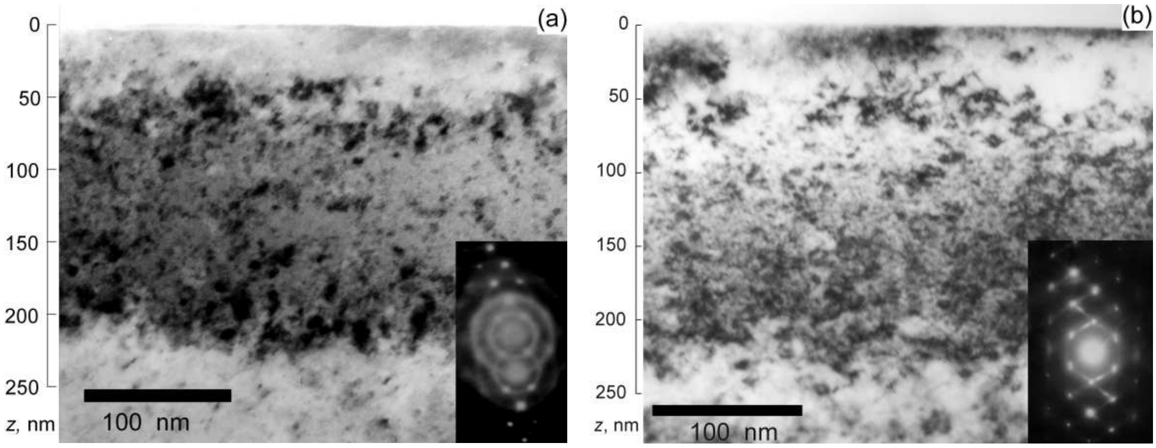

Fig. 4.7: Irradiation of predamaged GaAs with 390 MeV Xe at RT. Bright-field XTEM images of a GaAs sample first implanted with 2x10^{13} cm^{-2} Se at LNT and then irradiated with 1x10^{13} cm^{-2} Xe at RT [15]: (a) as-implanted, (b) after the Xe post-irradiation.

as-implanted GaAs sample the depth interval from ≈ 50 nm to ≈ 220 nm mainly consists of amorphous material (dominating grey homogeneous "background" without contrast as well as diffuse rings from the amorphous phase in the corresponding diffraction pattern) with some crystalline inclusions (dark contrast spots correspond to crystalline material but misaligned with the original crystalline matrix). The Xe irradiation [see Fig. 4.7(b)] decreases the amount of damage considerably; particularly, the diffraction pattern shows no indication of amorphous GaAs, which means that the amorphous material is almost recrystallised. A more detailed analysis (see Fig. 4.8) showed further that the recrystallisation is imperfect and results in formation of micro-twins of different size and shape as well as dense twin lamellae and stacking faults at different depths.

Thus, the fact that at high predamage levels the annealing efficiency of SHI noticeably decreases can be better understood by the XTEM results mentioned above. Obviously, the SHI post-irradiation causes a growth of the existing crystalline inclusions that are embedded in amorphous surrounding and aligned with the original crystalline matrix. For low predamage levels there are hardly any large misaligned areas in the crystal (rather single point defects and point defect clusters), therefore, one observes an almost perfect lattice structure after SHI post-irradiation with a sufficient fluence. For higher predamage levels

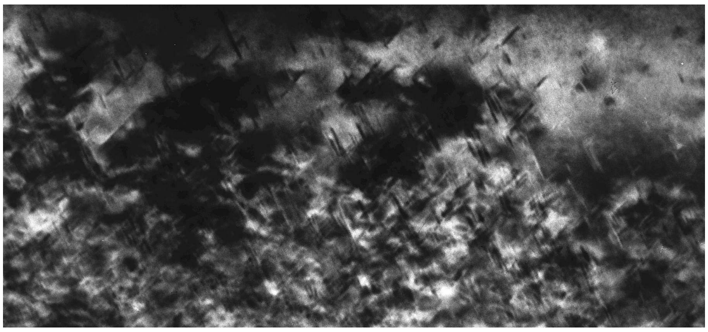

Fig. 4.8: Imperfect recrystallisation of GaAs. High-magnification XTEM image of the GaAs sample first implanted with 2x10^{13} cm^{-2} Se at LNT and then irradiated with 1x10^{13} cm^{-2} Xe at RT. One can see micro-twins of different size and shape as well as dense twin lamellae and stacking faults in the figure.

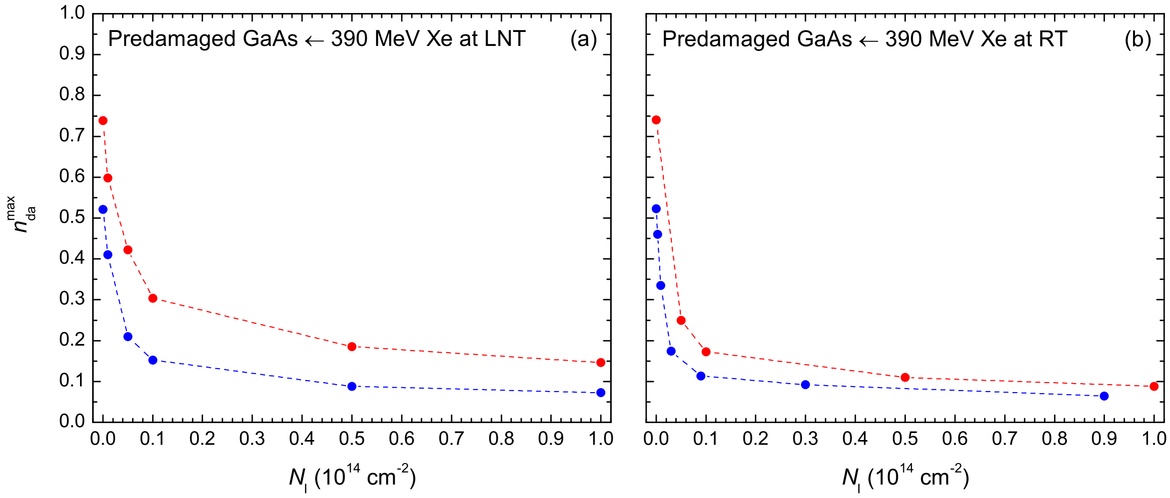

Fig. 4.9: Efficiency of damage annealing in GaAs by 390 MeV Xe at LNT and RT. Fluence dependence of n_{da}^{max} for GaAs predamaged with Ge (see Table 3.2) and post-irradiated with 390 MeV Xe. Parts (a) and (b) of the figure represent the data for LNT- and RT-irradiation with Xe, respectively. The dashed lines connecting the data points are drawn merely to guide the eye.

both the fraction of amorphous material and the ratio of misaligned/aligned crystalline inclusions increase, and this results in a less perfect lattice structure than that for low predamage levels (see Fig. 4.8).

Further, in order to check how the irradiation temperature influences the efficiency of the damage annealing by SHI's, we prepared two sets of predamaged GaAs samples with two different predamage levels $n_{da}^{init.max}$ of 52% and 74%. Those two sets of samples were irradiated with 390 MeV Xe at LNT or RT. The results obtained are presented in Fig. 4.9. One can see in the figure, that the existing damage is efficiently annealed by the Xe irradiation both at LNT and RT. Thus, the observed effect is qualitatively similar in both cases. However, the initial stage of the annealing differs noticeably for LNT- and RT-irradiation. That is, for low Xe fluences the dashed lines connecting the corresponding data points for RT-irradiation demonstrate steeper slopes than that for LNT-irradiation [compare parts (a) and (b) of Fig. 4.9]. For example, in the case of GaAs with initial damage concentration $n_{da}^{init.max} = 0.74$, the irradiation with 5x10^{12} cm^{-2} of 390 MeV Xe decreases the concentration of damage down to 0.42 and 0.25 at LNT and RT, respectively (see Fig. 4.9). Therefore, predamaged GaAs is annealed by SHI's more efficiently at RT than at LNT.

It is useful to compare the annealing efficiency for different SHI irradiation conditions. For this purpose we have selected the experimental data on the radiation damage annealing by 140 MeV Kr, 390 MeV Xe and 593 MeV Au in predamaged GaAs samples having similar values of the initial damage concentration of about 50-60%. Fig. 4.10 depicts the relative defect concentration n_{da}^{max} either versus the ion fluence N_I or versus the deposited electronic energy density $\varepsilon_e \cdot N_I$ [see parts (a) and (b), respectively]. Obviously, the annealing efficiency increases in the sequence Kr – Xe – Au, i.e., it is higher for ion beams having higher electronic energy loss ε_e [see Fig. 4.10(a) and Table 3.3]. Further, the relative differ-

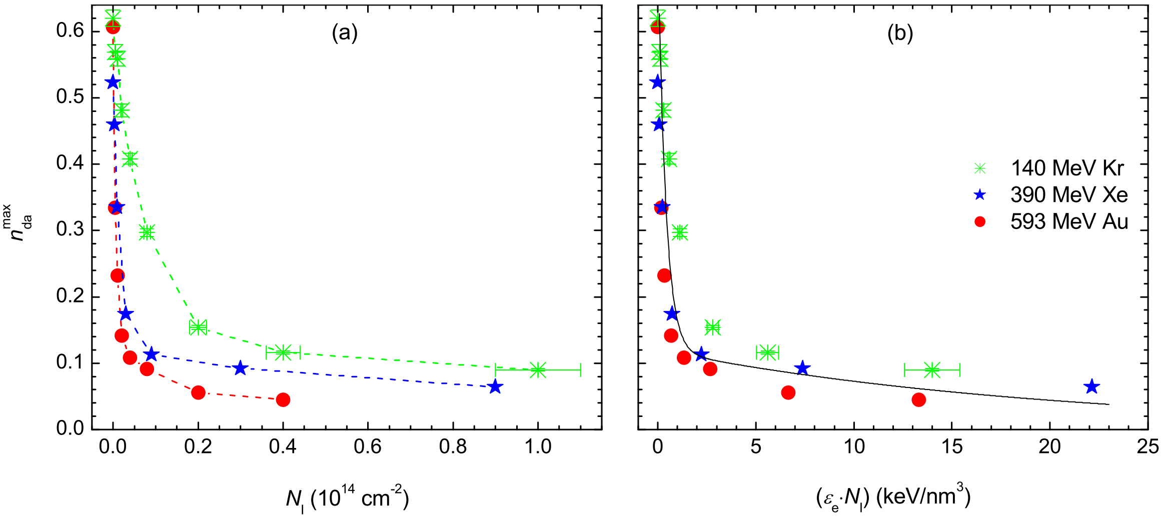

Fig. 4.10: Efficiency of damage annealing by different SHI's. Dependence of n_{da}^{max} on (a) ion fluence N_I, and (b) deposited energy density $(\varepsilon_e \cdot N_I)$ for GaAs predamaged with Ge (see Table 3.2) and post-irradiated with 140 MeV Kr, 390 MeV Xe, or 593 MeV Au at RT. The dashed lines connecting the data points are drawn merely to guide the eye.

ence between the values of ε_e for Xe and Au (24.6 keV/nm and 33.3 keV/nm, respectively) is smaller than that between the values of ε_e for Kr (14.0 keV/nm) and Xe, and for Kr and Au. This is in agreement with the fact that the respective $n_{da}^{max}(N_I)$ data points for 140 MeV Kr are definitely not on the same line with those for Xe and Au even taking into account the experimental uncertaincy [see Fig. 4.10(a)]. To check whether the experimental data for these three different ion species can be described by the *total density of the deposited electronic energy*[3], we multiplied the values of N_I by the respective values of ε_e characteristic to each certain ion species (see Table 3.3), i.e, we plotted the same data as a function of $(\varepsilon_e \cdot N_I)$. After this step all the data points within $0.2 < n_{da}^{max} < 0.6$ range can be well fitted by a single exponential curve [see Fig. 4.10(b)]. That means that SHI-induced annealing in predamaged GaAs is *widely determined* by the *integral electronic energy density* introduced into the material by SHI's.[4]

---

[3] This quantity is secondary and complementary to the electronic energy loss ε_e of a single ion in certain target.

[4] A similar observation was reported by Wesch *et al.* for GaAs implanted at RT with various ion species within 0.2 MeV – 10 MeV energy range [5].

4.3 Damage formation in virgin InP

As it will be shown below, virgin single-crystalline InP appears to be much less radiation-resistant to SHI irradiation than virgin Ge and GaAs (see Sect. 4.1). Therefore, InP is considered in this section separately from the other two materials.

4.3.1 Depth distribution of radiation damage

As an example, Fig. 4.11 illustrates the radiation damage build-up in InP bombarded with 390 MeV Xe at RT. Part (a) of the figure represents RBS spectra, and part (b) shows the corresponding depth distributions of the relative damage concentration n_{da}.

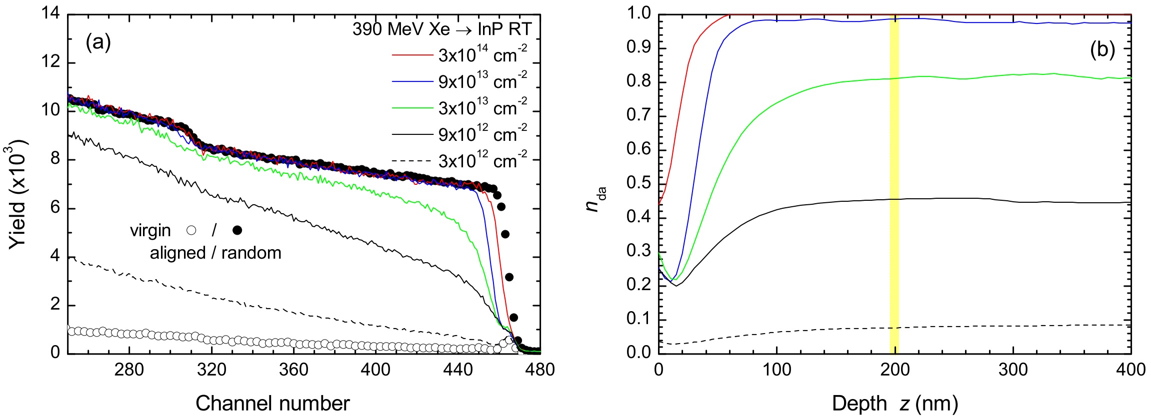

Fig. 4.11: Irradiation of virgin InP with 390 MeV Xe at RT. (a) RBS spectra of virgin InP irradiated with different fluences of 390 MeV Xe at RT, and (b) the corresponding depth distribution of the radiation damage concentration n_{da} [18].

One can see in Fig. 4.11(a) that the ongoing Xe irradiation at RT leads to defect formation and accumulation in InP. Finally, at sufficiently high ion fluences the material is rendered heavily damaged (amorphised). Further, as it can be seen from Fig. 4.11(b), in depths behind an only slightly damaged surface layer (ca. 40 nm thick) the damage concentration remains almost constant, which is in accordance with the depth distribution of the electronic energy deposition (see Fig. 3.3).

4.3.2 Charge state effect on near-surface damage formation

As it was shown in Sect. 4.3.1, irradiation of single-crystalline InP with large fluences of SHI's can cause formation of amorphous layers within the depth range of dominating electronic energy loss. However, contrary to the bulk, a thin surface layer (tens of nanometres) remains almost undamaged as proven by three independent experimental methods (TEM, XRD and RBS) [9, 10, 16, 18, 19, 66, 67]. This is well illustrated in Fig. 4.12 showing a XTEM image of InP irradiated with 250 MeV Xe at RT. One can see an approximately 30-35 nm thick crystalline surface layer (CSL) containing only few small clusters of defects,

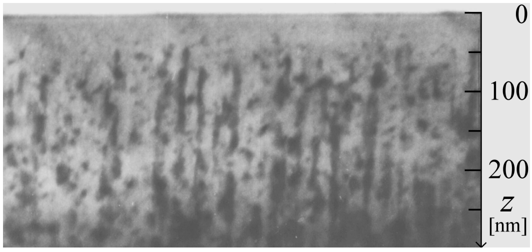

Fig. 4.12: Thin crystalline surface layer. Bright-field XTEM image of InP irradiated at RT with 250 MeV Xe (7x10^{12} cm^{-2}) [9].

but not heavy damage/tracks that are observed deeper. Two plausible suppositions can be made in order to explain the existence of the thin CSL: (a) either the surface acts as an efficient sink for defects produced by SHI irradiation near the surface (i.e., they move towards the surface and annihilate there), or (b) the SHI energy loss in the first tens of nm is lower than that in the bulk.

Fig. 4.13 shows $\Delta\chi_{min}(z)$ dependences for 250- or 390-MeV Xe, and 593-MeV Au irradiation of InP. With increasing SHI fluence, $\Delta\chi_{min}(z)$ increases up to its maximum value, which is commonly taken as an indication for amorphisation. However, in all cases a thin surface layer appears to be only slightly damaged for low and medium SHI fluences.

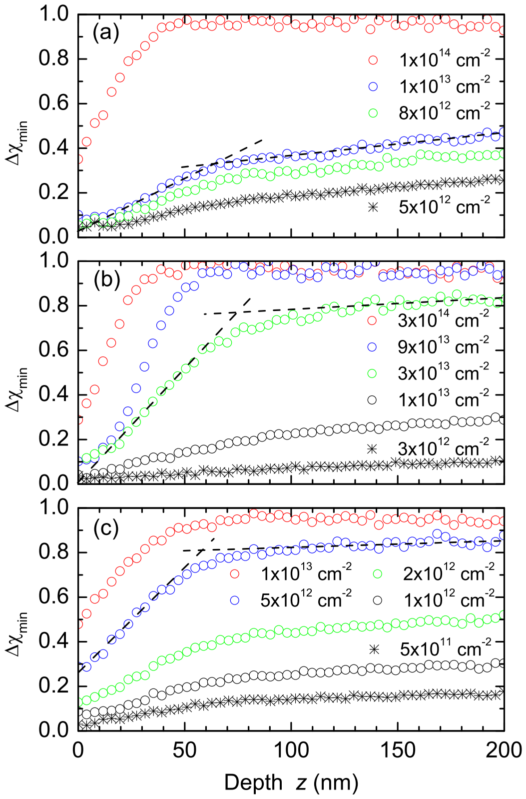

Fig. 4.13: Depth distribution of $\Delta\chi_{min}$. Difference in minimum yield vs. depth for different fluences of (a) 250 MeV Xe, (b) 390 MeV Xe, and (c) 593 MeV Au irradiation at RT. The dashed auxiliary lines are used to estimate the CSL thickness that is taken to be one-half of the depth at which the two respective lines intersect.

Further, there is an indication that the damage accumulation within a ca. 20 nm thick surface layer proceeds differently for 250 MeV Xe and 390 MeV Xe, on the one hand, and for 593 MeV Au, on the other hand. For example, in the case of 390 MeV Xe [see Fig. 4.13(b)] there is no noticeable increase in damage concentration within $0 \leq z \leq 20$ nm interval for two different ion fluences of 3x10^{13} and 9x10^{13} cm^{-2}, though at the same time $\Delta\chi_{min}(z)$ increases with fluence in the bulk. Only for $N_I >$ 9x10^{13} cm^{-2} (where the bulk is very heavily damaged or even amorphised already) $\Delta\chi_{min}(z)$ increases also within the thin surface layer. Contrary, in the case of 593 MeV Au irradiation the relative damage concentration increases with fluence in a similar way for both the thin surface layer and the bulk [see Fig. 4.13(c)]. Thus, the amorphisation of the thin surface layer in InP during 593 MeV Au irradiation can be explained by efficient accumulation of radiation damage

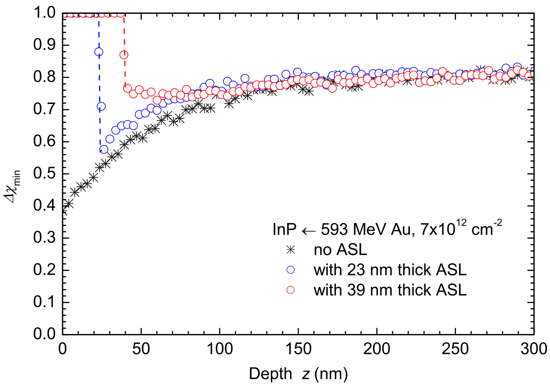

Fig. 4.14: SHI irradiation of InP with/without an amorphous surface layer (ASL). $\Delta\chi_{min}$ vs. depth for InP without or with 23/39 nm thick ASL, after 593 MeV Au irradiation [19].

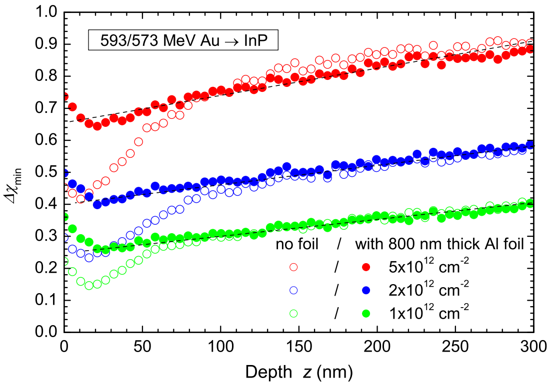

Fig. 4.15: SHI irradiation of InP through a thin Al foil. $\Delta\chi_{min}$ vs. depth for InP irradiated with either 593 MeV Au^{30+} ions or the same beam but passed through a 0.8 μm thick Al foil [20].

within this layer. In contrast, in the case of 250 MeV and 390 MeV Xe the amorphisation of the surface layers seems to be essentially governed by a broadening of the amorphous layer from the bulk towards the surface, but not due to the accumulation of radiation damage within the CSL.

In order to estimate the thickness of CSL's for different SHI irradiations, we plotted pairs of auxiliary lines together with the $\Delta\chi_{min}$ distributions for 250 MeV Xe, 390 MeV Xe and 593 MeV Au shown in Fig. 4.13. The first line in such a pair is drawn through the data points within the CSL and the second one is drawn through the data points for deeper layers, i.e., for $z \geq 100$ nm. The position of the CSL/bulk interface was estimated as one-half of the depth at which the two respective auxiliary lines intersect[5]. The estimated thickness of the CSL for 250/390 MeV Xe irradiation amounts to (35±2) nm and (37±2) nm, respectively [see Figs. 4.13(a) and (b)]. The obtained values for 250 MeV and 390 MeV Xe irradiations are very close to each other; further, the thickness of (35±2) nm for 250 MeV Xe agrees well with that observed by XTEM (see Fig. 4.12). For 593 MeV Au irradiation the thickness of the surface layer that remains partly crystalline is about (31±2) nm [see Fig. 4.13(c)].

Further, to check to which extent the surface of InP can act as a sink for defects produced within the surface layers, we performed 593 MeV Au irradiation of InP with 23 nm or 39 nm thick amorphous surface layer (ASL). Thus, the ASL is respectively thinner or thicker than the corresponding CSL mentioned above [i.e., (31±2) nm]. The resulting $\Delta\chi_{min}(z)$ dependences are shown in Fig. 4.14. One can see that for the sample with 39 nm thick ASL, $\Delta\chi_{min}(z)$ is almost constant for $z > 39$ nm, which proves that the ASL/bulk interface does not act as an efficient sink for defects. Contrary, in the case of the 23 nm thick ASL, $\Delta\chi_{min}$ in-

---

[5] Only one pair of such auxiliary lines is depicted in each case in order to avoid overcrowding. However, it is worth mentioning that for each case the average value of the interface position was determined from three different $\Delta\chi_{min}(z)$ distributions for medium fluences (where the bulk is not yet amorphised); the data for the highest fluences used were omitted in order to exclude a possible effect of the broadening of the amorphous layer from the bulk.

creases with depth for $z \geq 23$ nm in a similar manner as it does for InP without ASL (see Fig. 4.14). This demonstrates that a thin depth layer at $z \geq 23$ nm is much less damaged than the bulk. So as neither the surface nor the ASL/bulk interface can account for the existence of the slightly damaged layer at $z \geq 23$ nm for the sample with 23 nm thick ASL, it should be ascribed to a non-uniform depth distribution of defects being formed by SHI's. More specifically, the last indicates that ε_e must increase with depth within the range of interest (i.e., for approximately $0 \leq z \leq 50$ nm) in a similar manner as $\Delta\chi_{min}(z)$ does. The results obtained for other ion fluences (not shown) enabled the same conclusions.

Because the electronic energy loss of the ions depends on their momentary charge state q, the reduced defect concentration close to the surface can result from processes of single or multiple electron loss for SHI's travelling in the surface layers of solids [68]. To verify whether a difference between q_{init} and q_{mean} can be of importance for the CSL's observed experimentally, we performed irradiation of single-crystalline InP with 593 MeV Au^{30+} ions passed through a thin (0.8 μm) Al foil. In this way the ion beam energy is lowered by 20 MeV and, simultaneously, the charge of the ions is increased up to its equilibrium value, specific for the Al bulk (see Table 3.4). So as the projectile charge is only very weakly dependent on the properties of the solid target [69], the charge of 573 MeV Au ions just before entering InP is expected to be very close to the equilibrium one in bulk InP. Figure 4.15 shows depth distributions of damage formed by a direct 593 MeV Au^{30+} irradiation, on the one hand, and by an irradiation after the beam passed through the 0.8 μm thick Al foil, on the other hand. We can see in the figure that the $\Delta\chi_{min}(z)$ profiles for (573 MeV Au) irradiations through the foil do not show the decrease in $\Delta\chi_{min}$ close to the surface, occurring for the direct irradiations (see also Fig. 4.13). (The small peaks at $z = 0$ are merely surface peaks that are unavoidable in aligned RBS spectra.) This experimental result clearly shows that the noticeably lower efficiency of damage formation at the surface is explained solely by the initial ion charge being lower than the equilibrium one in the bulk (see [19] for details).

In fact, the values of CSL's thickness obtained for all SHI irradiations with $q_{init} < q_{mean}$, that is for 250/390 MeV Xe and 593 MeV Au (see Table 3.4), are in qualitative agreement with the data on the target thickness necessary to attain an equilibrium charge distribution in a beam of fast ions with different initial charge states, i.e., about 20-50 nm [70, 71]. For example, this value amounts to ca. 10^{17} at/cm^2 for irradiation of gaseous Ar with 1 MeV/nucleon I ions (see Fig. 5(d) in Ref. [70]). Taking this as an estimate for InP, one obtains a value of about 25 nm that is close to the values of the CSL thickness for 593 MeV Au and 250/390 MeV Xe irradiations [(31±2) nm, (35±2) nm, and (37±2) nm, respectively]. This supports the idea that the CSL thickness corresponds to the thickness of the layer the ion has to pass through until its equilibrium charge is reached.

Figs. 4.16 and 4.17 depict the difference in minimum yield versus depth, $\Delta\chi_{min}(z)$, for the irradiation of virgin InP with decelerated Au and Xe ions passed through relatively thick (tens of μm) Al foils. In all these cases $q_{init} \approx q_{mean}$ and, consequently, $\varepsilon_e(z) \approx const$ within

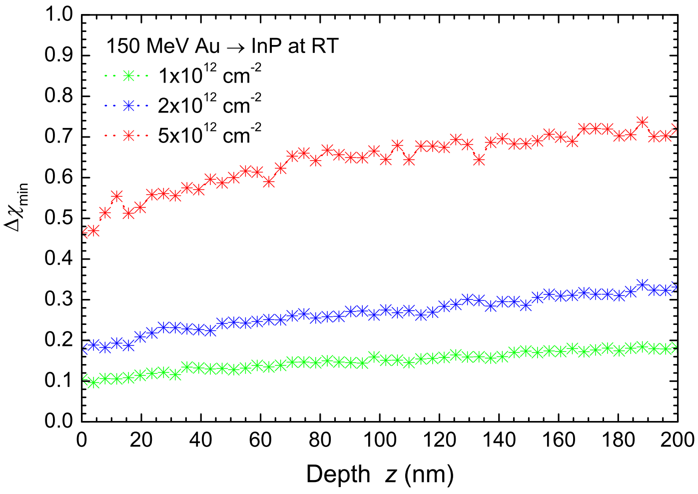

Fig. 4.16: Depth distribution of $\Delta\chi_{min}$ in InP irradiated at RT with (above-threshold) 150 MeV Au [19].

the depth interval of interest ($0 \leq z \leq 200$ nm). In the case of irradiations with 150 MeV Au [i.e., in an above-threshold regime ($\varepsilon_e > \varepsilon_e^{thr}$), see Table 3.4], no CSL is observed (Fig. 4.16). This is in agreement with the almost uniform $\varepsilon_e(z)$ distribution and gives us one more indication that the influence of the surface as a sink for defects is much less significant (if any). Furthermore, this also supports our assumption that the reduced electronic energy loss in case of $q_{init} < q_{mean}$ is responsible for the occurrence of the CSL's.

Contrary, for sub-threshold and near-threshold irradiations (64 MeV Au and 82 MeV Xe) a CSL is registered (see Fig. 4.17). Its thickness amounts to (12±2) nm for 64 MeV Au and (14±4) nm for 82 MeV Xe irradiation, i.e., it is 2-3 times smaller than that for the irradiations with 250/390 MeV Xe or 593 MeV Au (cf. with Fig. 4.13). Because we expect the ions to be in the mean equilibrium charge state, no CSL's should exist, at least not when assuming that the damage measured is caused solely by the electronic energy loss. This indicates that in the case of sub-threshold irradiations the electronic energy loss alone

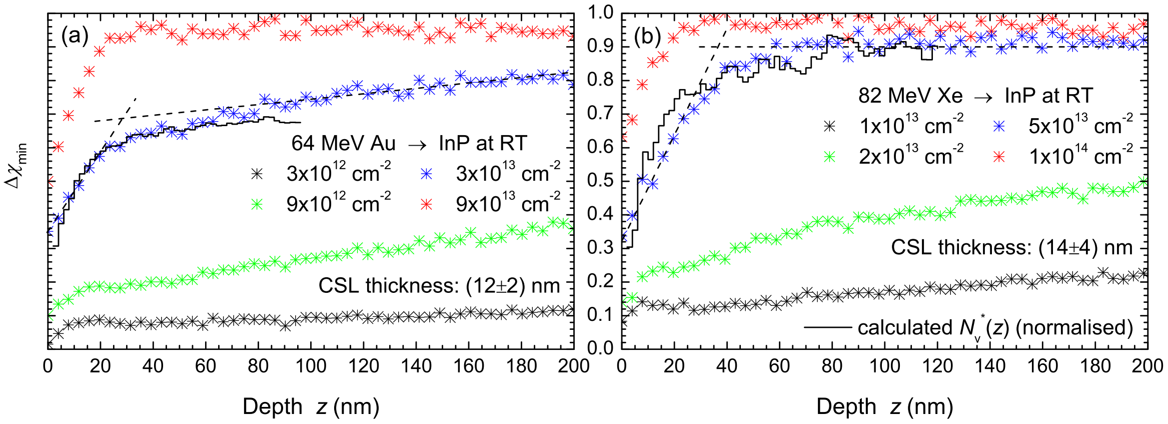

Fig. 4.17: $\Delta\chi_{min}$ versus depth for (sub-threshold) 64 MeV Au and 82 MeV irradiations. Depth distribution of $\Delta\chi_{min}$ in InP irradiated at RT with (a) 64 MeV Au or (b) 82 MeV Xe [19]. The dashed auxiliary lines are used to estimate the thickness of CSL's that is taken to be one-half of the depth at which the two respective lines intersect. The solid stepped curves represent the corresponding normalised distributions of displacements, $N_v^*(z)$, calculated with the SRIM-2003 code (in arb. units).

cannot be responsible for the damage formation and that the observed depth distribution of defects is at least to a large part due to the nuclear energy loss. Really, the deceleration of SHI's by using the Al foils inevitably leads to a higher nuclear energy loss ε_n (see Table 3.4) that can also contribute to the damage formation. Furthermore, the damage production due to the nuclear energy loss can become the principal mechanism for sub-threshold and near-threshold irradiations (if $\varepsilon_e \leq \varepsilon_e^{thr}$, i.e., when the electronic energy loss is too low to form heavy damage/tracks). From earlier studies on ion implantation in InP it is known that for $N_v \approx 10$ nm^{-1} amorphisation is reached for $n_{dpa} \approx 0.4$ dpa and for $N_v < 3$ nm^{-1} amorphisation seems to be hardly possible due to the nuclear energy loss [72]. Taking into account the fluences applied (see Table 3.4), a possible influence of the nuclear energy deposition is to be expected only for 64 MeV Au and 82 MeV Xe. E.g., in the case of the highest fluence of 64 MeV Au (9x10^{13} cm^{-2}) the material is close to amorphisation or already amorphised [see Fig. 4.17(a)]. In this case we have $N_v = 15.2$ nm^{-1} (see Table 3.4) and the resulting value of n_{dpa} amounts to approx. 0.35 dpa that is in good agreement with the value of 0.4 dpa mentioned above. Therefore, in this particular case the radiation damage accumulation can be explained by the nuclear energy deposition processes. This conclusion is also supported by the depth dependence of the vacancy concentration $N_v(z)$ calculated with the SRIM-2003 code. The corresponding normalised depth distributions, $N_v^*(z)$, for 64 MeV Au and 82 MeV Xe irradiation are plotted as solid lines in both parts of Fig. 4.17. In both cases the corresponding $N_v^*(z)$ profiles are in agreement with the measured damage distributions $\Delta\chi_{min}(z)$. Contrary, in the case of 150 MeV Au irradiation, $n_{dpa} = 0.009$ dpa is obtained for the highest fluence used. The radiation damage that is to be expected for this value of n_{dpa} is much lower than the measured value of $\Delta\chi_{min} \geq 0.5$ (see Fig. 4.16), and thus for 150 MeV Au irradiation ε_e, but not ε_n is responsible for the observed radiation damage.

To summarise, no any noticeable influence of the surface as a sink for defects was found. Therefore, the existence of the observed CSL's in *above-threshold regimes*[6] should be ascribed to an increasing value of ε_e with depth due to the increasing charge of the projectiles within the first tens of nm [19, 20]. Contrary, in sub-threshold regimes the less efficient damaging near the surface is due to the nuclear energy loss [19] that forms less defects at the surface than in the bulk (see Fig. 4.17). Generally, in an above-threshold regime the radiation damage production is determined by the electronic energy deposition, while in the sub-threshold regime the observed damage accumulation is at least to a large part due to the nuclear energy loss.

---

[6] Here "above-threshold" and "sub-threshold" is mentioned with regard to the electronic energy loss ε_e being respectively higher or lower than the threshold value ε_e^{thr} necessary for track formation.

4.3.3 Role of various experimental conditions

The following section shows how the efficiency of the damage formation and accumulation in InP is influenced by various experimental conditions (ion species, ion energy E, the electronic energy loss ε_e, and irradiation temperature). For the sake of accuracy one needs to fix as many parameters of interest as possible. The best case would be to fix all but one parameter. Unfortunately, the last is impossible in practice because they are not independent of each other. Nevertheless, a respective analysis yields some important conclusions, as it will be shown below.

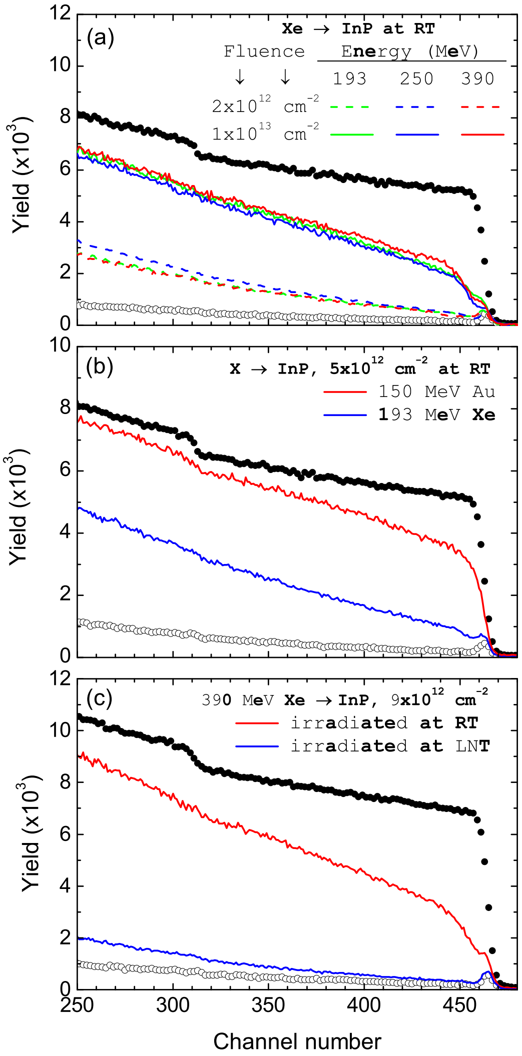

Fig. 4.18: RBS yields for various experimental conditions. RBS yields measured in InP samples for different irradiations. The open and closed symbols in all parts of the figure stand for the RBS yield measured in a virgin InP sample in axially aligned and random directions, respectively.

Fig. 4.18(a) shows RBS yields for two different fluences of 193 MeV, 250 MeV and 390 MeV Xe irradiations at RT. One can see that the aligned RBS spectra for these three different energies are close to each other for both ion fluences of 2x10^{12} cm^{-2} and 1x10^{13} cm^{-2}. This observation conforms to close values of the electronic energy loss per ion and unit path length ε_e [18.6 keV/nm, 20.0 keV/nm and 21.5 keV/nm for 193 MeV, 250 MeV and 390 MeV Xe irradiations, respectively (see Table 3.4)]. However, ε_e is not the only quantity that gov-

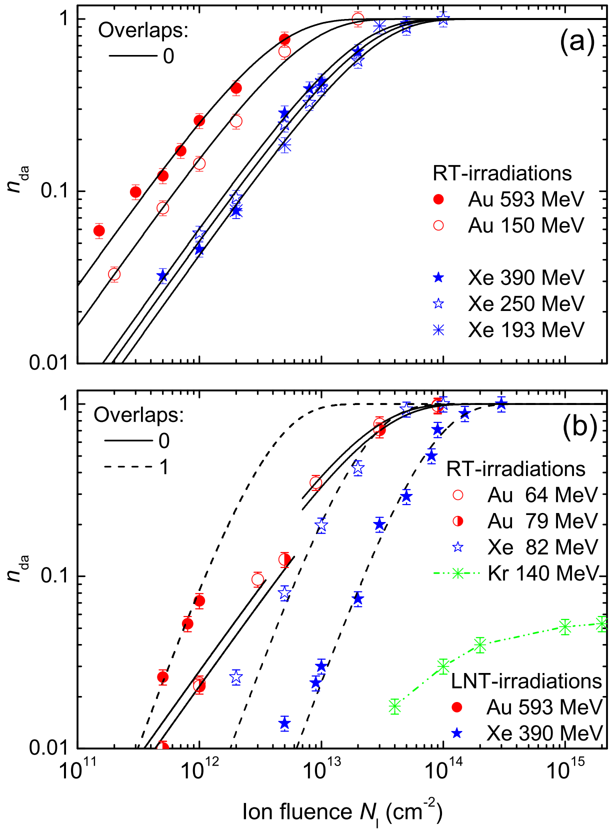

Fig. 4.19: Radiation damage *vs.* ion fluence. Relative concentration of displaced lattice atoms versus the ion fluence for different ion species listed in Table 3.4. Parts (a) and (b) cover all above-threshold and sub-threshold irradiations, respectively [20]. The relative error of the ion fluence is about 10% and, consequently, is well represented by the data point sizes. The dash-dot-dot line connecting the data points for 140 MeV Kr in (b) is only to guide the eye. Solid and dashed lines in both parts stand for fitting curves obtained by using Gibbons' overlap damage model assuming zero- or first order of overlapping, respectively.

erns the formation of radiation damage in InP. This is illustrated by Fig. 4.18(b), where selected RBS spectra for 150 MeV Au and 193 MeV Xe irradiation are shown. In this case the RT-irradiation with 193 MeV Xe forms noticeably less damage than that with 150 MeV Au despite very close values of ε_e (18.6 keV/nm and 18.8 keV/nm, respectively) and q_{mean} (29.4 and 31.3, respectively) presented in Table 3.4. Further, in the case of irradiations at LNT the efficiency of damaging is remarkably reduced as compared with that at RT [18], as it is demonstrated in Fig. 4.18(c) for the case of 390 MeV Xe irradiation.

Figure 4.19 summarises the corresponding fluence dependence[7] of n_{da} for the ion species and experimental conditions presented in Table 3.4. More detailed information about the process of defect formation can be obtained by analysing the ion fluence dependence of n_{da} in the framework of the overlap damage model introduced by Gibbons [73]. In this model it is assumed that amorphous material is produced either directly by a single incoming ion or by multiple overlap of damaged but not amorphised areas. The fitting of the fluence

---

[7] In order to avoid the effect of the initial charge state discussed in Sect. 4.3.2, the respective data points are taken at depth of 200 nm of the corresponding $n_{da}(z)$ distributions as illustrated, e.g., by the vertical line in Fig. 4.11(b).

dependences within this model yields the number m of overlaps necessary to amorphise the material, and the area A_I damaged by a single ion ("damage cross-section").

Obviously, for all above-threshold RT-irradiations with different ion species and beam energies the fluence dependences of n_{da} can be fitted with an overlap number $m = 0$ [see Fig. 4.19(a)]. This means that each single ion creates a heavily damaged area along its trajectory directly. Contrary, an assumption of one overlap is necessary to fit the experimental curves in the case of irradiations with 82 MeV Xe at RT and all LNT-irradiations (390 MeV Xe and 593 MeV Au), as can be seen in Fig. 4.19(b). It should be mentioned, that only three data points for LNT-irradiation of InP with 593 MeV Au are shown in Fig. 4.19(b). Unfortunately, no further points can be presented, because larger fluences of Au cause sample breaking at LNT. Nevertheless, the initial build-up of the radiation damage is well represented and is in agreement with that of 390 MeV Xe at LNT [see Fig. 4.19(b)]. 140 MeV Kr irradiation does not lead to amorphisation, and the n_{da} value at the maximum ion fluence equals ≈ 0.05, i.e., only 5% of the target atoms are displaced from their regular lattice positions. Thus, it can be concluded that in the case of Kr irradiation the electronic energy deposition is almost inefficient to create stable defect complexes in InP (either because of weak effects of the primary damage nucleation [10] or due to a very pronounced in situ damage annealing [18]). This is in correlation to the fact that the value of ε_e for 140 MeV Kr irradiation of InP (12.1 keV/nm, see Table 3.4) is below the threshold value for track formation of 13 keV/nm (see Chapter 1). Finally, the data points for 64/79 MeV Au irradiations cannot be fitted by single curves assuming any integer value of m. Nevertheless, in both cases the data points for $n_{da} \leq 0.1$ and $n_{da} > 0.1$ can be separately fitted by curves with $m = 0$, but with different damage cross-sections A_I (for $n_{da} \leq 0.1$: 2.9 nm^2 and 2.3 nm^2 for 64/79 MeV Au, respectively; and for $n_{da} > 0.1$: 4.8 nm^2 and 4.0 nm^2 for 64/79 MeV Au, respectively). The values of the damage cross-sections A_I and number of overlaps m obtained

Ion	E (MeV)	E/M_1 (MeV/u)	T_I	m	A_I (nm^2)	r_{RBS} (nm)
Xe	193	1.50	RT	0	4.3±0.4	1.2±0.1
Xe	250	1.94	RT	0	5.3±0.5	1.3±0.1
Xe	390	3.02	RT	0	6.3±0.6	1.4±0.1
Au	150	0.76	RT	0	16.7±1.7	2.3±0.1
Au	593	3.01	RT	0	28.6±2.9	3.0±0.2
Xe	82	0.64	RT	1	8.3±0.8	1.6±0.1
Xe	390	3.02	LNT	1	2.4±0.2	0.9±0.1
Au	593	3.01	LNT	1	47.6±4.8	3.9±0.2
Kr	140	1.63	RT	–	—	—
Au	64	0.32	RT	0	4.8±0.5	1.2±0.1
Au	79	0.40	RT	0	4.0±0.4	1.1±0.1

Tab. 4.1: RBS damage cross-sections in InP. Number of overlaps m, damage cross-sections A_I, and resulting radii r_{RBS} obtained from Gibbons' model [73] for different SHI irradiations of InP.

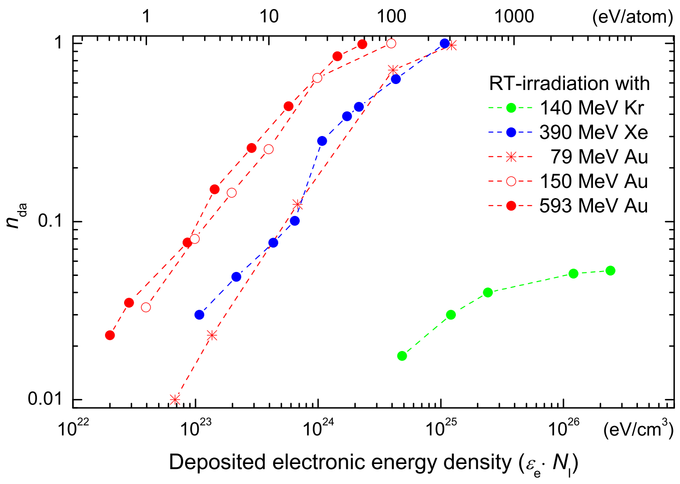

Fig. 4.20: Damage concentration versus energy density. Relative concentration of displaced lattice atoms n_{da} versus deposited electronic energy density ($\varepsilon_e \cdot N_I$) for different SHI irradiations of InP at RT. The top axis gives the independent variable in relative units of $\varepsilon_e \cdot N_I / N_a$ (here N_a is the atomic density of InP), i.e., in eV per lattice atom. The dashed lines connecting the data points are drawn to guide the eye.

by using Gibbons' model for different ion species and energies are summarised in Table 4.1. However, it should be kept in mind that those calculated damage cross-sections for all SHI species are mean values of the damage areas (produced per ion) that can be different in size (see Chapter 6).

Further, in order to obtain an additional information about possible integral effects, the values of n_{da} from Fig. 4.19 are plotted in Fig. 4.20 versus the energy density deposited into electronic processes (product of the electronic energy deposition per ion and unit path length, ε_e, and the ion fluence N_I). If the relative defect concentration remaining after irradiation would depend only on the electronic energy deposited in total per unit volume (or per lattice atom), all curves in Fig. 4.20 should fall on the same line. But this is definitely not the case, indicating that the effects observed are to a large extent *single-ion* ones. They should depend on the energy ε_e deposited per ion and unit path length. Close values of ε_e were realised first for 150 MeV Au and 390 MeV Xe and, second, for 79 MeV Au and 140 MeV Kr (see Table 3.4). However, the curves resulting for the similar values of ε_e also do not fall on the same line (see Fig. 4.20), i.e., for a given ion fluence of Au ions a higher relative defect concentration is obtained than for the Xe or Kr irradiation. All this allows to conclude that neither the energy deposition per unit path length nor the energy deposition per unit volume alone can describe the SHI effects in virgin InP [18]. Therefore, the corresponding radial distribution of the energy deposition has to be taken into account as well, which depends both on ion species (e.g., on the atomic number Z_1) and on ion energy E.

4.4 Damage annealing in predamaged InP

The effect of SHI irradiation on predamaged InP was studied for 140 MeV Kr and 390 MeV Xe irradiation. Fig. 4.21 shows the damage distributions in InP predamaged with 600 keV Ge ($1\mathrm{x}10^{13}$ cm^{-2} at LNT) and afterwards post-irradiated with different fluences of 140 MeV Kr either at RT or at LNT [parts (a) and (b), respectively]. The maximum damage concentration n_{da}^{max} of about 0.8 in the as-implanted InP is reduced down to about 0.2 due to the Kr irradiation at RT with no indication to a saturation of this effect [see Fig. 4.21(a)]. This noticeable annealing of the predamaged InP by the Kr irradiation is very similar to that previously observed in Ge and GaAs (see Sect. 4.2). Contrary, the effect of annealing is very weak in the case of LNT-irradiation. One can see in Fig. 4.21(b) that only the lowest fluence used causes slight annealing of the damage at the maximum of its depth distribution (at ca. 180 nm as indicated by the vertical dashed line in the figure), whereas higher fluences increase the damage concentration. Further, the annealing efficiency within the depth range $0 \leq z \leq 100$ nm is higher than that in the maximum, which can be probably explained by different initial concentration of damage. However, it turns out that the annealing efficiency within $0 \leq z \leq 100$ nm depth range is also higher than that within 250 nm $\leq z \leq 350$ nm depth interval despite close initial conditions. So as the surface cannot act as a sink for defects (see Sect. 4.3.2), the observed difference has to be ascribed either to the effect of the initial ion charge being lower than the equilibrium one in the bulk (see Table 3.4 and Sect. 4.3.2) or to the lower concentration of defects formed in a sub-threshold regime by the nuclear energy loss near the surface as compared with that in the bulk (see Sect. 4.3.2).

Unlike the results for 140 MeV Kr irradiation at RT, the effect of annealing is very slight in the case of 390 MeV Xe irradiation [18]. This is demonstrated in Fig. 4.22 that depicts depth distributions of the damage in an InP sample pre-damaged with 600 keV Ge up to

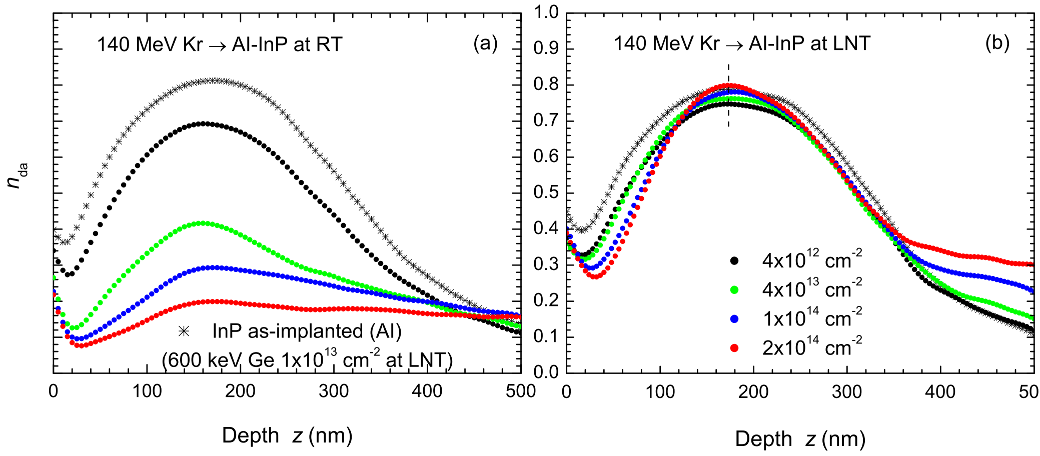

Fig. 4.21: Irradiation of predamaged InP with 140 MeV Kr. Evolution of the depth distribution of the damage concentration, $n_{da}(z)$, resulting from 140 MeV Kr irradiation of predamaged InP either (a) at RT [18] or (b) at LNT. The predamaging was performed by LNT-implantation of 600 keV Ge up to a fluence of $1\mathrm{x}10^{13}$ cm^{-2}. The description of the predamaging conditions and the values of Kr ion fluences are valid for both parts of the figure.

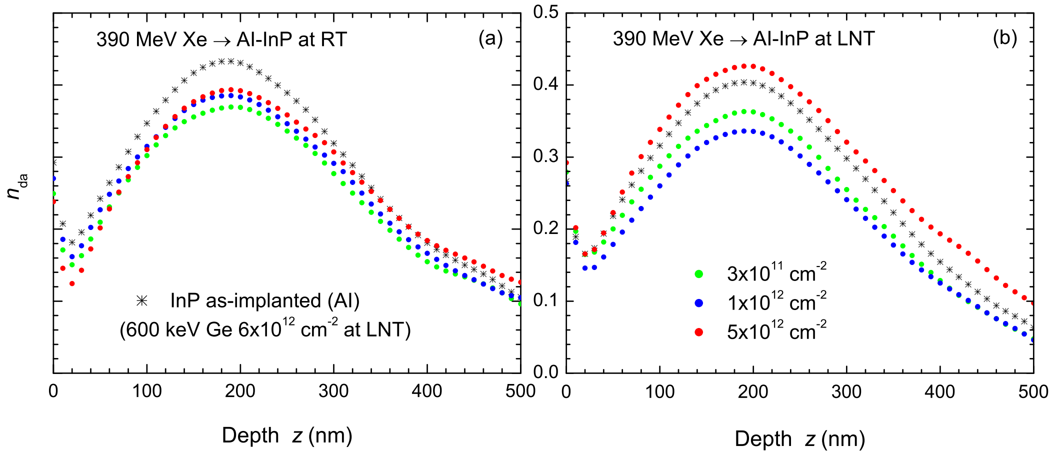

Fig. 4.22: Irradiation of predamaged InP with 390 MeV Xe. Evolution of the depth distribution of the damage concentration, $n_{da}(z)$, resulting from 390 MeV Xe irradiation of predamaged InP either (a) at RT or (b) at LNT. The predamaging was performed by LNT-implantation of 600 keV Ge up to a fluence of 6x10^{12} cm^{-2}. The description of the predamaging conditions [labelled "as-implanted (AI)" here] and the values of Xe ion fluences are valid for both parts of the figure.

6x10^{12} cm^{-2} and post-irradiated with 390 MeV Xe either at RT or at LNT [see parts (a) and (b) of the figure, respectively]. One can see that the ongoing irradiation of the predamaged InP with 390 MeV Kr at RT or at LNT results in a partial annealing only for low ion fluences, whereas higher fluences increase the damage concentration. The same conclusions are drawn for predamage levels that are lower or higher than that presented in Fig. 4.22. For example, Fig. 4.23 illustrates the effect of the 390 MeV Xe irradiation at RT on InP with two different predamage levels of about 20% and 80% [see parts (a) and (b) of the figure, respectively]. Again, only for low fluences of 390 MeV Xe a slight annealing is observed, while higher fluences lead to a larger damage concentration exceeding the initial predamage level.

Fig. 4.24 summarises the maximum relative defect concentration, n_{da}^{max}, versus the SHI fluence for different pre-damage levels. For comparison, the data points for irradiation of

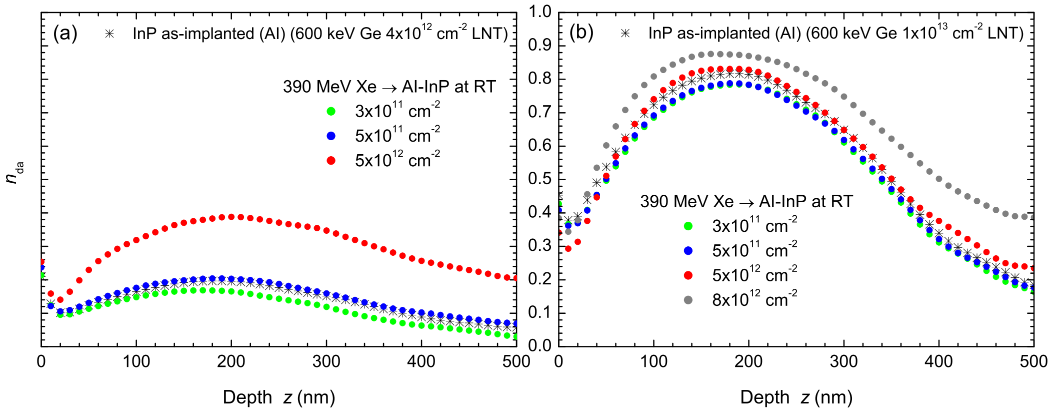

Fig. 4.23: 390 MeV Xe irradiation of InP with different predamage levels. Evolution of the depth distribution of the damage concentration, $n_{da}(z)$, resulting from 390 MeV Xe irradiation of predamaged InP at RT. The predamaging was performed by LNT-implantation of 600 keV Ge up to a fluence of (a) 4x10^{12} cm^{-2} [18] or (b) 1x10^{13} cm^{-2}.

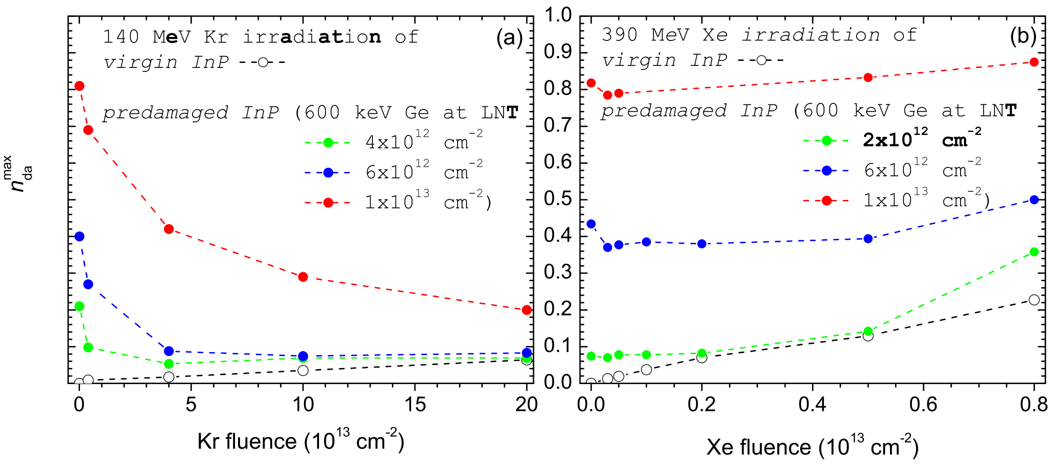

Fig. 4.24: SHI irradiation of predamaged InP under various experimental conditions. Damage concentration at the maximum of its depth distribution n_{da}^{max} [e.g., as indicated by the dashed line in Fig. 4.21(b)] versus ion fluence for (a) 140 MeV Kr or (b) 390 MeV Xe irradiation at RT [18]. The open symbols stand for the irradiation of virgin InP, and the closed ones – for the post-irradiation of predamaged InP with different initial damage concentration. The dashed lines connecting the data points are drawn to guide the eye.

virgin InP are included. As already mentioned, in the case of 140 MeV Kr [see Fig. 4.24(a)] a noticeable defect annealing takes place. However, one can see that for intermediate predamage levels ($n_{da}^{max} \approx 0.2$ or $n_{da}^{max} \approx 0.4$) over a broad range of Kr fluences the effect of the ongoing Kr irradiation is hardly visible, whereas for virgin InP one can see a slight but continuous increase of n_{da} within this fluence range. Because of the damage formation occurring during 140 MeV Kr irradiation in virgin InP and the strong annealing at low Kr fluences in the predamaged InP, the observed plateau is obviously the consequence of an equilibrium between the two concurrent processes. Fig. 4.24(b) shows that both effects are also present in the case of 390 MeV Xe irradiation. But contrary to the results for 140 MeV Kr, the annealing is relatively slight and is observed only for the lowest fluence used. For higher fluences — as in the case of virgin material — the damage formation dominates.

In summary, our results for SHI irradiation of pre-damaged InP demonstrate that both additional damage formation and annealing occur. Generally, damage formation in predamaged InP takes place for irradiation conditions that cause a strong damage formation in virgin material [18]. And annealing dominates in the case of irradiation conditions, for which only slight damaging is observed in virgin InP [18]. Most probably, this is the annealing of point defects. Furthermore, one has to consider that the ongoing irradiation results also in a defect transformation, which may be hardly visible by RBS and requires further experimental studies (e.g., TEM investigations).

4.5 TEM studies on ion track formation in InP

Transmission electron microscopy (TEM) investigations provide additional important data on the defect structure in InP bombarded with different SHI's.

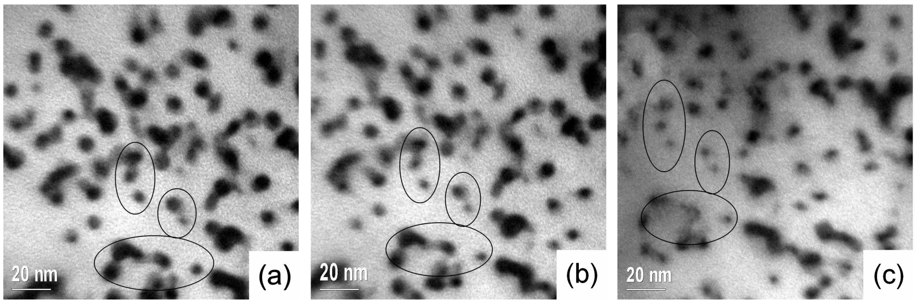

Fig. 4.25: Annealing of Au ion tracks under the electron beam. PV-TEM images of an InP sample irradiated with 593 MeV Au at RT. The series of images shows the temporal evolution of single and overlapping ion tracks under the TEM electron beam [20]. The TEM observations were performed at RT. Part (a) shows the initial picture, while (b) and (c) - after 2 and 3 minutes, respectively.

First, it is worth mentioning that various defects are efficiently annealed under irradiation with energetic electrons during TEM analysis. It turns out that ion tracks are generally not stable under the electron beam. As an example, Fig. 4.25 shows a series of plan-view (PV) TEM images of an InP sample irradiated with 593 MeV Au at RT. One can see that already after the first 3 minutes the TEM image changes very noticeably.[8] Further, the effect seems to be even more noticeable in the case of the ion tracks formed by 375 MeV Xe ions. So, as it is shown in Fig. 4.26, only a few ion tracks are still visible after 4 to 5 minutes.

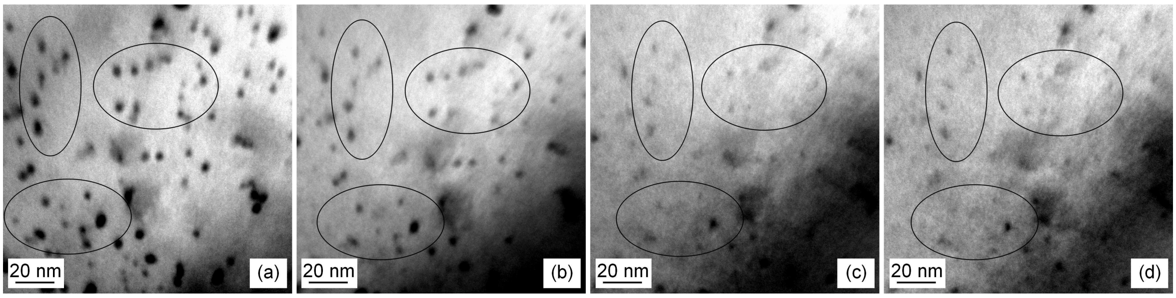

Fig. 4.26: Annealing of Xe ion tracks under the electron beam. PV-TEM images of an InP sample irradiated with 375 MeV Xe at RT. The series of images illustrates the temporal evolution of single and overlapping ion tracks under the TEM electron beam. The TEM observations were performed at RT. Part (a) shows the initial picture, while (b), (c), and (d) - after 2, 4, and 5 minutes, respectively.

The conclusions mentioned above are also supported by the evidence obtained by high-resolution (HR) TEM. Fig. 4.27 represents images taken at higher magnification than that of Figs. 4.25 and 4.26 ($\times 1\,000\,000$ vs. $\times 120\,000$). One can see that in only two minutes an isolated ion track with the initial diameter of ca. 4.5 nm shrinks to ca. 2 nm [cf. parts (a) and (b)]. Therefore, especially when interpreting HR-TEM images, particular care must be taken to ensure the correctness of the conclusions drawn. In order to obtain high (atomic) resolution images, high local densities of the electron current are necessary, which leads to a very efficient damage annealing. This makes it extremely difficult to reveal the *original inner structure* of the observed ion tracks, especially the smallest ones.

---

[8] A similar effect of recrystallisation was also reported by Jenčič *et al.* after TEM observations of amorphous zones formed by room-temperature irradiation of InP with 50 to 300 keV Xe ions [74].

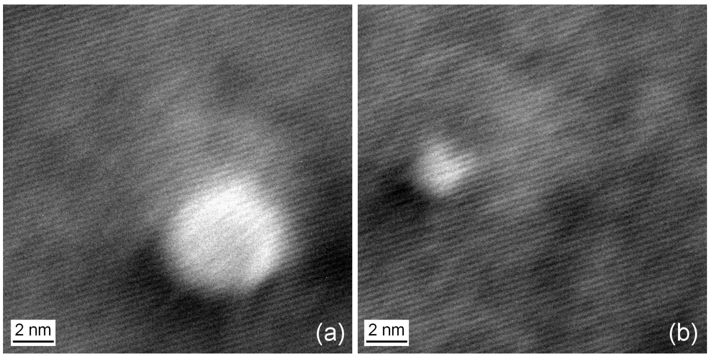

Fig. 4.27: HR-TEM analysis of ion tracks in InP. High-resolution (HR) PV-TEM images of an InP sample irradiated at RT with 573 MeV Au ions (1x10^{11} cm^{-2}). Part (a) shows the initial image, and part (b) - after 2 minutes. The TEM observations were performed at RT.

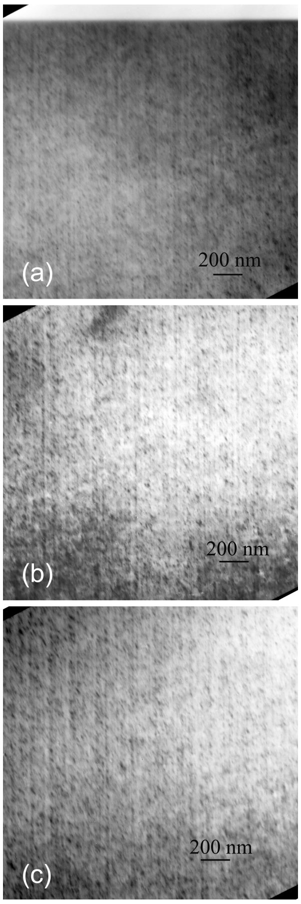

Fig. 4.28: Continuous tracks in InP. Panorama-view XTEM images of an InP sample irradiated with 593 MeV Au (1x10^{12} cm^{-2} at RT). Parts (a)-(c) are images taken at the very surface and at about 5-7 μm and 15-17 μm, respectively.

Fig. 4.28 shows cross-section (X) TEM images taken at different depths of an InP sample bombarded at room temperature with 593 MeV Au ions (1x10^{12} cm^{-2}). In all three parts of the figure one can see continuous ion tracks appearing as vertical lines with dark contrast running across the whole image areas shown.[9] This observation proves that the ion tracks extend from the surface [that is visible at the top of the part (a)] to depths z larger than 17 μm. The respective electronic energy loss at $z = 17$ μm amounts to approximately 19 keV/nm (see Fig. 3.3). Therefore, the Au ions are still in an above-threshold regime and thus are able to form tracks. However, the Au ions suffer a continuous energy loss in the target and, consequently, in deeper layers the tracks first become discontinuous and then disappear totally. This is illustrated in Fig. 4.29 that shows the depth interval where rather continuous tracks are first substituted by discontinuous ones, and then, gradually, no tracks are visible with increasing depth.

In order to estimate the number of visible ion tracks, PV-TEM images are used commonly. As an example, Fig. 4.30(a) shows a PV-TEM image of an InP sample irradiated with a relatively low fluence of 573 MeV Au ions at RT. It is worth mentioning that in this particular case the initial charge q_{init} of the ions is expected to be close to the equilibrium one q_{mean} in the bulk [i.e., at $z \approx 100$ nm and deeper, see Figs. 4.13(c), 4.14, and 4.15]. Therefore, in this

---

[9] Larger round-shaped dark spots are small In droplets located on the TEM sample surface. The droplets were formed during the ion-beam milling procedure; see also Fig. 4.33 for details.

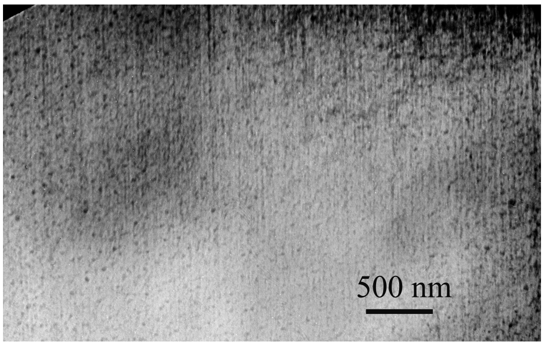

Fig. 4.29: End-of-tracks depth interval in InP. A bright-field XTEM image of an InP sample irradiated with 593 MeV Au (2x10^{12} cm^{-2} at RT). The image was taken at 25±5 μm. One can see three different depth intervals containing rather continuous tracks, discontinuous tracks and no tracks, respectively. The direction of the ion movement is from top to bottom.

case $q_{init} \approx q_{mean}$ (see Table 3.4) and, consequently, $\varepsilon_e(z) \approx const$ from the very surface of the sample. Taking further into consideration that $\varepsilon_e > \varepsilon_e^{thr}$ (see Table 3.4), one can expect that each 573 MeV Au ion produces a continuous track. In fact, the number of isolated ion tracks is $\geq$ 9x10^{10} cm^{-2} as follows from Fig. 4.30(a). Taking into account the experimental error for the estimation of the ion fluence (±10%), one can conclude that each 573 MeV Au ion produces a visible track. Further, the visible ion tracks appear to be continuous and almost uniformly thick within the sample area that is transparent to the analysing electron beam [see Fig. 4.30(b)].

Fig. 4.31 illustrates formation and accumulation of radiation damage in InP bombarded with 375 MeV Xe at RT. One can see numerous ion tracks resulting from the ongoing irradiation. The first part of the figure stands for a relatively low ion fluence, where there are not very many tracks yet and thus the overlapping is an event occurring with a relatively low probability. However, with increasing ion fluence more and more ion tracks overlap, which leads to formation of heavily damaged regions that are much larger than the initial single ion tracks (see Fig. 4.31).

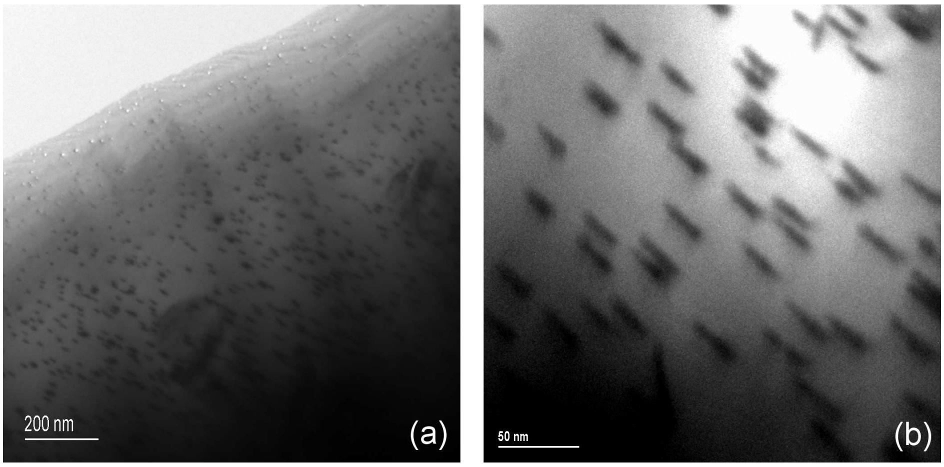

Fig. 4.30: TEM images of ion tracks in InP. Plan-view mode TEM images of an InP sample irradiated at RT with a relatively low fluence (1x10^{11} cm^{-2}) of 573 MeV Au ions (593 MeV Au ion beam passed through a 0.8 μm thick aluminium foil, see Table 3.4). Parts (a) and (b) show images of the InP sample aligned normally to the analysing electron beam (i.e, in <100> direction) and tilted, respectively.

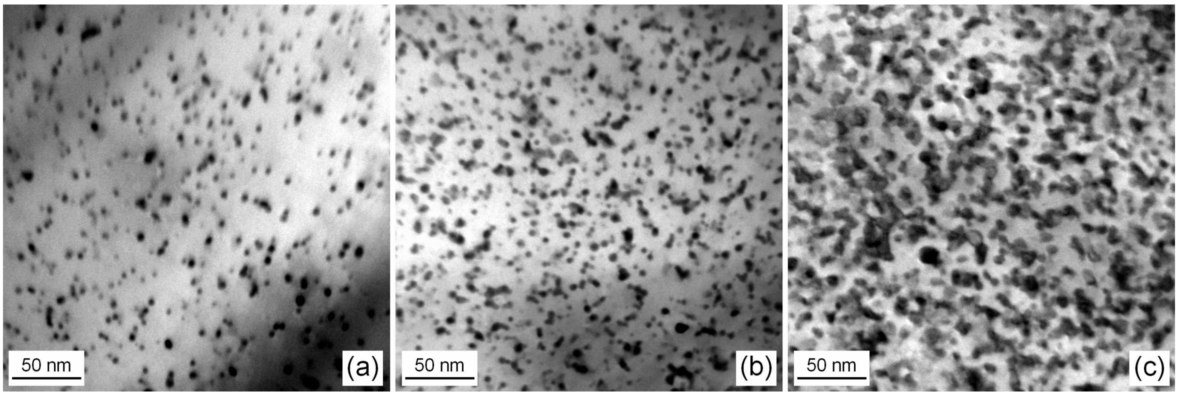

Fig. 4.31: Radiation damage accumulation with increasing ion fluence. Bright-field PV-TEM images of an InP sample irradiated with three different fluences of 375 MeV Xe at RT: (a) 8.4x10^{11} cm^{-2}, (b) 2.8x10^{12} cm^{-2}, and (c) 5.6x10^{12} cm^{-2}. The corresponding values of the relative damage concentration n_{da} for a similar irradiation with 390 MeV Xe are ca. 5%, 12%, and 30%, respectively, as it follows from Fig. 4.19(a).

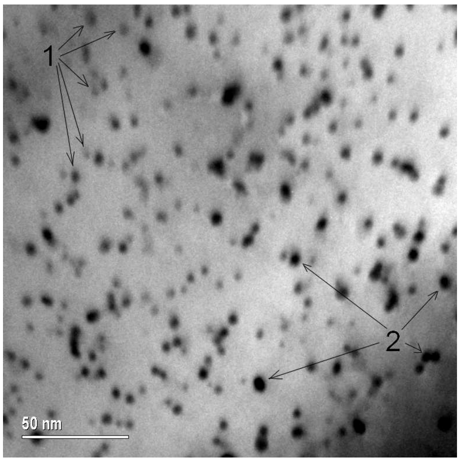

Fig. 4.32: Single and overlapping tracks. Bright-field PV-TEM image[11] of InP irradiated with 375 MeV Xe (8.4x10^{11} cm^{-2} at RT). The single isolated (narrow) and overlapping (wider) ion tracks are labelled by “1” and “2”, respectively.

It is worth mentioning that TEM investigations provide an indication that the damage accumulation in InP due to swift Xe ion bombardment proceeds in a qualitatively different way if compared with the case of swift Au ions. To illustrate this, Fig. 4.32 shows an enlarged part of Fig. 4.31(a). One can see two different types of tracks formed by 375 MeV Xe ions. The first type (labelled by “1” in the figure) represents the majority of the ion tracks. Such tracks are characterised mostly by a light-grey contrast that is sometimes even hardly distinguishable from that of the crystalline surrounding; further, their diameters do not exceed 3 nm. Most probably, such ion tracks are single-ion ones[12] and yet not completely amorphous. Contrary, ion tracks of the second type (labelled by “2”) are larger (with diameter up to 5.6 nm) and have a dark-grey to black contrast in TEM images. We believe that the larger tracks are not single-ion ones.[13] The estimated number of smaller (type “1”) and larger (type “2”) ion tracks visible in Fig. 4.32 equals 240 and 60, respectively. Such a large difference in their numbers supports the idea that the smaller tracks are primary (i.e., single-ion) ones. Keeping in mind our assumption that the larger tracks are formed by at least two ions, one can estimate the

---

[11] This image is a part of Fig. 4.31(a). The selection is made both in order to have a more homogeneous background, and to ease the counting of ion tracks (see text for details).

[12] That is, such an isolated track is formed due to a single-ion impact, and no further ions hit this local region again.

[13] I.e., such a track is formed only if a swift heavy ion penetrates one of the regions already predamaged by the preceding ions.

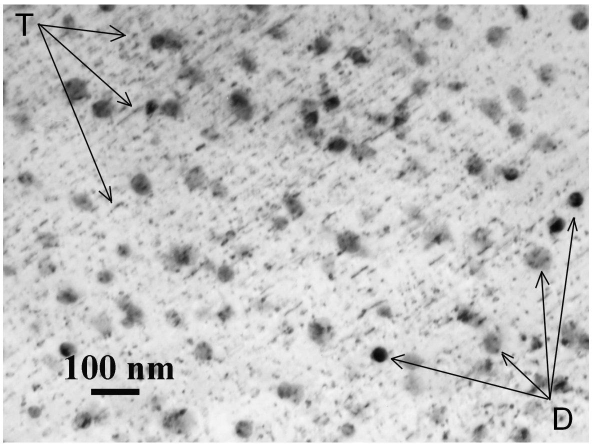

Fig. 4.33: Discontinuous tracks in InP. X-TEM image of an InP sample irradiated with 390 MeV Xe at LNT [20]. Taken at a depth of 4±1 μm. The ion fluence N_I = 3x10^{13} cm^{-2} and the corresponding value of n_{da} is 20% as it follows from the RBS measurements [see Fig. 4.19(b)]. One can see discontinuous tracks (labelled with "T") visible either as short continuous dark lines or as strings of dark points. Larger round-shaped gray or black spots with diameters of about 30–45 nm are small In droplets ("D") located on the TEM sample surface; they are formed during the ion-beam milling procedure.

total number N_{tot} of ions that impinged on the sample area shown in Fig. 4.32. Therefore, $N_{tot} \geq 360$ (i.e., $240 + 2 \times 60$), which yields 7.9x10^{11} ions/cm^2. Now the last value can be compared with the respective ion fluence N_I of 8.4x10^{11} cm^{-2} [see Fig. 4.31(a)]. The difference between them amounts to ca. 6% that is lower than the experimental uncertainty of 10% in the value of N_I.[14] Therefore, in the case of Xe ion irradiation each ion produces a track; however, the created primary (single-ion) tracks contain rather damaged but not yet amorphous material. Nevertheless, each of the subsequent projectiles might have a chance to hit one of the primary tracks. The latter event obviously enlarges the (initially small) ion tracks. Furthermore, contrary to the single-ion tracks, the larger tracks formed due to multiple Xe ions are most probably amorphous. This idea is supported, e.g., by the TEM data on the annealing of ion tracks under the analysing electron beam (see Fig. 4.26). So, the largest ion tracks with a black contrast in Fig. 4.26(a) shrink very noticeably after 4-5 minutes, but do not disappear yet. Contrary, the smaller ion tracks are hardly seen or not seen at all after the same span of time.

Fig. 4.33 shows discontinuous tracks formed by LNT-irradiations with 390 MeV Xe. In this case the ion tracks are observed as strings of dots or short (up to ca. 100 nm length) lines. It is worth mentioning that the diameters of the largest tracks are approximately equal to the diameters of the largest tracks formed at RT in InP by *relatively low fluences* of 375 MeV Xe [see Figs. 4.26, 4.31(a), and 4.32]. Nevertheless, for the RT-irradiation of InP with higher fluences of 375 MeV Xe the largest ion tracks have larger dimensions than those formed at LNT (e.g., with diameters of ca. 11 nm due to RT-irradiation with 5.6x10^{12} Xe/cm^2 versus 6 nm due to LNT-irradiation with an about 5 times larger ion fluence of 3x10^{13} Xe/cm^2 – compare Figs. 4.31(c) and 4.33, respectively). However, the observed large discontinuity of the ion tracks qualitatively explains the noticeable difference between respective $n_{da}(N_I)$

---

[14] Alternatively, the observed difference can be due to tracks created by three or more ions. E.g., in that case about 240, 40, and 20 tracks must originate from single, double, and triple ion impacts, respectively. Taking into account that the tracks resulting from double ion impacts have cross-sections that are 2-3 times larger than in the case of the single-ion tracks (see Fig. 4.32), the above-mentioned illustrative ratio of 240/40/20 does not seem to be unrealistic.

Ion	E (MeV)	N_I (cm^{-2})	T_I	X- or PV-TEM	Number of ion tracks (cm^{-2})	Track radii r_{TEM} (nm)
Xe	250	$3x10^{12}$	RT	PV	$> 1.0x10^{11}$	2.2-4.0
Xe	250	$5x10^{12}$	RT	PV	$> 1.4x10^{11}$	2.2-4.0
Xe	375	$8.4x10^{11}$	RT	PV	$> 6.6x10^{11}$	0.6-2.8
Xe	375	$2.8x10^{12}$	RT	PV	—	0.8-3.7
Xe	375	$5.6x10^{12}$	RT	PV	—	1.5-5.5
Xe	390	$3x10^{13}$	LNT	X	—	1.3-3.0
Au	150	$5x10^{11}$	RT	PV	$> 1.0x10^{11}$	2.0-3.5
Au	573	$1x10^{11}$	RT	PV	$> 9.0x10^{10}$	1.7-3.5
Au	593	$5x10^{11}$	RT	PV	$> 2.0x10^{11}$	1.5-4.5
Au	593	$7x10^{11}$	RT	PV	$> 2.5x10^{11}$	1.5-4.5
Au	593	$9x10^{11}$	RT	PV	$> 3.5x10^{11}$	1.5-4.5
Au	593	$1x10^{12}$	RT	X	—	2.0-4.5
Au	593	$2x10^{12}$	RT	X	—	2.0-4.5

Tab. 4.2: Summary of TEM results. Results of the TEM studies (cross-section or plan-view modes) of InP irradiated with various ion fluences N_I of Xe or Au ions having different energy E.

curves for RT- and LNT-irradiation of InP with Xe or Au ion beams (see Fig. 4.19).

The main results obtained by TEM studies are summarised in Table 4.2. Two important remarks concerning the data presented in the table are to be taken into consideration. First, especially for high ion fluences a multiple overlapping of the ion tracks is observed; thus we were able to estimate only the lower limit in their surface density. Nevertheless, in the case of the irradiation with a relatively low fluence of 573 MeV Au ions of $1x10^{11}$ cm^{-2} (see Fig. 4.30), ion tracks almost do not overlap and, therefore, can be counted more accurately. And second, the ion track radii determined from the PV-TEM images are exclusively for isolated tracks. However, one cannot exclude the possibility that the largest isolated tracks are due to two or more projectiles hitting the sample surface at the same point or very close to it (furthermore, such a multiple hit seems to us to be the most probable reason for the formation of the largest ion tracks). An alternative explanation of the variation in the isolated track radii is the inevitable phenomenon of ion charge fluctuations that increase or decrease the momentary energy loss and in this way statistically alter the track radii.

4.6 SIMS studies on intermixing in Bi/GaAs and Bi/InP layered structures

As it was already mentioned in Chapters 1 and 3.3.3 (see pp. 5 and 15, respectively), experiments on intermixing of layered structures are potentially capable to provide an important information on the local melting of the target matter inside SHI tracks. Therefore, we prepared

Bi/GaAs and Bi/InP layered structures[15] and irradiated them at RT with 593 MeV Au (5x10^{13} cm^{-2}). Afterwards both the unirradiated and SHI irradiated layered structures were investigated by means of secondary ion mass spectrometry (SIMS) using the geometry illustrated in Fig. 4.34. It is important to mention that in all cases the sputtering starts from the Bi layer[16] on the top of the GaAs or InP bulk, respectively (see Fig. 4.34). Fig. 4.35 shows the respective effect of intermixing in the Bi/GaAs and Bi/InP layered structures mentioned above. In the figure the SIMS yield is plotted versus the sputtering time t. One can see in the upper part of Fig. 4.35 that the irradiation of the Bi/GaAs layered structure almost do not modify the SIMS profiles for both Ga and As constituents. The slight difference between the respective profiles can be explained, e.g., by the ballistic intermixing [75–78] due to the low but not negligible value of the nuclear energy loss ε_n.

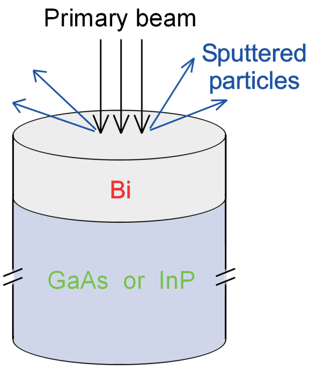

Fig. 4.34: SIMS geometry. A schematic illustration of the SIMS geometry used.

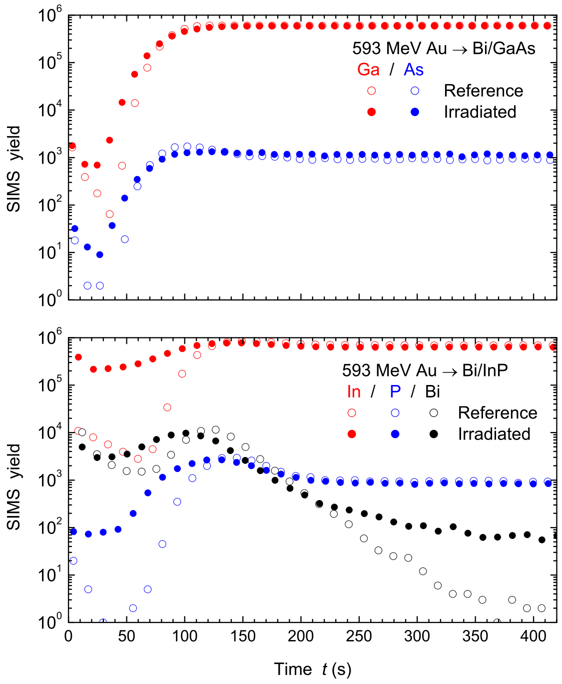

Fig. 4.35: SIMS studies on Bi/GaAs and Bi/InP intermixing. SIMS results on the intermixing in Bi/GaAs and Bi/InP layered structures due to 593 MeV Au irradiation (5x10^{13} cm^{-2} at RT). The upper and the bottom parts of the figure stand for Bi/GaAs and Bi/InP layered structures, respectively. The bottom part shows also the respective profiles of Bi for comparison. The small peaks at the surface (at $t = 0$) are inevitably caused by the transitional character of the target sputtering at the very beginning.

Contrary, in the case of the Bi/InP system the effect of the SHI irradiation is very noticeable. It is quite obvious, that In and P atoms are in large quantities transported through the

---

[15] see Sect. 3.3.3 on details of the sample preparation.

[16] The Bi layers on the top of GaAs and InP must have equal properties, particularly, their thickness equals to 62±2 nm in the both cases, as it was measured by means of RBS and surface profilometry.

Bi/InP interface towards the surface. This means that unlike the interface between Bi and GaAs, the Bi/InP interface is not so sharp after the SHI irradiation as it was before. If the observed large effect in the Bi/InP system were a result of ballistic intermixing [75–78], the same large effect must occur in the Bi/GaAs as well because the respective values of ε_n and N_v are almost identical in InP and GaAs (see Tables 3.3 and 3.4). However, this is clearly not the case, as follows from Fig. 4.35. Thus, the efficient intermixing observed in the case of the Bi/InP layered system cannot be ascribed to the action of the nuclear energy deposition ε_n and, consequently, must be governed by the the electronic energy loss ε_e. Taking further into account the observation that both sides of the interface must be locally molten by SHI's in order to make an efficient intermixing possible (see p. 5) [45–47, 49, 50], one can conclude that the observed large difference between the magnitude of the intermixing in Bi/GaAs and Bi/InP layered systems can be easily understood if assuming that in GaAs, contrary to InP, no molten tracks are formed.[17]

To sum up, the observed difference between GaAs, on the one hand, and InP, on the other hand, is in agreement with the fact that GaAs is much more resistant to SHI irradiation than InP (see Sect. 4.1 and 4.3).

---

[17] Or alternatively, they have negligible dimensions or exist too shortly to cause a noticeable transient interduffusion in the tracks across the interface Bi/GaAs.

Chapter 5

Modelling of swift heavy ion irradiation effects in InP

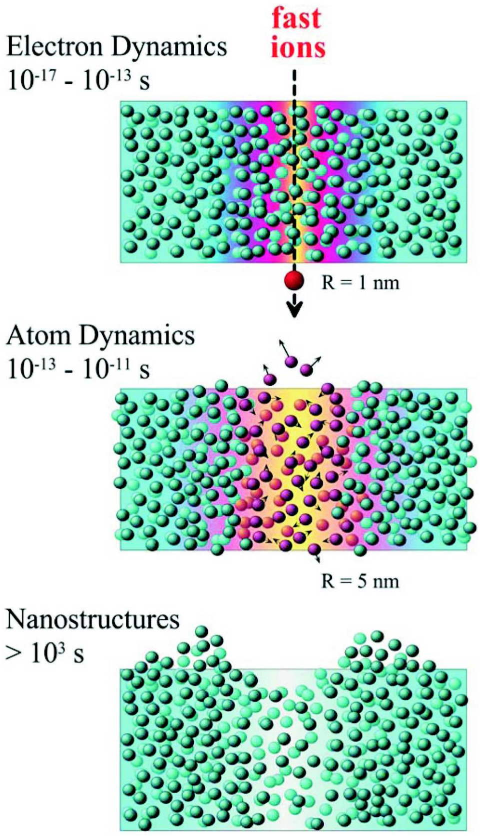

Fig. 5.1: Energy relaxation in ion track. Time-evolution of an ion track. The initial electronic excitation can finally induce an atomic motion, and in this way the resulting disorder is frozen in. Taken from Ref. [69].

This part is devoted to a theoretical description of the formation of the radiation damage (particularly, ion tracks) in InP bombarded with swift heavy ions (SHI's). The corresponding energy loss per unit path length of a SHI with atomic number Z_1, energy E and mass M_1 can be divided into two parts: nuclear (ε_n) and electronic (ε_e) energy loss. It was shown above (see Sect. 4.3) that the high electronic energy deposition in InP samples bombarded with various SHI's results in a measurable damage within the near-surface region. In order to answer the question how this high amount of the electronic excitation is transferred into atomic motion, one has to consider all temporal stages of the energy transfer from SHI's to electrons and then to the lattice.

The initial processes of the energy transfer from a SHI take only 10^{-19} to 10^{-17} s for inner-shell interactions and slightly longer (about 10^{-16} s) for collective electronic excitations (formation of plasmons) [69]. Hence, just after the passage of the SHI, the narrow cylindrical target zone coaxial with the SHI path consists of a two-component plasma of "cold" lattice atoms and "hot" electrons as it is illustrated in Fig. 5.1. Such a narrow region is often called "ionisation spike". At later temporal stages this high amount of the electronic excitation is transferred into atomic motion (see Fig. 5.1). The initial energy distribution and dynamics of the hot charge carriers within "ionisation spikes" have been extensively studied by Schiwietz *et al.* [79] by means of Auger-electron spectroscopy.

Irradiation of matter by ultrashort (fs-, ps- or ns-scale) laser pulses is one more powerful technique widely used to study the ultrafast dynamics of the excited charge carriers and the energy transfer to the lattice from the temporal evolution of the optical properties of the material [80–82]. A principal difference between plasmas formed by SHI's and by laser irradiation of solids is the energy distribution of freed electrons. Usually, laser pulses lead to an almost uniform energy distribution (i.e., loosely bound and freed electrons gain approximately equal energy defined by the laser wavelength). On the contrary, electrons located closely to the paths of the SHI's gain very different energies dependent on their binding energy and impact parameter.

5.1 Ionisation spikes

In this section the first stage of energy relaxation (i.e., ionisation spikes formed by SHI's) will be considered in more detail. In order to do so, one faces the following basic aspects: the number of electrons freed from their host atoms, their initial energy distribution, and their initial radial distribution.

The energy distribution and number of freed electrons per unit path length can be obtained from the classical Rutherford formula for delta-ray production by a single ion [83–85],

$$\frac{dn}{d\varepsilon} = \frac{\psi}{(\varepsilon + I)^2}, \tag{5.1}$$

where dn is the number of freed electrons per unit path length within the energy interval $(\varepsilon,\ \varepsilon + d\varepsilon)$ that were initially bound with energy I to the atoms. The maximum energy that can be transferred to an electron in a single collision is given by

$$\varepsilon_{max} = 2m_e\gamma^2\beta^2c^2. \tag{5.2}$$

Here m_e is the electron mass, $\gamma^2 = 1/(1-\beta^2)$, and $\beta = v/c$, where v is the ion velocity and c is the speed of light in vacuum.

Assuming an average binding energy $\bar{I}$, the total number and the total energy of the electrons freed by a single ion per unit path length are calculated from Eq. (5.1):

$$\begin{array}{l} \Delta N = \int\limits_0^{\varepsilon_{\max}} \frac{dn}{d\varepsilon} d\varepsilon = \psi \frac{1}{\bar{I}(1+k)} \\ \Delta E = \int\limits_0^{\varepsilon_{\max}} \varepsilon \frac{dn}{d\varepsilon} d\varepsilon = \psi \left[\ln\left(1 + \frac{1}{k}\right) - \frac{1}{1+k} \right] \end{array}, \tag{5.3}$$

where $k = \bar{I}/\varepsilon_{max}$. Thus, the mean value and the standard deviation of the energy per electron are given by

$$\begin{array}{l} \bar{\varepsilon} = \frac{\Delta E}{\Delta N} = \bar{I}\left[(1+k)\ln\left(1+\frac{1}{k}\right)-1\right] \\ \sigma = \sqrt{\overline{\varepsilon^2}-\bar{\varepsilon}^2} = \bar{I}\sqrt{\left(1+\frac{1}{k}\right)-\left[(1+k)\ln\left(1+\frac{1}{k}\right)\right]^2} \end{array} . \tag{5.4}$$

Using the recommended mean binding energies of 481 eV for In atoms and 172 eV for P atoms [84], the calculations yield, for the example of 150 MeV Au, $\bar{\varepsilon} \cong 450$ eV, $\sigma \cong 420$ eV, and $\bar{\varepsilon} \cong 280$ eV, $\sigma \cong 340$ eV, for the In and P sublattices of the target, respectively. Generally, the mean value of the energy per freed electron increases with increasing specific ion energy and varies from ca. 250 eV to 910 eV for the In target atoms and from 180 eV to 480 eV for the P atoms for the performed SHI irradiations. In order to analyse the basic energy distribution [Eq. (5.1)], it is useful to introduce the functions

$$\begin{array}{l} f_n(\varepsilon) = \frac{1}{\Delta N}\int\limits_0^{\varepsilon}\frac{dn}{d\varepsilon}d\varepsilon = \frac{1+\bar{I}/\varepsilon_{\max}}{1+\bar{I}/\varepsilon} \\ f_\varepsilon(\varepsilon) = \frac{1}{\Delta E}\int\limits_0^{\varepsilon}\varepsilon\frac{dn}{d\varepsilon}d\varepsilon = \frac{\ln\left(1+\varepsilon/\bar{I}\right)-\left(1+\bar{I}/\varepsilon\right)^{-1}}{\ln\left(1+\varepsilon_{\max}/\bar{I}\right)-\left(1+\bar{I}/\varepsilon_{\max}\right)^{-1}} \end{array} . \tag{5.5}$$

Here $f_n(\varepsilon)$ is the number of electrons per unit path length freed by a single ion and having energies within the interval $(0,\varepsilon)$ relative to their total number ΔN per unit path length. The second function in Eqs. (5.5), $f_\varepsilon(\varepsilon)$, stands for the energy per unit path length that is accumulated by all electrons within the energy interval $(0,\varepsilon)$ relative to the total electronic energy ΔE per unit path length. The expressions for ΔN and ΔE are given in Eqs. (5.3). Obviously, both functions in Eqs. (5.5) depend only on the mean binding energy $\bar{I}$ (target

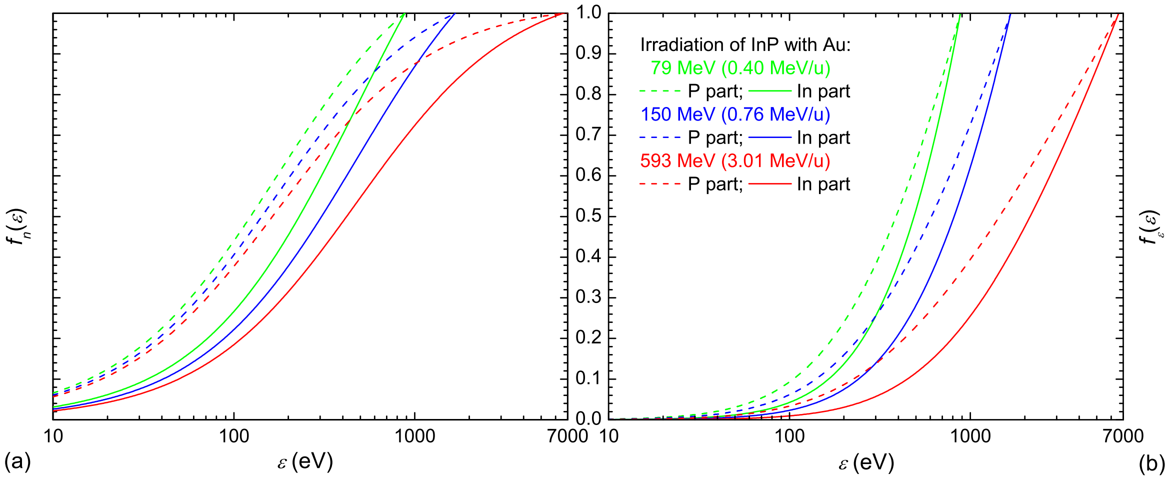

Fig. 5.2: Energy distributions of electrons freed by SHI's. The functions $f_n(\varepsilon)$ (a), and $f_\varepsilon(\varepsilon)$ (b) given by Eqs. (5.5), for different representative SHI irradiations [20]. The former function stands for the number of electrons per unit path length freed by a single ion and having energies within the interval (0, ε) relative to their total number per ion and unit path length. The latter function represents the energy per unit path length that is accumulated by all electrons within the energy interval (0, ε) relative to the total electronic energy per ion and unit path length. The description given in (b) is valid for (a) as well.

property) and on the maximum electron energy ε_{max} (ion property). The latter value, in its turn, depends only on the ion velocity [see Eq. (5.2) above]. Therefore, different SHI's having almost equal specific energy E/M_1 (like 390 MeV Xe and 593 MeV Au, see Table 3.4) will be represented by virtually the same $f_n(\varepsilon)$ and $f_\varepsilon(\varepsilon)$ functions. The energy distributions given in Eqs. (5.5) are illustrated in Fig. 5.2 for selected ion species. One can see in Fig. 5.2(a) that the fraction of electrons with an energy of $\varepsilon \leq 10$ eV is about 2-6%, and their total energy is in all cases less than 1% of the ion energy loss [see Fig. 5.2(b)]. The fraction of electrons within the energy range of 10-100 eV varies between 15% and 40%, and their total energy is limited to 10% in the maximum. Contrary, very fast electrons ($\varepsilon \geq 1$ keV) can constitute up to 25% of the total freed electrons but can carry up to 75% of the total energy lost by the ions. Finally, a major part of the electrons belongs to an intermediate energy range from 100 eV to 1 keV [cf. also with the mean energies of the electrons obtained from Eqs. (5.4)] and share from 25% to 90% of the total electronic energy depending on the SHI velocity.

In order to calculate the projected ranges r_p of the energetic electrons escaping from the initial ionisation spikes, we have used the CASINO Monte Carlo code (version 2.42) [86]. As an illustrative example, Fig. 5.3 shows the range distributions of 200 eV, 500 eV, 1 keV, and 2 keV electrons in InP. One can see that the mean projected range of such electrons varies from units to tens of nanometres.

It should be mentioned that the basic Eq. (5.1) supposes that all (initially bound) electrons have equal binding energy I. In practice, however, the electron binding energies in the outermost and the innermost electronic shells of heavy atoms (e.g, In) can differ by 3-4 orders of magnitude. Nevertheless, Eq. (5.1) holds for any specific electronic shell and can be applied for practical calculations providing that absolute or relative ionisation cross-sections are known for each electronic shell. Such cross-sections were calculated using the CASP code by Grande and Schiwietz [87]. The results of the corresponding CASP calculations show that

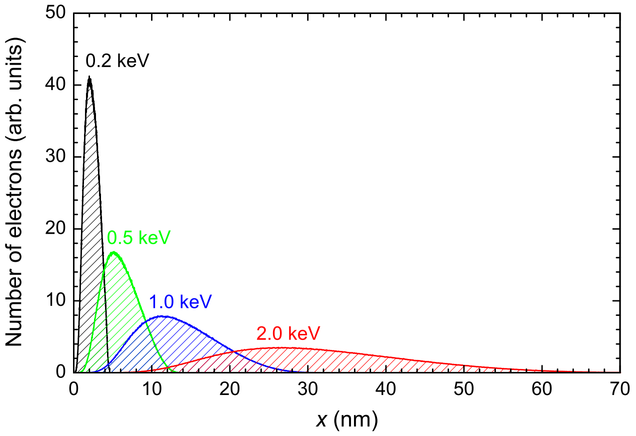

Fig. 5.3: Range distribution of fast electrons. Range distribution of electrons [20] with initial energy of 200 eV, 500 eV, 1 keV, and 2 keV in InP as calculated by the CASINO code.

most of the SHI energy is spent to outer electronic shells. So as fast ions are decelerated mainly through ionisation of target atoms and much less through excitation of valence- and conduction-band states [69], we can neglect excitation events and consider the cross-sections Q_e calculated by the CASP code as related only to ionisation energy losses that are caused by SHI interaction with each specific electronic shell of the target atoms. That is, the ΔE value in Eqs. (5.3) can be substituted by the corresponding partial energy loss of the ion due to interaction with the ith shell

$$\varepsilon_e^{(i)} = \frac{Q_e^{(i)}}{\sum\limits_k Q_e^{(k)}} \varepsilon_e, \tag{5.6}$$

where ε_e is the total energy loss of the ion per unit path length. The performed substitution allows us to calculate the term ψ from the last expression[1] in Eqs. (5.3) and put it into the first expression. In this way one obtains the number of electrons detached from each specific shell $\Delta N^{(i)}$. Finally, the summation over all electronic shells of the two atom species provides the total number of freed electrons $\Delta N_e^{(total)}$ per unit path length, $\Delta N_e^{(total)} = \sum\limits_i \Delta N^{(i)}$.

In the next step the initial radial distribution of electrons detached by a single SHI from their host atoms is considered. The formula for the impact parameter (r) dependent ion energy loss [53] in a single collision of an ion with an electron can be rewritten as

$$\varepsilon(r) = \frac{(b_\mathrm{e}/2)^2}{(b_\mathrm{e}/2)^2 + r^2} \varepsilon_{max} \quad \text{with} \quad b_\mathrm{e} = \frac{Z_1 e_0^2}{4\pi\varepsilon_0} \frac{1}{E_1} \frac{M_1}{m_\mathrm{e}}. \tag{5.7}$$

From this one obtains the impact-parameter-dependent energy transfer to a single electron (i.e., the initial radial distribution) in the approximation of the free electron gas according to

$$\varepsilon(r) = \frac{\varepsilon_\mathrm{max}}{1+\chi^2 r^2}, \quad \text{where} \quad \chi = \frac{4\pi\varepsilon_0 m_e v^2}{Z_1 e_0^2} = \frac{2\pi\varepsilon_0 \varepsilon_{max}}{Z_1 e_0^2}. \tag{5.8}$$

For non-bare ions the charge Z_1 of the nucleus must be replaced by their mean ionisation degree q_{mean}. The last equation allows to calculate the maximum distance at which an electron in the outermost electronic shell of a target atom can be detached from its host atom (this distance is limited by the energy gap E_g of the target),

$$r_\mathrm{max} = \frac{1}{\chi}\left(\frac{\varepsilon_\mathrm{max}}{E_\mathrm{g}} - 1\right)^{1/2}. \tag{5.9}$$

The mean equilibrium charge state q_{mean} of the ion can be calculated by using the formulas given by Schiwietz *et al.* [69]. The calculations yield, for the example of 250 MeV Xe, $r_{max} \cong 1$ nm and $\Delta N_e^{(total)} = 189$ nm^{-1}. Therefore, the initial density of the freed elec-

---

[1] The electron shell binding energies $I^{(i)}$ for elements were taken from G. Williams' WWW compilation (see `http://www.jlab.org/~gwyn/ebindene.html` or `http://www.webelements.com`). The data are adapted from Refs. [88–90].

trons equals approximately 6x10^{22} cm^{-3} and is comparable with the atomic density of InP (3.96x10^{22} cm^{-3}).

Now the temporal evolution of the ionisation spikes will be considered. Unfortunately, unlike the initial stage of the formation of the ionisation spikes, the cooling stage is not so well studied. First, the differently hot carriers redistribute energy among themselves (electronic energy thermalisation). Second, they transfer some part of the energy to the surrounding cold lattice (e.g., due to the carrier-optical phonon scattering [91], which is the main mechanism for compound semiconductors consisting of light and heavy constituents). Finally, the highly excited nonequilibrium carriers in the electron-hole plasma can recombine or be scattered by ionised impurities [92], though at room temperature and at elevated temperatures the last two mechanisms are much slower than the carrier-carrier and carrier-phonon scattering processes mentioned above [44, 80, 92, 93]. Thus, the initial stage of electronic energy thermalisation is followed by a relaxation stage, where the hot carriers exchange energy with the lattice by emission and absorption of phonons, which results in a net flow of energy from the carriers to the lattice (so-called “electron-phonon coupling”). It should be mentioned that some part of nonequlibrium phonons emitted in earlier events will be reabsorbed by the charge carriers, which slows down the overall cooling process to some extent [93].

5.2 Thermal spikes

It is worth mentioning that the whole spectrum of the experimental data on the radiation damage formation and annealing in InP due to swift heavy ions presented above[2] does not conform to and cannot be explained neither by the *Coulomb spike* mechanism [21–23], nor by the *lattice-relaxation* (*athermal melting*) mechanism [28–30] because otherwise the observed radiation damage in InP formed by SHI bombardment would be essentially independent of the irradiation temperature. The last is obviously not the case as it follows, e.g., from Figs. 4.18(c) and 4.19. Contrary, the observed noticeable influence of the irradiation temperature gives a clear indication that the underlying fundamental processes are of a thermal character. Therefore, namely the thermal spike model was chosen as a basis for the following calculations.[3]

The calculation of the lattice temperature is performed on the basis of coupled differential equations of heat flow both in the electron gas and the atomic lattice [31],

$$\begin{aligned} C_e(T_e)\frac{\partial T_e}{\partial t} &= \frac{1}{r}\frac{\partial}{\partial r}\left[rK_e(T_e)\frac{\partial T_e}{\partial r}\right] - g(T_e)\,(T_e - T_a) + A(r,t) \\ C_a(T_a)\frac{\partial T_a}{\partial t} &= \frac{1}{r}\frac{\partial}{\partial r}\left[rK_a(T_a)\frac{\partial T_a}{\partial r}\right] + g(T_e)\,(T_e - T_a) \end{aligned}, \qquad (5.10)$$

---

[2] see, particularly, Sect. 4.3.3 and 4.4.

[3] See also p. 4 and p. 5 for the respective motivation and grounds.

where C_e, K_e, and C_a, K_a are the specific heat and thermal conductivity of electrons and atoms, respectively; T_e and T_a are the electronic and atomic temperature (average energy); r is the radial distance from an ion trajectory; t is the time; $g(T_e)$ is the efficiency of the energy transfer from excited electrons to the lattice (so-called electron-phonon coupling); A is the energy density [37] deposited in target electrons,

$$A(r,t) = \alpha \exp\left(-\frac{(t-t_0)^2}{2t_0^2}\right) F(r), \tag{5.11}$$

where α is a normalisation constant and t_0 is the energy deposition time [41].

As it is known from many experiments on ion irradiation of different targets, visible tracks consist of two distinct zones [94–97]. The maximum track radius r_p is determined by the range of the most energetic electrons produced by the ions (see Sect. 5.1 and Fig. 5.3). Such a wide cylindrical zone of a track is called “ultratrack”, “halo”, or “penumbra”. A much thinner cylindrical zone of primary ionization with a radius $r_c = r_{max}$ [see Eq. (5.9)] is called “infratrack” or “core”. The average accumulated dose within the track core is usually orders of magnitude higher than that in the track penumbra. Chatterjee and Schaefer [94] have proposed the following expressions for the average initial energy densities in the ion track as functions of the radial distance r from the ion path:

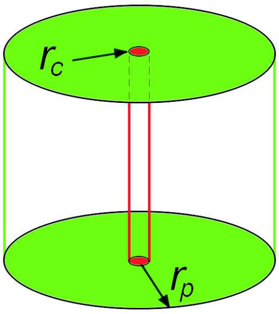

Fig. 5.4: SHI track. The radii of core (r_c) and penumbra (r_p) are shown.

$$F(r) = \rho_c + \rho_p(r), \tag{5.12}$$

where

$$\rho_c = \frac{\varepsilon_e}{2\pi r_c^2}\left[1 + \frac{1}{2\ln\left(\frac{r_p}{r_c}\sqrt{e}\right)}\right] \quad \text{for } r \le r_c\text{, and} \tag{5.13}$$

$$\rho_p(r) = \frac{\varepsilon_e}{2\pi r^2}\frac{1}{2\ln\left(\frac{r_p}{r_c}\sqrt{e}\right)} \qquad \text{for } r_c < r \le r_p \tag{5.14}$$

are the energy densities within the track core and penumbra, respectively. These densities are semi-empirical (the r^{-2} distribution comes from experiments), self-consistent (they are monotonous and finite), and (as it can be easily proven) self-normalised, i.e.,

$$\int_0^{r_p} F(r)\,2\pi r\,dr = \left(\int_0^{r_c} \rho_c\,2\pi r\,dr + \int_{r_c}^{r_p} \rho_p\,2\pi r\,dr\right) = \varepsilon_e$$

is valid.

The constant α in Eq. (5.11) can be calculated from the normalisation condition for the initial energy density $A(r,t)$ by

$$\int_{t=0}^{\infty}\int_{r=0}^{r_p} A(r,t)2\pi r dr dt = \varepsilon_e \tag{5.15}$$

As it was already mentioned, the spatial term of $A(r,t)$ [i.e., $F(r)$ in Eq. (5.11)] is self-normalised. The integration of the time-dependent term of $A(r,t)$ yields

$$\int_{0}^{\infty} e^{-\frac{(t-t_0)^2}{2t_0^2}} dt = t_0\sqrt{2}\int_{1/\sqrt{2}}^{\infty} e^{-x^2} dx = t_0\sqrt{\frac{\pi}{2}}\,\mathrm{erfc}\left(\sqrt{\frac{1}{2}}\right) \cong 0.398 t_0. \tag{5.16}$$

As a consequence of Eq. (5.16) α is given by

$$\alpha \cong (0.398 t_0)^{-1}. \tag{5.17}$$

Further, by analogy with the initial distribution of the energy density [see Eqs. (5.13) and (5.14)], the radial distribution of the free electron concentration $n_e(r)$ is given by

$$n_e(r) = \begin{cases} \frac{N^*}{\pi r_c^2} & \text{for} \quad r \le r_c \\ \frac{N^*}{\pi r^2} e^{1-r/r_c} & \text{for} \quad r_c \le r \le r_p \end{cases}, \tag{5.18}$$

where N^* is a normalisation constant that is determined from

$$\int_{0}^{r_p} n_e(r)2\pi r dr = \Delta N_e^{(total)} \tag{5.19}$$

with $\Delta N_e^{(total)}$ being the total number of freed electrons per ion and unit path length (it is calculated as described in Sect. 5.1).

The electron-phonon coupling efficiency [40]

$$g = \frac{\pi^2 m_e n_e v_s^2}{6\tau_e(T_e)T_e} \tag{5.20}$$

was introduced originally for metals [98]. Here n_e is the volume concentration of free electrons, v_s is the sound velocity, and $\tau_e(T_e)$ is the mean free time between two electronic collisions at temperature T_e [40]. However, as it is known from laser experiments on the temporal evolution of the optical properties of various semiconductors [69, 80, 82], the energy gap closes and one observes a metallic behaviour if about 10% of the valence electrons are promoted into the conduction band. As it was shown above, this condition holds in the wake of a SHI, i.e, close to the ion path. Further, as it was suggested by other authors, hot electrons in conduction bands of nonmetallic solids will behave like hot electrons in a metal [41, 99]. Thus, Eq. (5.20) will be used in this study as well.

5.3 Data used for the calculations

The $C_e(T_e)$ and $K_e(T_e)$ dependences are not known for InP. Therefore, it was assumed that freed electrons with high energies can be considered as quasi-free particles (see above). Consequently, the specific heat $C_e = \frac{3}{2}k_B n_e$ and the thermal conductivity of the electrons $K_e = C_e D_e$, where k_B is the Boltzmann constant, D_e is the thermal diffusivity of electrons (its value is unknown for InP; D_e is taken to be 5 cm^2/s close to the value used by Meftah *et al.* [41] for yttrium iron garnet). The temperature dependences of C_a and K_a taken from available table data [55, 100] are shown in Fig. 5.5.

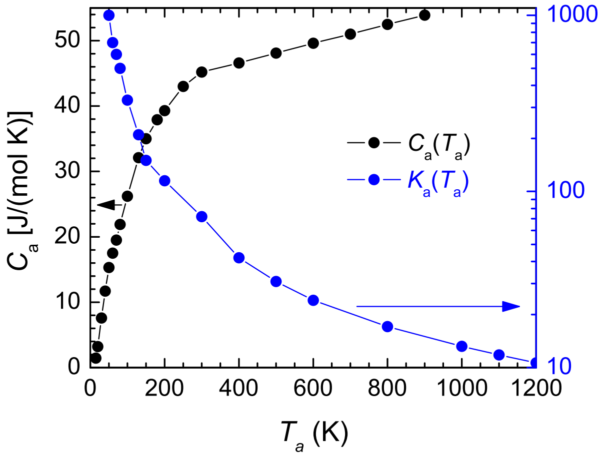

Fig. 5.5: Thermal properties of InP. Temperature dependence of the specific heat C_a and the thermal conductivity K_a of InP lattice [20]. To our knowledge, there are no data on the thermal properties of InP for higher temperatures in literature; therefore, the presented curves are extrapolated.

The value of the average sound velocity v_s = 5130 m/s is from Ref. [101]. The parameter t_0 in Eq. (5.11) was taken to be equal to 5x10^{-15} s. Izui suggested that the energy is shared between electrons within ca. 1x10^{-15} s [102]. However, a variation of this value within (1-5)x10^{-15} s has almost no influence on the results of the calculations.[4] On the contrary, the parameter τ_e strongly influences the results of the calculations and cannot be taken arbitrarily. Instead, τ_e can be estimated from available experimental data. For that we have used the data on ion track formation in InP presented by Herre *et al.* in Ref. [9]. Particularly, the TEM results shown there suggest that in the case of 250 MeV Xe irradiations at RT rather continuous tracks extend up to depths of approximately 7 μm and discontinuous tracks reach a depth of about 10 μm. The electronic energy loss of the Xe ions at 7 μm and at 10 μm is 16.1 keV/nm and 13.4 keV/nm, respectively (see Fig. 5.6).

As suggested by Komarov *et al.* [103, 104], discontinuous tracks are formed due to statistical fluctuations of the SHI charge because of electron capture and loss processes. The statistical fluctuations of the ion charge are immediately followed by the corresponding fluctuations of the momentary energy loss ε_{mom}. Thus, if ε_{mom} is only slightly higher than the threshold value for track formation ε_e^{thr}, a capture of one or more electrons by a SHI

---

[4] Because of the applied uniform time grid to be mentioned below, taking 5x10^{-15} s instead of 1x10^{-15} s allows us to use five times larger time steps in the finite difference schemes for Eqs. (5.10) and thus results in a very substantial saving of the processor time.

can reduce ε_{mom} below ε_e^{thr}. Similarly, if ε_{mom} is only slightly lower than ε_e^{thr}, a loss of one or more electrons by a SHI can increase ε_{mom} so that it will be higher than ε_e^{thr}. In this way a discontinuous track is formed; the lengths of its isolated parts are determined by the probabilities of electron capture or loss [68] by the SHI. Let us denote the mean energy loss at depth z as $\overline{\varepsilon}$ and its standard deviation as $\Delta\varepsilon$ ($\Delta\varepsilon > 0$). Therefore, discontinuous (continuous) tracks extend up to the depth, where $(\overline{\varepsilon} \pm \Delta\varepsilon) = \varepsilon_e^{thr}$, respectively. Assuming $\Delta\varepsilon(7\ \mu\mathrm{m}) \approx \Delta\varepsilon(10\ \mu\mathrm{m})$, the value of ε_e^{thr} can be easily estimated for Xe irradiation: $\varepsilon_e^{thr} \approx 14.8$ keV/nm. This value corresponds to the energy loss of a Xe ion with energy of about 100 MeV. Therefore, 100 MeV was taken to be the threshold energy for track formation in InP by Xe irradiation. Within the thermal spike model this means that the ion locally heats the target exactly up to the melting point T_m of 1335 K. This condition was used to determine τ_e. Namely, the value of τ_e is first set arbitrarily, and then is varied in finite steps until the calculated maximum atomic temperature at the ion track axis equals T_m. The resulting value[5] of τ_e ($8.5\mathrm{x}10^{-17}$ s) is afterwards used for all other ion species and energies; additionally, it is considered to be constant, because its temperature dependence is not known. Taking the calculated value of $6\mathrm{x}10^{22}$ cm^{-3} as estimation of the concentration of the freed electrons within ionisation spikes (see Sect. 5.1), the electron-phonon coupling efficiency g can be calculated by using Eq. (5.20). So, for example, at the initial stage of the electron cooling the "hot" electrons can have temperatures up to 10^4-10^5 K, which leads to g = $2.8\mathrm{x}10^{11}$-$2.8\mathrm{x}10^{12}$ W/(cm^3 K). At the final stage of the electron cooling g amounts to

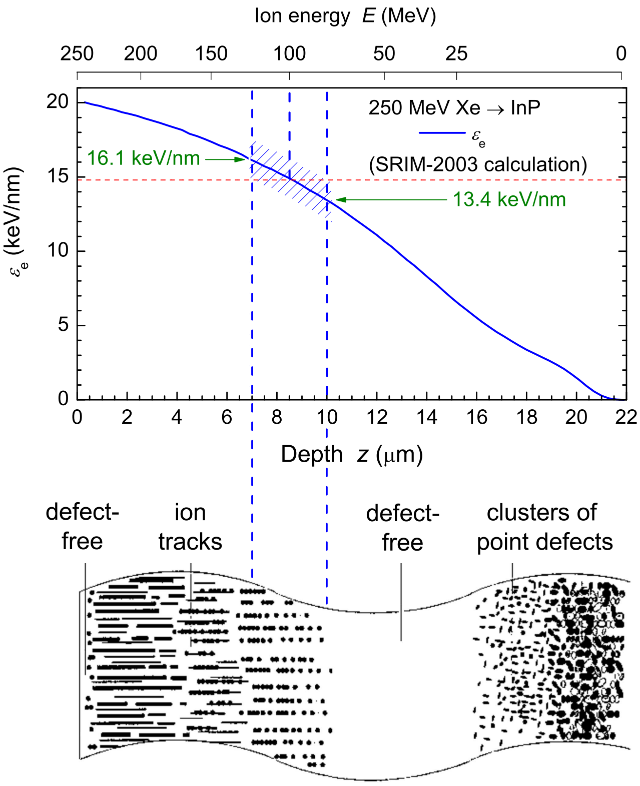

Fig. 5.6: Mean electronic energy loss of 250 MeV Xe in InP. Depth dependence of the ion energy and the corresponding mean electronic energy loss ε_e of 250 MeV Xe in InP (solid line, SRIM-2003 [58] calculations). The hatched area schematically illustrates a possible deviation (not to scale) of ε_e from its mean value (represented by the solid line, see above) due to statistical fluctuations of the momentary ion charge q. The vertical dashed lines mark the depths of 7 μm and 10 μm where respectively rather continuous or discontinuous tracks disappear (cf. with the bottom part of the figure that schematically summarises the panorama-view XTEM images [9] presented in Fig. 1.1).

---

[5] This value is relatively small; however, such a short free time between two collisions is not impossible, as follows, e.g., from the high electron-phonon scattering rates presented by Arnold and Cartier [105].

about 9.3x10^{13} W/(cm^3 K) when the electronic temperature approaches room temperature.

Finally, the initial and boundary conditions for both Eqs. (5.10) are the following ones

$$T(r,0) = T(R,t) = T_0; \quad \lim_{r \to 0} r^m K(T) \frac{\partial T}{\partial r} = 0, \tag{5.21}$$

where R is some constant value chosen arbitrarily so that $R >> r_p$, and T_0 is the initial temperature of the target. The second condition in Eq. (5.21) merely demands that all spatial gradients of the temperature be finite.

5.4 Calculations

The numerical solution of the system of differential equations (5.10) with the initial and boundary conditions (5.21) has been performed using our program code HEAT [20, 106]. We have used nonuniform spatial and uniform time grids. The constructed high accuracy scheme for the differential equations with variable coefficients was proven to be converging to the exact solution with the rate $O(h^2 + \tau)$, where h and τ are spatial and time grid steps, respectively. The details of the mathematical model can be found in Ref. [106].

5.5 Calculation results

It has to be mentioned that in our calculations of the atomic temperature in InP, the latent heat of melting is not taken into account. Namely, we have supposed that in order to melt material locally, it is enough to heat the atomic lattice up to the melting point. This can be qualitatively understood, if keeping in mind that atoms located within an ionisation spike have lost most of the valence electrons and, hence, the chemical bonding among ionised atoms must be much weaker than in normal state.

As an example, Fig. 5.7 shows the temporal evolution of the radial distributions of the electronic (T_e) and atomic (T_a) temperature (average energy) in InP irradiated with 390 MeV Xe at RT [see parts (a) and (b), respectively]. One can see that within the time span from 0.1 ps to 3 ps the electronic temperature decreases by about an order of magnitude at the track axis (i.e., at $r = 0$). This is caused by an efficient redistribution of the energy among electrons and by the energy transfer to the atomic lattice via electron-phonon coupling (see Sect. 5.1 and 5.2). As a result of the electron-phonon coupling, the atomic temperature at the track axis increases from the initial value (i.e., from RT) up to the melting point T_m in about 1 ps. Contrary, at larger distances the maximum temperature is reached much later [e.g., cf. the respective $T_a(r)$ distributions for 1 ps, 1.5 ps, 2 ps, and 3 ps shown in Fig. 5.7(b)]. The radius of the molten zone reaches its maximum value at approx. 1.5 ps, whereupon a cooling stage

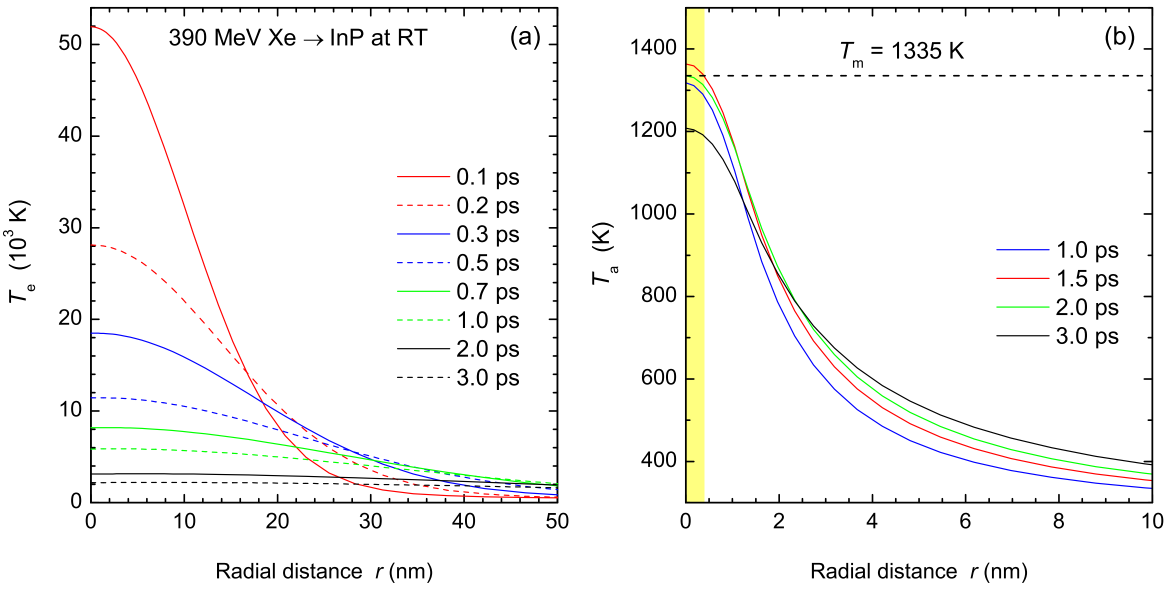

Fig. 5.7: Thermal spikes in InP irradiated with 390 MeV Xe at RT. Radial distributions of the (a) electronic and (b) atomic temperature in InP bombarded with 390 MeV Xe at RT [please, note the different scale of the horizontal and vertical axes in parts (a) and (b)]. Multiple curves in both parts stand for different moments of time t. Further, the curve for $t = 1.5$ ps in part (b) corresponds to the moment of time where the radius of the molten track reaches its maximum value r_{sim} [i.e., where the melting point T_m (1335 K, see Table 3.1) is reached at the maximum radial distance r from the track core axis, as it is illustrated by the light yellow area].

comes into play.[6]

The main calculation results for different experimental conditions (ion species and irradiation temperature) are depicted in Fig. 5.8. Fig. 5.8(a) shows the maximum atomic temperature in InP at the ion track axis as a function of the ion species and energy. One can see that for RT-irradiations with Au and Xe, the calculated maximum atomic temperatures exceed the melting point T_m within a certain range of ion energies. Contrary, for RT-irradiations with Kr and for all LNT-irradiations, the calculated maximum atomic temperatures are lower than T_m. The resulting radii of the molten tracks formed by Au and Xe at RT are depicted in Fig. 5.8(b). This figure shows that the calculated radii vary with the ion species and energy. One can see that the calculated radii of the molten tracks correlate with the available TEM results on Xe and Au irradiation of InP. Similar calculations were performed for RT-irradiations with Pb as well. The corresponding line for Pb lies only slightly above that for Au and, therefore, it is omitted in the figure. For example, the calculated track radii amount to 2.4 nm (not shown) in the case of 385 MeV Pb irradiation at RT and, hence, are in a good agreement with the TEM results presented by Szenes *et al.* (see [13]). Further, Fig. 5.8(b) demonstrates that there are “low-” and “high-energy” thresholds for melting, which are different for lighter and heavier ions. Finally, there appears to be no universal (i.e., valid for all ion species) “low-energy” RT-threshold for melting (the only measure used commonly

---

[6] The calculated values of the solid-liquid phase transition mentioned above (i.e., from 1 ps to 3 ps) correlate well with the results obtained by Bonse *et al.* for InP irradiated with ultrafast laser pulses [107]. Particularly, 150 fs laser pulses above the threshold of 0.16 J/cm^2 were found to cause an *ultrafast thermal melting* of the material within 1-2 ps.

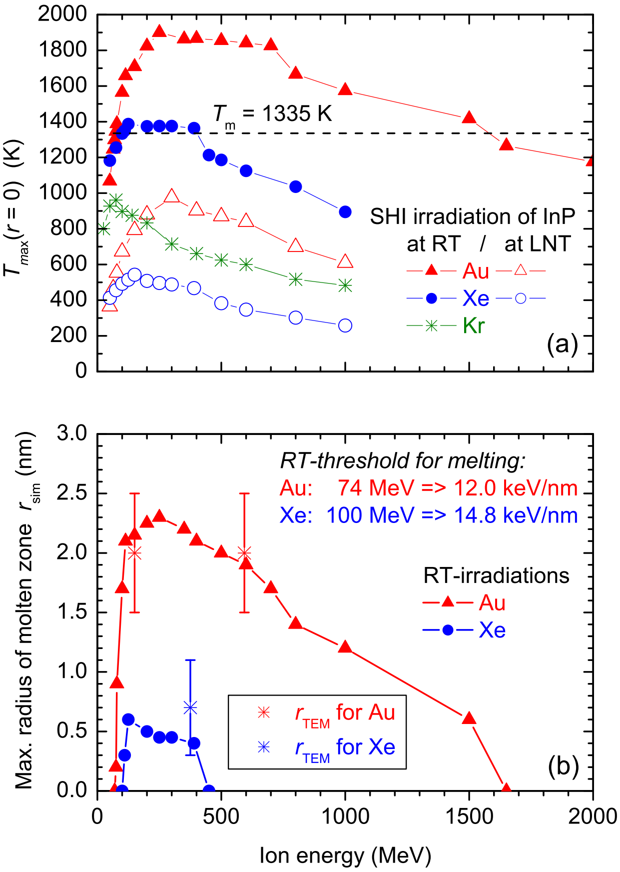

Fig. 5.8: Results of the thermal spike modelling. (a) Dependence of the maximum atomic temperature at the ion track axis ($r = 0$) on the ion energy for various ion species [20]. The data are presented for both RT- and LNT-irradiations. The dashed line corresponds to the melting point of InP (1335 K). (b) Dependence of the calculated maximum radius of the molten zone, r_{sim} , on the ion energy for various ion species [20]. The data are shown solely for RT-irradiations. The "low-energy" RT-thresholds for melting are presented. Data points obtained from TEM for 150 MeV Au, 593 MeV Au, and 375 MeV Xe are also shown for comparison.

in the literature). More specifically, the threshold energy loss ε_e^{thr} is higher for ions having lower atomic number Z_1 (cf. the estimated values of ε_e^{thr} for Au and Xe of 12.0 keV/nm and 14.8 keV/nm, respectively).

To sum up, the obtained calculation results are self-consistent and correlate well with the data available from the TEM investigations. Therefore, the extended thermal spike model (see Sections 5.1, 5.2 and 5.3) correctly describes the formation of ion tracks in InP due to (above-threshold) SHI irradiation and allows to calculate their spatial dimensions.

Chapter 6

Discussion

In the following the main experimental and theoretical results obtained for various SHI irradiation conditions and for different target materials (Ge, GaAs, and InP) will be analysed and compared to each other.

6.1 Origin of the radiation damage in InP

As it was shown in Sect. 4.3, SHI irradiation of virgin InP in above-threshold electronic regimes causes the lattice disordering up to amorphisation. In order to check for the possible influence of nuclear energy deposition, we recalculated the values of the ion fluences used (see Table 3.4) into the relative concentration of displacements n_{dpa} (in commonly used units of displacements per atom, dpa) according to

$$n_{dpa} = N_v N_I / N_a, \tag{6.1}$$

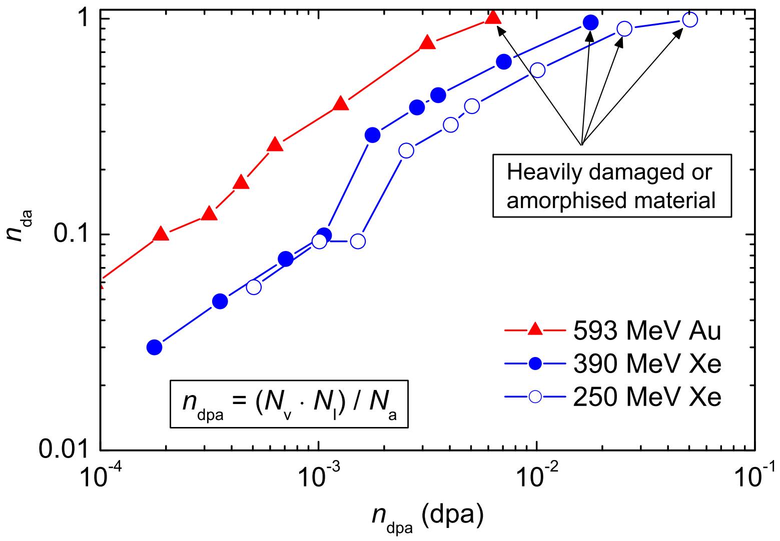

Fig. 6.1: Origin of the radiation damage in InP. Measured damage concentration n_{da} (from RBS studies) versus the calculated relative concentration of displacements n_{dpa} [20].

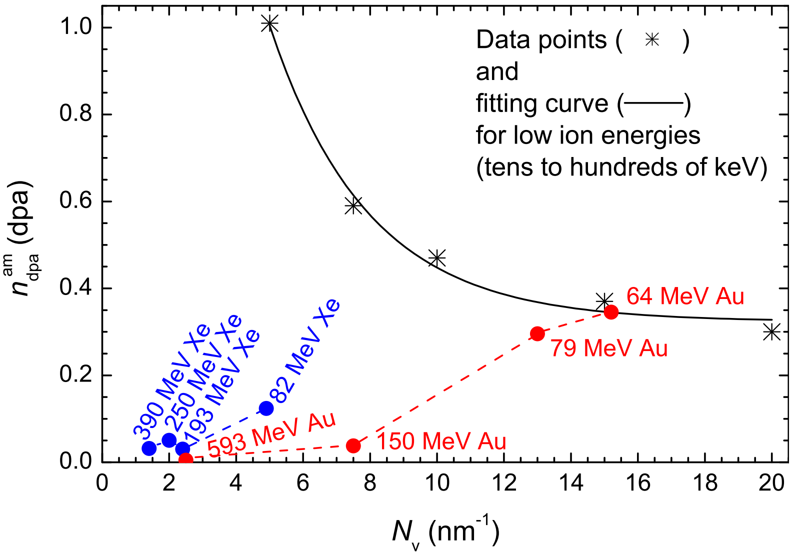

Fig. 6.2: Amorphisation threshold for low- and high-energy irradiation. Relative concentration of displacements necessary to amorphise material, n_{dpa}^{am}, versus the number of vacancies per unit path length N_v [20].

where N_v and N_I are the number of vacancies[1] per ion and unit path length and the ion fluence, respectively, and N_a = 3.96x10^{22} cm^{-3} is the atomic density of InP (see Table 3.1). Fig. 6.1 shows the measured damage concentration n_{da} (obtained by means of RBS and channelling technique) as a function of n_{dpa} calculated for some above-threshold irradiations. The data points at $n_{da} \approx 1$ marked by arrows in the figure demonstrate that the material is already very heavily damaged and partially amorphised, while the relative vacancy concentration is still very low: it amounts to only 0.5-3% of the atomic density of InP. Obviously, the damage measured is too high to be caused by the nuclear energy loss of the ions. Therefore, the *nuclear energy loss alone* cannot account for the damage formation illustrated in Fig. 6.1; instead, the observed large radiation damage has to be attributed to the *high electronic energy deposition* [18].

In contrast to the above-threshold irradiations, in the case of sub-threshold and near-threshold irradiations (i.e., for 82 MeV Xe, 64 MeV Au, and 79 MeV Au, see Table 3.4) the nuclear energy loss of the ions can play a more important role, or can even turn into the *dominating mechanism* of damage formation. This is illustrated in Fig. 6.2, which shows the relative concentration of displacements necessary to amorphise material (n_{dpa}^{am}) versus the calculated number of vacancies per ion and unit path length N_v. The results previously reported by Wendler *et al.* [72] for low ion energies of tens to hundreds of keV (where damaging is determined by nuclear energy loss) are shown for comparison. One can see in Fig. 6.2 that the data points for 64 MeV and 79 MeV Au irradiations are very close to the curve for the low energies. Therefore, in those two cases the radiation damage is at least to a large part due to the nuclear energy loss, which qualitatively explains our observation that the experimental values $n_{da}(N_I)$ for 64 MeV and 79 MeV Au irradiations cannot be fitted by single curves in the framework of the Gibbons' model [see Fig. 4.19(a)].

---

[1] As calculated by using the SRIM-2003 code [58], see Table 3.4.

6.2 Formation and overlapping of ion tracks in InP

Figure 6.3 shows a PV-TEM image of an InP sample irradiated with 593 MeV at RT. One can see in the figure both single ion tracks (marked by circles) and overlapping tracks (marked by arrows). The radii of the single isolated tracks were measured by a series of PV-TEM images taken with the same or higher magnification from various parts of the sample surface. The largest isolated tracks with radii from 3.0 nm to 4.5 nm are rather rare; their number does not exceed 5% of the total number of tracks. If the largest (very seldom observed) tracks[2] are not taken into consideration, the radii of smaller isolated tracks (that constitute the absolute majority of all isolated tracks) vary between 1.5 nm and 2.5 nm. The same range of isolated track radii is also observed for 150 MeV Au irradiations. Those values are in good agreement with the calculated radii of molten zones [see Fig. 5.8(b)].

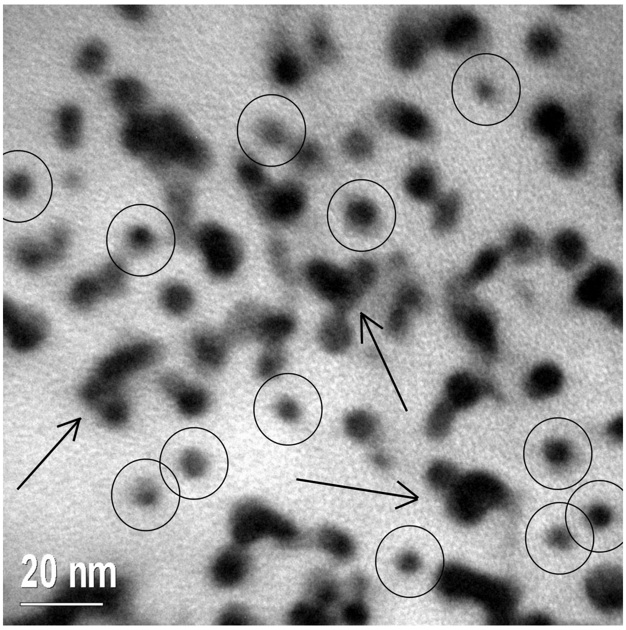

Fig. 6.3: Single- and multiple-ion tracks. PV-TEM image of an InP sample irradiated at RT with 593 MeV Au up to a fluence of 9x10^{11} cm^{-2} [20]. The circles mark (most likely) single ion tracks and the arrows point to areas containing at least 3-4 overlapping tracks.

Further, the calculated radii of molten zones in virgin InP irradiated with 193 MeV Xe, 250 MeV Xe, or 390 MeV Xe do not exceed 0.6 nm [see Fig. 5.8(b)]. This value is only slightly larger than the lattice constant of InP (0.586 nm, see Table 3.1). Therefore, not tracks, but rather point defects and point defect clusters are formed at first in virgin InP by fast Xe ions.[3] Nevertheless, with increasing Xe ion fluence more and more radiation damage is created in form of point defects and point defect clusters, which increases the probability that subsequent Xe projectiles hit areas already damaged by preceding ions. Electrons freed by such ions from their host atoms no longer "see" the perfect virgin atomic lattice, but a more or less disordered one. Consequently, they interact more strongly with the atoms, causing a faster transfer of energy from the excited electrons into the lattice, which in its turn

---

[2] See Table 4.2 and Sect. 4.5, p. 42.

[3] See also discussion of the respective TEM results (Sect. 4.5, p. 40).

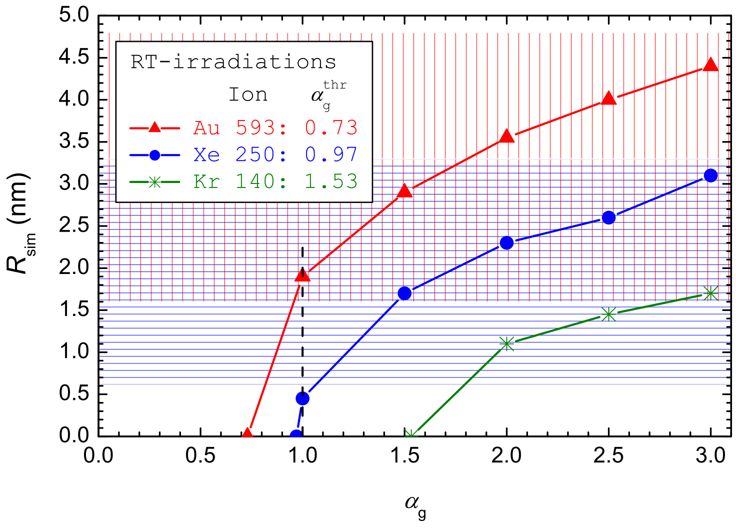

Fig. 6.4: Simulated ion track radii in disordered InP. Radii of molten tracks calculated by the HEAT code in disordered InP assuming different predamage level and, thus, increased electron-phonon coupling efficiency g [20]. The threshold values of the factor α_g are also shown (see text for details). The hatched areas illustrate the respective intervals of the track radii obtained by TEM for Xe or Au irradiation at RT (see Sect. 4.5).

favours the formation of visible ion tracks.[4]

In terms of the thermal spike model a more efficient transfer of energy from excited electrons to the lattice means that the electron-phonon coupling efficiency g [see Eq. (5.20)] becomes higher with increasing damage concentration. In order to estimate the qualitative influence of this effect on track formation, we have performed calculations with all the same parameters as previously (i.e., the results shown in Fig. 5.8), but multiplied the values of g by a factor α_g. The values of molten track radii R_{sim} calculated in this way for selected ion species are shown in Fig. 6.4. The case of $\alpha_g = 1$ corresponds to SHI irradiations into perfectly ordered virgin material, while data points with $\alpha_g > 1$ are for predamaged InP. Finally, the data points for $\alpha_g < 1$ have no direct physical meaning, because the electron-phonon coupling efficiency cannot be lower than that for the perfectly ordered material. Nevertheless, the position at which the calculated curve crosses the abscissa, α_g^{thr}, allows us to predict, whether a certain SHI irradiation of the virgin material will result in track formation. One can expect rather continuous tracks if α_g^{thr} is noticeably lower than unity, rather discontinuous tracks if α_g^{thr} is close to unity, and, finally, no tracks are to be expected if this value is noticeably larger than unity. This conclusion is supported by the RBS and TEM investigations presented in Sect. 4.3.3 and 4.5. For example, no tracks in crystalline InP were formed by Kr irradiation with $\alpha_g^{thr} \approx 1.5$. However, even in this case tracks can be created if the ions penetrate heavily damaged areas or suffer an instantaneous loss of many electrons (though the latter event has a relatively low probability).

Further, Fig. 6.4 demonstrates that the whole interval of the track radii determined from the TEM investigations (see the blue and the red hatched areas in the figure) can be described

---

[4] Additionally, the thermal conductivity of the disordered lattice can be lower than that of the perfect one (e.g., in the case of highly disordered $Si_{80}Ge_{20}$ alloy a calculated reduction in the thermal conductivity amounts to 32% [108]). However, our calculations by using the HEAT code show that such a reduction in the thermal conductivity of InP does not lead to a very large increase in the maximum temperatures within track regions.

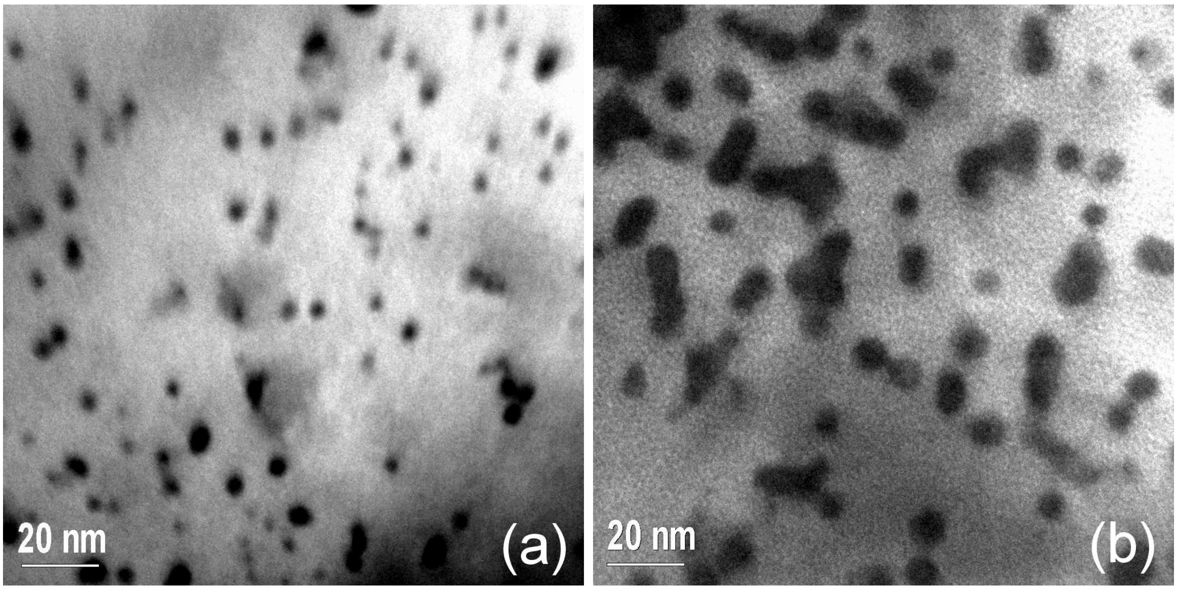

Fig. 6.5: InP irradiation with different ion species: Xe vs. Au. Bright-field PV-TEM images of InP irradiated at RT with (a) 375 MeV Xe, or (b) 593 MeV Au. The ion fluence N_I equals ca. 8.4x10^{11} cm^{-2} in both cases.

in the framework of the extended thermal spike model (see Sect. 5.2) by assuming that the electron-phonon coupling efficiency g increases with damage concentration and for very high lattice disorder arrives at a value that is about 3 times larger than that for the perfectly ordered material.[5]

The results obtained for LNT-irradiations with 390 MeV Xe and 593 MeV Au show that the very first Xe or Au ions impinging perfectly ordered InP cannot create tracks, but only point defects and point defect clusters. This follows from the fact that, first, one overlap is necessary to fit the corresponding experimental $n_{da}(N_I)$ curves [see Fig. 4.19(b)] and, second, the calculations give radii of the molten zones of $r_{sim} = 0$ [see Fig. 5.8(b)]. This also explains why no tracks were observed by Gaiduk *et al.* [11] in InP irradiated at LNT with a relatively low fluence of 7x10^{12} cm^{-2} of 250 MeV Xe ions. Contrary, subsequent Xe or Au ions are able to form discontinuous tracks at LNT (e.g., for the much higher Xe ion fluence of 3x10^{13} cm^{-2}, see Fig. 4.33) by hitting damaged zones already created by preceding ions.[6]

Fig. 6.5 provides an illustrative comparison between efficiencies of the radiation damage formation and accumulation in InP bombarded at RT either with 375 MeV Xe or 593 MeV Au ions [parts (a) and (b), respectively]. In both cases the ion fluence equals approximately 8.4x10^{11} cm^{-2}. Obviously, the irradiation with Au results in formation of noticeably larger tracks as compared with the Xe irradiation. This conclusion is valid both for single-ion tracks and multiple-ion (i.e., overlapping) tracks. The last observation correlates well with the simulation results on the molten track radii in virgin and disordered InP [see Figs. 5.8(b) and 6.4, respectively].

---

[5] I.e., the value of the α_g increases from its initial value of unity to about three.

[6] See the discussion above, p. 61.

6.3 Calculated *vs.* experimental values of ion track radii in InP

Let us compare the values of the track radii obtained by the calculations with the HEAT code (see Sect. 5.4 and 5.5) to those resulting from RBS and TEM investigations. These values are summarised in Table 6.1.

Ion	E (MeV)	T_I	m_{RBS}	r_{sim} (nm)	r_{RBS} (nm)	r_{TEM} (nm)
Xe	193	RT	0	0.50	1.2±0.1	—
Xe	250	RT	0	0.45	1.3±0.1	1.0–4.0
Xe	375	RT	0	0.40	—	0.6–2.8
Xe	390	RT	0	0.40	1.4±0.1	—
Au	79	RT	0	0.90	1.1±0.1	—
Au	150	RT	0	2.15	2.3±0.1	1.5–3.5
Au	573	RT	–	1.90	—	1.7–3.5
Au	593	RT	0	1.90	3.0±0.2	1.5–4.5
Xe	82	RT	1	0	1.6±0.1	—
Xe	390	LNT	1	0	0.9±0.1	1.5–3.0
Au	593	LNT	1	0	3.9±0.2	—
Kr	140	RT	–	0	—	—
Au	64	RT	0	0	1.2±0.1	—

Tab. 6.1: Damage cross-sections in InP. Ion track radii simulated by the HEAT code (r_{sim}, see Fig. 5.8), calculated from the respective RBS data (r_{RBS}, see Table 4.1), and measured by TEM (r_{TEM}, see Table 4.2) for different ion species. Here m_{RBS} is the number of overlaps obtained by fitting of the RBS data in the framework of the Gibbons model [73] for different SHI irradiations of InP (see Sect. 4.3.3).

One can see that the simulated radii r_{sim} are generally lower than both r_{RBS} and r_{TEM}. However, the values of r_{sim}, r_{RBS}, and r_{TEM} for every certain ion species can in no way be equal to each other, because all of them have different physical meaning. So, the calculated radii r_{sim} are exclusively for perfectly ordered material [see Fig. 5.8(b)]. Contrary, the data from the RBS investigations are more or less averaged values resulting from point defects, point defect clusters, and tracks.[7] Finally, the TEM data cover the range from the narrowest tracks (formed by single ions hitting undamaged crystalline areas) to wider ones (due to multiple ions hitting the same area). The diameters of the tracks vary over a broad range. Furthermore, for discontinuous tracks the general picture is even more complex, because their second spatial dimension (length) is also varied. Nevertheless, as expected, in those cases where each ion is supposed to produce a track (noticeably larger than point defect clusters and large enough to be stable, as it seems to be the case, e.g., for RT-irradiations with 150 MeV and 593 MeV Au), the calculated radii r_{sim} are close to the lower limit of the TEM radii r_{TEM}.

---

[7] Therefore, the mean track radius must be smaller than the respective value of r_{RBS}.

Contrary, for SHI irradiations with ion species producing at first no amorphous tracks but rather point defect clusters in perfectly ordered virgin material (all RT- and LNT-irradiations with Xe, and LNT-irradiations with 593 MeV Au), the values of r_{sim} and r_{RBS} are generally smaller than the radii deduced from TEM studies.

6.4 Radiation resistance of Ge, GaAs and InP

As it was demonstrated in Chapter 4, SHI bombardment of crystalline materials leads to the formation of radiation damage. The measured damage concentration n_{da} strongly depends on the target material, ion species and energy, and irradiation temperature.

Figure 6.6 shows fluence dependences of the damage concentration n_{da} resulting from either 390 MeV Xe or 593 MeV Au irradiation of Ge, GaAs, or InP at RT. First, one can see that GaAs is slightly more radiation-resistant to both Xe and Au bombardment than Ge. Further, InP appears to be much less resistant to SHI irradiation than the two other materials studied. For example, in the case of 1x10^{13} cm^{-2} of 593 MeV Au InP is nearly amorphised, whereas the observed concentration of damage in Ge and GaAs does not exceed 1% providing the same irradiation conditions (see Fig. 6.6). Such a remarkable difference between Ge and GaAs, on the one hand, and InP, on the other hand, is very intriguing. Further, the respective damage concentrations n_{da} in Ge and GaAs are still relatively low even for the highest ion fluences used (see Fig. 6.6); the value of n_{da} saturates at ca. 1-3% during the ongoing irradiation. This demonstrates that the radiation damage formed due to the elastic stopping in single atomic cascades is not stable. This instability can be explained,

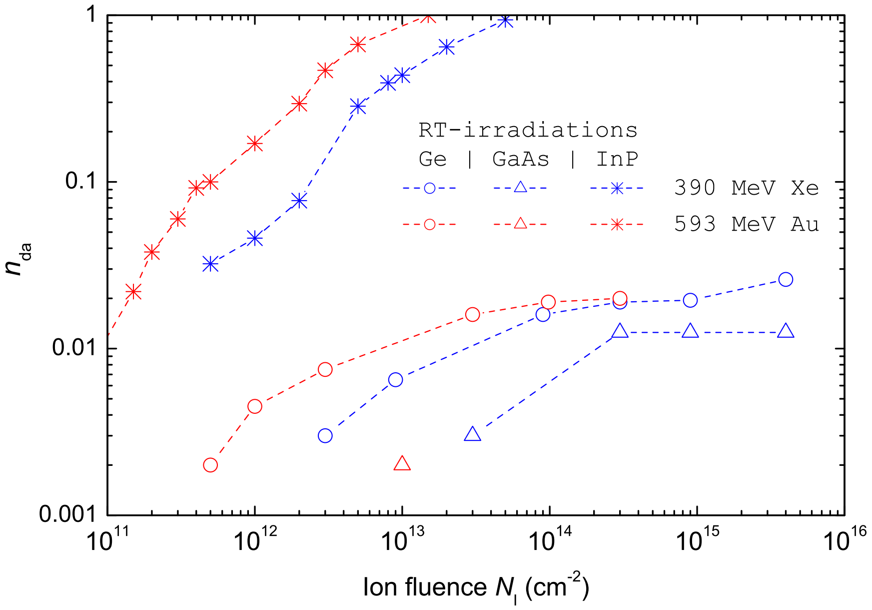

Fig. 6.6: Radiation resistance of Ge, GaAs, and InP. Fluence dependence of the damage concentration, $n_{da}(N_I)$, formed at RT with different SHI's in the studied materials.

e.g., by *efficient diffusion* and *annihilation* of point defects in Ge (provided that they are mobile at RT), or by the *damage annealing* due to the high electronic energy deposition ε_e.

It is worth mentioning that up to now no tracks were registered below 35 keV/nm in Ge or GaAs irradiated with various fast monatomic ions [109–111]. On the other hand, irradiation of Ge with 20 MeV, 30 MeV or 40 MeV fullerenes (ε_e of 37, 44, and 51 keV/nm, respectively) does result in formation of tracks [111].[8] This gives us an indication that in order to form tracks a certain threshold energy deposition must be exceeded. Therefore, as it is supposed by Komarov *et al.* [115], the threshold values of ε_e for Si, Ge, and GaAs crystals are relatively large and have not been reached during irradiations with monatomic ion beams. However, they reported on formation of noticeably discontinuous tracks in Ge irradiated with 710 MeV ^{209}Bi or 1.3 GeV ^{238}U ions [115]. The electronic energy loss ε_e of the bismuth and uranium ions is relatively high and equals respectively 35 keV/nm and 43 keV/nm as follows from the SRIM-2003 calculations. However, the tracks observed by them are more like rare strings of elongated blobs; and the total number of the tracks is more than an order of magnitude less than the ion fluence used. The authors suggest that the discontinuous track are formed in subthreshold regime and have to be ascribed to inevitable statistical fluctuations of the SHI charge state.[9] Finally, they estimated the threshold value of ε_e for continuous track formation in Ge to be about 46-49 keV/nm [115].

Therefore, it turns out that all the SHI irradiations of Ge performed in the current work are *subthreshold* ones (cf. with Table 3.3), which qualitatively explains the *low damaging efficiency* observed (see Sect. 4.1).

Further, it is worth mentioning that earlier investigations of amorphisation of various elemental and III-V binary semiconductors by a conventional implantation of 200 keV Ar$^+$ or 300 keV Se$^+$ at LNT or RT [116] also showed that the arsenides are more radiation-resistant than the phosphides and elemental semiconductors (*viz.*, Si and Ge). It was suggested that in the arsenides an efficient defect transformation and annealing occur *in situ* at RT due to high mobility of primary point defects formed by the ionic projectiles [116, 117]. Furthermore, it was stated that in the phosphides the primarily formed clusters of defects are almost stable and, therefore, the gradual transition from the initial crystalline to the final amorphous state is put into effect via damage accumulation [5, 116]. Contrary, in the arsenides point defects and point defect complexes are produced initially, whereas amorphous regions are generated by a collapse-like process.

However, it still remains to be answered why materials with similar properties (cf., e.g., GaAs and InP, see Table 3.1) behave themselves so differently under SHI irradiation. The ex-

---

[8] Ion track formation due to irradiation with MeV fullerenes is also observed in Si [112, 113] and GaAs [114].

[9] I.e., the visible by TEM isolated blobs constituting the ion tracks are believed to be formed due to ion-atomic collisions leading to instantaneous loss of many electrons by the SHI. Such an event noticeably increases the momentary energy loss, that in this way might exceed the threshold for track formation ε_e^{thr} until the next ion-charge-changing process comes into play (see also Sect. 5.3, p. 53).

isting models that try to answer this question are divided into two basic classes. The first class is constituted by the so-called “topological” models that relate the radiation resistance of materials to their respective geometrical structure (e.g., see Ref. [118]). The second large class includes various models that relate the resistance to certain physical or chemical properties of materials, like ionicity, density, elastic moduli, glass-forming ability, or melting point (as reviewed, e.g, in Ref. [119]). Nevertheless, to our knowledge, up to now no model is able to describe all different materials self-consistently.

Chapter 7

Summary and conclusions

SHI bombardment of crystalline materials leads to the formation of radiation damage. In Ge and GaAs the respective damage concentrations n_{da} are still relatively low even for the highest ion fluences used; furthermore, the value of n_{da} saturates at ca. 1-3% with the ongoing irradiation. Most probably, for these materials the threshold value of the electronic energy deposition to melt the material is not yet reached with 593 MeV Au ions which is in agreement with results published by other groups.

SHI irradiation of Ge and GaAs samples predamaged by means of conventional keV implantation leads to damage annealing. The last effect is very large for certain experimental conditions; the annealed fraction can reach 90% and more with no indication of the saturation [15, 18]. Further, the SHI-induced annealing in predamaged GaAs appears to be widely determined by the integral electronic energy density introduced by SHI's into the material. The obtained TEM results suggest that in the case of heavily predamaged but not yet amorphised materials the existing remnants of the crystalline inclusions aligned with the initially perfect lattice are "growing" under the SHI irradiation until the almost complete recrystallisation. However, the lattice recrystallised in this way is not perfect and contains micro-twins of different size and shape as well as dense twin lamellae and stacking faults [15].

Contrary, SHI bombardment of InP in above-threshold electronic stopping regimes produces very noticeable amount of radiation damage in form of point defect clusters and ion tracks [9–11] due to the high electronic energy deposition ε_e. With increasing ion fluence single-ion tracks accumulate and overlap that finally leads to formation of amorphous surface layers at large ion fluences [9, 10, 18, 19]. However, contrary to the bulk, a thin surface layer (tens of nanometres) remains almost undamaged. This feature has to be ascribed to the increasing value of ε_e with depth[1] within the first tens of nm [19]. Generally speaking, in above-threshold regimes the radiation damage production is determined by the electronic energy deposition, while in the subthreshold regime the observed damage accumulation is at least to a large part due to the nuclear energy loss.

---

[1] That is characteristic, e.g., to SHI's having an initial charge q_{init} lower than the mean equilibrium one for the bulk q_{mean}.

The RBS investigations performed prove that neither the ion energy loss per unit path length nor the total energy deposition per unit volume alone can describe SHI irradiation effects in InP. Therefore, the radial distribution of the energy deposition[2] has to be taken into account. This demand is realised in our computer code "HEAT" based on the thermal spike (TS) model. We show that the experimental data on ion track formation in InP can be qualitatively and quantitatively described on the basis of the inelastic thermal spike (TS) model that has been originally used only for metallic targets. The presented extension of the TS model on semiconductors covers mainly the very first stage of the energy transfer from SHI's (so-called "ionisation spikes"). The most important input parameter governing the electron-phonon coupling efficiency is determined from available experimental data. The calculated maximum atomic temperature exceeds the melting point within a certain interval of ion energies in the case of Xe and Au irradiation at RT, but not at LNT, and not for Kr one. The calculated track radii vary with ion energy E and thus with ε_e; further, they are reasonable and correlate well with the RBS and TEM results.[3]

Further, our simulation results prejudice the amenity of a single value of the threshold LET, ε_e^{thr} as a fundamental quantity that is commonly used for the description of track formation in solids irradiated with different ion species. So, it is shown that there is no universal RT-threshold for track formation in InP. More specifically, the threshold energy loss depends on the ion atomic number Z_1: ε_e^{thr} is higher for lighter ions (12.0 keV/nm and 14.8 keV/nm for RT irradiations with Au and Xe, respectively).

Our experimental and simulation results on the LNT-irradiations as well as on the sub-threshold irradiations at RT support the idea that the formation of visible tracks requires the material predamaging [10], unless each SHI penetrating perfectly ordered virgin InP directly produces a track that is noticeably larger than point defect clusters and large enough to be stable.

Thus, the extended TS model offers a self-consistent way to explain the influence of various irradiation conditions (ion mass, ion energy, irradiation temperature, etc.) on the ion track formation and damage accumulation in InP and, therefore, can make a contribution to a better understanding of the underlying mechanisms.

The damage annealing in conventionally predamaged InP due to SHI irradiation dominates the damage formation for the sub-threshold irradiation with 140 MeV Kr for which the damage formation in virgin InP is very low. In contrast, the above-threshold irradiations (e.g., 390 MeV Xe and 593 MeV Au) yield a much higher damage formation in virgin InP and have hardly any effect on the annealing in the pre-damaged material, but increase the defect concentration.

The performed experiments on intermixing of Bi/GaAs and Bi/InP layered systems allow one to conclude that the observed large difference between the magnitude of the intermixing

---

[2] That depends upon both ion species and ion energy.

[3] Including experimental results published by other authors.

in Bi/GaAs and Bi/InP layered systems can be easily understood if assuming that in GaAs, contrary to InP, no molten tracks are formed. It is worth mentioning that this conclusion correlates well with other RBS and TEM results presented in the current work.

Generally, on the basis of the experimental data presented for Ge, GaAs and InP, one can suggest that two concurrent processes take place *simultaneously* during SHI irradiation of solids: both radiation *damage formation* and *annealing*. Whether the first or the second one plays a more important role depends on the SHI mass and energy.

Bibliography

[1] D. STREIT: In: *Compound Semiconductors*, May 2002; D. LAMMERS: In: *Electronic Engineering Times*, September, 12, 2002; B. HUMPHREYS AND A. O'DONELL: In: *Compound Semiconductors*, August 2003; T. WHITAKER: In: *Compound Semiconductor magazine*, January 2004; D. LAMMERS: In: *Electronic Engineering Times*, March, 17, 2004

[2] G.G. BENTINI, A. GOLANSKI , AND S. KALBITZER (Eds.): *Deep implants: Fundamentals and applications (Proceedings of Symposium C, E-MRS Spring Conference, Strasbourg, France, 31 May - 2 June 1988).* NORTH-HOLLAND, 1989

[3] C.R. WIE, T. VREELAND JR., AND T.A. TOMBRELLO: In: *Nucl. Instrum. Methods B* 16 (1986), p. 44

[4] M. LEVALOIS, J.P. GIRARD, G. ALLAIS, A. HAIRIE, M.N. METZNER, AND E. PAUMIER: In: *Nucl. Instrum. Methods B* 63 (1992), p. 25

[5] W. WESCH, E. WENDLER, T. BACHMANN, AND O. HERRE: In: *Nucl. Instrum. Methods B* 96 (1995), p. 290

[6] I. JENČIČ, M.W. BENCH, I.M. ROBERTSON, M.A. KIRK: In: *J. Appl. Phys.* 78 (1995), p. 974

[7] I JENČIČ AND I.M. ROBERTSON: In: *J. Mat. Res.* 11 (1996), p. 2152

[8] I. JENČIČ, I.M. ROBERTSON, AND J. SKVARČ: In: *Nucl. Instrum. Methods B* 148 (1999), p. 345

[9] O. HERRE, W. WESCH, E. WENDLER, P.I. GAIDUK, F.F. KOMAROV, S. KLAUMÜNZER, AND P. MEIER: In: *Phys. Rev. B* 58 (1998), p. 4832

[10] W. WESCH, O. HERRE, P.I. GAIDUK, E. WENDLER, S. KLAUMÜNZER, AND P. MEIER: In: *Nucl. Instrum. Methods B* 146 (1998), p. 341

[11] P.I. GAIDUK, F.F. KOMAROV, AND W. WESCH: In: *Nucl. Instrum. Methods B* 164 (2000), p. 377

[12] P.I. GAIDUK, F.F. KOMAROV, V.S. TISHKOV, W. WESCH, AND E. WENDLER: In: *Phys. Rev. B* 61 (2000), p. 15785

[13] G. SZENES, Z.E. HORVÁTH, B. PÉCZ, F. PÁSZTI, AND L. TÓTH: In: *Phys. Rev. B* 65 (2002), p. 045206

[14] F. KOMAROV, P. GAIDUK, AND A. KAMAROU: In: *Vacuum* 63 (2001), p. 657

[15] W. WESCH, A. KAMAROU, E. WENDLER, K. GÄRTNER, P.I. GAIDUK, AND S. KLAUMÜNZER: In: *Nucl. Instrum. Methods B* 206 (2003), p. 1018

[16] W. WESCH, A. KAMAROU, AND E. WENDLER: In: *Nucl. Instrum. Methods B* 225 (2004), p. 111

[17] W. WESCH, A. KAMAROU, E. WENDLER, AND S. KLAUMÜNZER: In: *Nucl. Instrum. Methods B* 242 (2006), p. 363

[18] A. KAMAROU, W. WESCH, E. WENDLER, AND S. KLAUMÜNZER: In: *Nucl. Instrum. Methods B* 225 (2004), p. 129

[19] A. KAMAROU, E. WENDLER, AND W. WESCH: In: *J. Appl. Phys.* 97 (2005), p. 123532

[20] A. KAMAROU, W. WESCH, E. WENDLER, A. UNDISZ, AND M. RETTENMAYR: In: *Phys. Rev. B* 73 (2006), p. 184107

[21] R.L. FLEISCHER, P.B. PRICE, AND R.M. WALKER: *Nuclear Tracks in Solids*. University of California Press, 1975

[22] R.E. JOHNSON AND W.L. BROWN: In: *Nucl. Instrum. Methods* 198 (1982), p. 103

[23] D. LESUEUR AND A. DUNLOP: In: *Radiat. Eff.* 126 (1993), p. 163

[24] D.A. YOUNG: In: *Radiat. Meas.* 27 (1997), p. 575

[25] Y. KITAZOE, N. HIRAOKA, AND Y. YAMAMURA: In: *Surf. Sci.* 111 (1981), p. 381

[26] Y. YAMAMURA: In: *Nucl. Instrum. Methods* 194 (1982), p. 515

[27] I.S. BITENSKY AND E.S. PARILIS: In: *Nucl. Instrum. Methods B* 21 (1987), p. 26

[28] C.C. WATSON AND T.A. TOMBRELLO: In: *Radiat. Eff.* 89 (1985), p. 263

[29] P. STAMPFLI AND K.H. BENNEMANN: In: *Phys. Rev. B* 49 (1994), p. 7299

[30] P. STAMPFLI: In: *Nucl. Instrum. Methods B* 107 (1996), p. 138

[31] M. Toulemonde, C. Dufour, and E. Paumier: In: *Phys. Rev. B* 46 (1992), p. 14362

[32] S. Furuno, H. Otsu, K. Hojou, and K Izui: In: *Nucl. Instrum. Methods B* 107 (1996), p. 223

[33] C. Dufour, E. Paumier, and M. Toulemonde: In: *Nucl. Instrum. Methods B* 122 (1997), p. 445

[34] F. Agulló-López, G. García, and J. Olivares: In: *J. Appl. Phys.* 97 (2005), p. 093514

[35] F. Desauer: In: *Z. Phys.* 12 (1923), p. 38

[36] F. Seitz and J.F. Koehler: In: *Solid State Phys.* 2 (1956), p. 305

[37] C. Dufour, A. Audouard, F. Beuneu, J. Dural, J.P. Girard, A. Hairie, M. Levalois, E. Paumier, and M. Toulemonde: In: *J. Phys.: Cond. Matter* 5 (1993), p. 4573

[38] A. Meftah, F. Brisard, J.M. Costantini, E. Dooryhee, M. Hage-Ali, M. Hervieu, J.P. Stoquert, F. Studer, and M. Toulemoude: In: *Phys. Rev. B* 49 (1994), p. 12457

[39] Z.G. Wang, Ch. Dufour, E. Paumier, and M. Toulemonde: In: *J. Phys.: Cond. Matter* 6 (1994), p. 6733

[40] M. Toulemonde, Ch. Dufour, Z. Wang, and E. Paumier: In: *Nucl. Instrum. Methods B* 112 (1996), p. 26

[41] A. Meftah, J.M. Costantini, M. Djebara, N. Khalfaoui, J.P. Stoquert, F. Studer, and M. Toulemonde: In: *Nucl. Instrum. Methods B* 122 (1997), p. 470

[42] E.M. Johnson, R.E. Johnson: In: *Nucl. Instrum. Methods B* 143 (1998), p. 513

[43] E.M. Bringa and R.E. Johnson: In: *Phys. Rev. Lett.* 88 (2002), p. 165501

[44] A. Miotello, R. Kelly, and M. Dapor: In: *Nucl. Instrum. Methods B* 141 (1998), p. 16

[45] W. Bolse and B. Schattat: In: *Nucl. Instrum. Methods B* 190 (2002), p. 173

[46] W. Bolse: In: *Surf. Coatings Technol.* 158-159 (2002), p. 1

[47] W. Bolse and B. Schattat: In: *Nucl. Instrum. Methods B* 209 (2003), p. 32

[48] Z.G. Wang, C. Dufour, S. Euphrasie, and M. Toulemonde: In: *Nucl. Instrum. Methods B* 209 (2003), p. 194

[49] W. Bolse, B. Schattat, A. Feyh, and T. Renz : In: *Nucl. Instrum. Methods B* 218 (2004), p. 80

[50] B. Schattat and W. Bolse: In: *Nucl. Instrum. Methods B* 225 (2004), p. 105

[51] T. Som, B. Satpati, P.V. Satyam, D. Kabiraj, Ajay Gupta, and N.C. Mishra: In: *J. Appl. Phys.* 96 (2004), p. 7141

[52] A.S. Khalil, D.J. Llewellyn, M.C. Ridgway, A.M. Stewart, A.P. Byrne, and L.T. Chadderton: In: *Microsc. and Microanal.* 10 (Suppl. S02) (2004), p. 580

[53] K. Gärtner: In: G. Götz and K. Gärtner (Eds.): *High Energy Ion Beam Analysis of Solids*, Akademie-Verlag Berlin, 1988, p. 13–30

[54] D.W. Palmer: *Properties of semiconductors http://www.semiconductors.co.uk 2003.04.*

[55] D. Bimberg, R. Blachnik, M. Cardona, P.J. Dean, Th. Grave, G. Harbeke, K. Hübner, U. Kaufmann, W. Kress, O. Madelung, W. v. Münch, U. Rössler, J. Schneider, M. Schulz, and M.S. Skolnick: Physics of Group IV Elements and III-V Compounds. In: O. Madelung and M. Schulz (Eds.): *Landolt-Börnstein: Numerical Data and Functional Relationships in Science and Technology - New Series* Vol. 17a. Berlin : Springer-Verlag, 1982

[56] O. Pätzold, B. Fischer, and A. Cröll: In: *Cryst. Res. Technol.* 37 (2002), p. 1058

[57] O. Pätzold, I. Grants, U. Wunderwald, K. Jenkner, A. Cröll, and G. Gerbeth: In: *J. Cryst. Growth* 245 (2002), p. 237

[58] J.P. Biersack and J.F. Ziegler: *The Stopping and Ranges of Ions in Matter*. Vol. 1. Oxford : Pergamon Press, 1985

[59] P.M. Mooney and J.C. Bourgoin: In: *Phys. Rev. B* 29 (1984), p. 1962

[60] R. Bäuerlein: In: *Z. Phys.* 176 (1963), p. 198

[61] B. Massarani and J.C. Bourgoin: In: *Phys. Rev. B* 34 (1986), p. 2470

[62] K. Gärtner: In: *Nucl. Instrum. Methods B* 132 (1997), p. 147

[63] Z.G. Wang, C. Dufour, M.D. Hou, G.M. Jin, Y.F. Jin, E. Paumier, and M. Toulemonde: In: *Nucl. Instrum. Methods B* 135 (1998), p. 265

[64] H. Huber, W. Assmann, S.A. Karamian, H.D. Mieskes, H. Nolte, E. Gazis, M. Kokkoris, S. Kossionides, R. Vlastou, R. Grötzschel, A. Mücklich, W. Prusseit: In: *Nucl. Instrum. Methods B* 146 (1998), p. 309

[65] K. Nordlund and R.S. Averback: In: *Phys. Rev. B* 56 (1997), p. 2421

[66] N. Darowski, I. Zizak, G. Schumacher, S. Klaumünzer, and E. Wendler: In: *Nucl. Instrum. Methods B* 209 (2003), p. 131

[67] N. Darowski, I. Zizak, and G. Schumacher: In: *Phys. B* 357 (2005), p. 118

[68] H.-D. Betz: In: *Rev. Mod. Phys.* 44 (1972), p. 465

[69] G. Schiwietz, K. Czerski, M. Roth, F. Staufenbiel, and P.L. Grande: In: *Nucl. Instrum. Methods B* 226 (2004), p. 683

[70] I.S. Dmitriev, V.P. Zaikov, E.A. Kral'kina, V.S. Nikolaev, and Ya.A. Teplova: In: *Nucl. Instrum. Methods B* 14 (1986), p. 515

[71] Y. Sato, T. Miyoshi, T. Murakami, K. Noda, V.P. Shevelko, and H. Tawara: In: *Nucl. Instrum. Methods B* 225 (2004), p. 439

[72] E. Wendler, T. Opfermann, and P.I. Gaiduk: In: *J. Appl. Phys.* 82 (1997), p. 5965

[73] J.F. Gibbons: In: *Proc. IEEE* 60 (1972), p. 1062

[74] I. Jenčič, E.P. Hollar, and I.M. Robertson: In: *Philos. Mag.* 83 (2003), p. 2557

[75] R.S. Averback: In: *Nucl. Instrum. Methods B* 15 (1986), p. 675

[76] W. Bolse: In: *Mat. Sci. Eng. A* 253 (1998), p. 194

[77] J. Tarus, K. Nordlund, J. Sillanpää, and J. Keinonen: In: *Nucl. Instrum. Methods B* 153 (1999), p. 378

[78] S. Kumar, P.K. Sahoo, R.S. Chauhan, D. Kabiraj, Umesh Tiwari, D. Varma, and D.K. Avasthi: In: *Nucl. Instrum. Methods B* 212 (2003), p. 238

[79] G. Schiwietz, E. Luderer, G. Xiao, and P.L. Grande: In: *Nucl. Instrum. Methods B* 175 (2001), p. 1

[80] M. Raff, M. Schütze, C. Trappe, R. Hannot, and H. Kurz: In: *Phys. Rev. B* 50 (1994), p. 11031

[81] K. Sokolowski-Tinten, J. Bialkowski, and D. von der Linde: In: *Phys. Rev. B* 51 (1995), p. 14186

[82] L. Huang, J.P. Callan, E.N. Glezer, and E. Mazur: In: *Phys. Rev. Lett.* 80 (1998), p. 185

[83] B.T. Price: In: *Rep. Progr. Phys.* 18 (1955), p. 52

[84] S.P. Ahlen: In: *Rev. Mod. Phys.* 52 (1980), p. 121

[85] M.P.R. Waligórski, R.N. Hamm, and R. Katz: In: *Int. J. Radiat. Appl. Instrum., Part D: Nucl. Tracks Radiat. Meas.* 11 (1986), p. 309

[86] D. Drouin, A.R. Couture, R. Gauvin, P. Hovington, P. Horny, and H. Demers: *Computer code* CASINO, *version 2.42 (2002)* (see http://www.gel.usherbrooke.ca/casino/index.html)

[87] P.L. Grande and G. Schiwietz: In: *Nucl. Instrum. Methods B* 195 (2002), p. 55

[88] J.A. Bearden and A.F. Burr: In: *Rev. Mod. Phys.* 39 (1967), p. 125

[89] M. Cardona and L. Ley (Eds.): *Photoemission in Solids I: General Principles (with additional corrections)*. Berlin : Springer-Verlag, 1978

[90] J.C. Fuggle and N. Martensson: In: *J. Electron Spectrosc. Relat. Phenom.* 21 (1980), p. 275

[91] M.G. Holland: In: *Phys. Rev.* 134 (1964), p. A471

[92] A. Amith, I. Kudman, and E.F. Steigmeier: In: *Phys. Rev.* 138 (1965), p. A1270

[93] T. Elsaesser, M. Woerner: In: *Phys. Rep.* 321 (1999), p. 253

[94] A. Chatterjee and H.J. Schaefer: In: *Radiat. Environ. Biophys.* 13 (1976), p. 215

[95] A. Chatterjee and J.L. Magee: Track Models and Radiation Chemical Yields. In: *Radiation Chemistry: Principles and Applications*, VCH Publishers, Inc., 1987, p. 173

[96] F. Studer, M. Hervieu, J.-M. Costantini, and M. Toulemonde: In: *Nucl. Instrum. Methods B* 122 (1997), p. 449

[97] C. Trautmann, M. Toulemonde, K. Schwartz, J.M. Costantini, and A. Müller: In: *Nucl. Instrum. Methods B* 164 (2000), p. 365

[98] M.I. Kaganov, I.M. Lifshitz, and L.V. Tanatarov: In: *Sov. Phys. JETP* 4 (1957), p. 173

[99] I.A. Baranov, Yu.V. Martinenko, S.O. Tsepelevitch, and Yu.N. Yavlinskii: In: *Sov. Phys. Usp.* 31 (1988), p. 1015

[100] S. Adao: *Physical properties of III-V semiconductor compounds: InP, InAs, GaAs, GaP, InGaAs, and InGaAsP*. New York, U.S.A. : John Wiley & Sons, 1992

[101] S.E. Laux and M.V. Fischetti: *Computer code* DAMOCLES *(see ”Material parameters” section (Table 7) in ”Numerics” part at http://www.research.ibm.com/DAMOCLES/html_files/numerics.html#table7)*

[102] K. Izui: In: *J. Phys. Soc. Jpn.* 20 (1965), p. 915

[103] F.F. Komarov and A.F. Komarov: In: *Sov. Phys. JETP* 86 (1998), p. 270

[104] F.F. Komarov, A.F. Komarov, and A.M. Mironov: In: *Nucl. Instrum. Methods B* 148 (1999), p. 159

[105] D. Arnold and E. Cartier: In: *Phys. Rev. B* 46 (1992), p. 15102

[106] A.A. Kamarou, D.A. Malafei, and V.S. Shchehlik: In: *Proc. 2nd Int. Conf. CFDM-98 (Finite-difference methods: theory and applications)* Vol. 2. Minsk, Belarus, 1998, p. 56

[107] J. Bonse, S.M. Wiggins, and J. Solis: In: *J. Appl. Phys.* 96 (2004), p. 2628

[108] C.M. Bhandari and D.M. Rowe: In: *J. Phys. D: Appl. Phys.* 10 (1977), p. L59

[109] M. Mikou, R. Carin, P. Bogdanski, and R. Madelon: In: *Nucl. Instrum. Methods B* 107 (1996), p. 246

[110] M. Levalois and P. Marie: In: *Nucl. Instrum. Methods B* 156 (1999), p. 64

[111] A. Colder, O. Marty, B. Canut, M. Levalois, P. Marie, X. Portier, S.M.M. Ramos, and M. Toulemonde: In: *Nucl. Instrum. Methods B* 174 (2001), p. 491

[112] B. Canut, N. Bonardi, S.M.M. Ramos, S. Della-Negra: In: *Nucl. Instrum. Methods B* 146 (1998), p. 296

[113] A. Dunlop, G. Jaskierowicz, and S. Della-Negra: In: *Nucl. Instrum. Methods B* 146 (1998), p. 302

[114] A. COLDER, B. CANUT, M. LEVALOIS, P. MARIE, X. PORTIER, AND S.M.M. RAMOS: In: *J. Appl. Phys.* 91 (2002), p. 5853

[115] F.F. KOMAROV, P.I. GAIDUK, L.A. VLASUKOVA, A.J. DIDYK, AND V.N. YUVCHENKO: In: *Vacuum* 70 (2003), p. 75

[116] E. WENDLER, W. WESCH, AND G. GÖTZ: In: *Nucl. Instrum. Methods B* 63 (1992), p. 47

[117] W. WESCH: In: *Nucl. Instrum. Methods B* 68 (1992), p. 342

[118] K.E. SICKAFUS, L. MINERVINI, R. W. GRIMES, J. A. VALDEZ, M. ISHIMARU, F. LI, K.J. MCCLELLAN, AND T. HARTMANN: In: *Science* 289 (2000), p. 748

[119] K. TRACHENKO: In: *J. Phys.: Cond. Matter* 16 (2004), p. R1491

Acknowledgements

Now I want to express my hearty thanks to all people that have directly or indirectly contributed to the present work.

First, I am greatly indebted to Prof. Dr. Werner Wesch (IFK, FSU Jena) for the excellent supervision and all-round support of my thesis. His numerous invaluable advices and suggestions as well as many helpful discussions have noticeably improved this work.

Many thanks to Prof. Dr. Wolfgang Witthuhn, Dr. Konrad Gärtner, Dr. Elke Wendler, Dr. Frank Schrempel, Mrs. Carmen Voigt, Mr. Gerald Lenk, Mr. Ullrich Barth (all IFK, FSU Jena), and Dr. Christian Schubert (previously IFK, FSU Jena; now HMI Berlin) for their help, support, and advices over the past several years.

My special thanks to Dr. André Hedler (IFK, FSU Jena) and Dr. Siegfried Klaumünzer (ISL, HMI Berlin) for the experimental support during ion irradiations at the ISL laboratory of the HMI and for many fruitful discussions.

Besides, my sincere gratitude goes to Prof. Dr. Peter Gaiduk and Mr. Oleg Milchanin (both from BSU Minsk), and Prof. Dr. Markus Rettenmayr and Mr. Andreas Undisz (both from the Institut für Materialwissenschaft und Werkstofftechnologie, FSU Jena) for TEM analysis of many GaAs and InP samples.

And, last but not least, many hearty thanks to my wife Maryia Kamarova, my daughter Alesja Kamarova, my father Aliaksandr Kamarou, my mother Ludmila Kamarova and my brother Aliaksandr Kamarou for the permanent confidence, countenance and love in the private life.

Ich danke dem Bundesministerium fur Bildung und Forschung und der Deutschen Forschungsgemeinschaft für die Finanzielle Unterstützung dieser Arbeit.

Ehrenwörtliche Erklärung

Ich erkläre hiermit ehrenwörtlich, dass ich die vorliegende Arbeit selbstständig und ohne Hilfe Dritter und ohne Benutzung anderer als der angegebenen Hilfsmittel und Literatur angefertigt habe. Die aus anderen Quellen direkt oder indirekt übernommenen Daten und Konzepte sind unter Angabe der Quelle gekennzeichnet.

Weitere Personen waren nicht an der inhaltlich-materiellen Erstellung der vorliegenden Arbeit beteiligt. Insbesondere habe ich hierfür nicht die entgeltliche Hilfe von Vermittlungs- bzw. Beratungsdiensten (Promotionsberater oder andere Personen) in Anspruch genommen. Niemand hat von mir unmittelbar oder mittelbar geldwerte Leistungen für die Arbeiten erhalten, die im Zusammenhang mit dem Inhalt der vorgelegten Dissertation stehen.

Die Arbeit wurde bisher weder im In- noch im Ausland in gleicher oder ähnlicher Form einer anderen Prüfungsbehörde vorgelegt.

Die geltende Prüfungsordnung der Physikalisch-Astronomischen Fakultät ist mir bekannt.

Ich versichere ehrenwörtlich, dass ich nach bestem Wissen die reine Wahrheit gesagt und nichts verschwiegen habe.

Jena, den 30. November 2006

……………………………

Andrey Kamarou

Lebenslauf

Persönliche Daten

Name	Kamarou
Vorname	Andrey
Geburtsdatum	1. März 1975
Geburtsort	Minsk (Belarus)

Schulausbildung

1982–1992	Mittelschulen Nr. 36, 118, und 50 in Minsk
25.06.1992	Abitur, Prädikat “Auszeichnung”

Studium

09/1992–12/1996	Studium der Physik an der Belarussischen Staatlichen Universität Minsk
01/1997–06/1997	Diplomarbeit mit dem Thema “Defekt- und Spurbildung in einkristallinen Halbleitern hervorgerufen durch Hochenergie-Schwerionenbestrahlung”
27.06.1997	Diplom in Physik, Prädikat “Auszeichnung”
11/1997–11/2000	Promotionsarbeit an der Belarussischen Staatlichen Universität Minsk
seit 07/2001	Promotionsarbeit am Institut für Festkörperphysik der Friedrich-Schiller-Universität Jena

Berufliche Tätigkeit

08/1997–11/1997 11/2000–07/2001	wissenschaftlicher Mitarbeiter am Institut für Angewandte Physik der Belarussischen Staatlichen Universität Minsk
seit 07/2001	wissenschaftlicher Mitarbeiter am Institut für Festkörperphysik der Friedrich-Schiller-Universität Jena

Jena, den 30. November 2006

………………………………

Andrey Kamarou